Design of a High Resolution Time-of-Flight Crystal Analyser Spectrometer and Hydrogen Diffusion in Intermetallic Compounds.

by

Stuart Ian Campbell

A thesis submitted in partial fulfilment of
the requirements of the Degree of
Doctor of Philosophy

Department of Physics
Joule Laboratory
Science Research Institute
University of Salford
Salford M5 4WT
United Kingdom

September 1998

To Mum and Dad

Contents

List of Tables

List of Figures

Acknowledgements

Firstly, I would like to thank my supervisor, Keith Ross for all his supervision throughout the course of this project. Without his enthusiasm and particular insight it would have been more difficult to make the most of this project. I am also grateful to David Martín whose help and guidance was instrumental in the work carried out as part of the OSIRIS Project.

I would like to thank all the past and present members of the Neutron Scattering and Materials Physics Group at Salford University for their help during the course of my PhD, namely Philip Shepherd, Michelle Mercer, Paul Cray, Martin Poyser, Mohamed Kemali, Paco Fernandez, Dan Bull and Darren Broom.

The experimental sections of this thesis would have not been possible without the help of a number of people. I would like to Mark Johnson from the ILL for his help with the quasi-elastic experiments. The multireflectivity measurements would not have been possible without the co-operation of the IRIS instrument scientists, Mark Adams and Winnie Kagunya. Thanks must also go to a number of staff at Rutherford Appleton Laboratory that have helped with my general scientific understanding, in particular Steve Bennington, Wolfgang Hahn and Chris Frost.

In particular I would like to thank Steve & Kate Bennington for all their generous hospitality. I am also grateful to Chris Frost for sharing his particular insight into life with anyone that would listen.

I would also like to thank the members of the Crystal Analyser Group who made me feel welcome during the year I spent at ISIS, namely, John Tomkinson, Andrew Fielding, David Martín, Mark Adams, Winnie Kagunya and Stewart Parker. I would also like to thank Colin Carlile for agreeing to help with the financial cost of my accommodation during that year.

My special thanks also go to Mike Johnson, firstly for giving me a job, but also for allowing me the time to complete this thesis.

I would like to thank David Joyce, not only for helping me carry out the AFM measurements presented, but also for having the patience to share a house with me for what must have seemed like an eternity.

Finally, and most importantly, I would like to thank my Mum and Dad for all their support (both financial and otherwise), encouragement and patience throughout my PhD.

Abstract

The main part of this thesis concerns the design and simulation of a polarization analysis backscattering cold neutron spectrometer, OSIRIS, at the ISIS pulsed neutron source. The OSIRIS instrument consists of two parts, a high-resolution powder diffractometer and a micro-eV resolution inelastic spectrometer. The incident cold neutron beam has the option of being polarised by means of a series of interchangeable polarising benders. The inelastic spectrometer consists of an analyser array constructed from pyrolytic graphite crystals situated in near-backscattering geometry. Monte Carlo simulations have been performed in order to optimise and investigate various components of the spectrometer, including the guide, polarisers and analyser.

A microguide testing device, MITED, has been constructed, commissioned and, using it, measurements have been made on neutron guide sections. This instrument has also been used to test the reflectivity of supermirror coated guide sections.

Originally, it was the aim of this thesis to carry out all the scientific commissioning experiments required for OSIRIS. This has become unfeasible due to manpower problems within the ISIS facility, which have delayed the construction of the OSIRIS spectrometer and have moved it out of the time range of this thesis.

Therefore an extra section of work has been included, on a family of intermetallic metal hydride systems that it will be of interest to investigate using the OSIRIS instrument.

A general study of the diffusion of hydrogen in C15 Laves phase intermetallic compounds has been performed. This has employed the techniques of quasi-elastic neutron scattering, inelastic vibrational spectroscopy, diffraction and muon spectroscopy.

Chapter 1

Introduction

1.1 Neutron properties and Condensed Matter Research

James Chadwick first discovered the neutron in the 1930's, but it was not until the proliferation of research reactors with sufficiently high thermal neutron fluxes in the late 1950's that the neutron becomes more widely used as a probe in condensed matter research. The neutron consists of two down quarks (each of which has a charge of - 1/3 e, where e is the charge of an electron) and one up quark (charge +2/3 e). Thus we have a particle that has a net electric charge of zero. It has an electric dipole moment that is either zero or too small to be measured by the most sensitive of modern techniques (Ramsey 1989). The neutrons value to condensed matter research is due to the fact that it has a de Broglie wavelength $\left(\lambda = h/mv\right)$, comparable to that of the interatomic spacing in many physical systems and also that its energy is comparable to many atomic and electronic processes, (i.e. in the meV to eV range). As the neutron has a net charge of zero, and therefore has the ability to penetrate far into matter, it is possible for experiments to be performed on samples 'in-situ', i.e. whilst inside specialist sample environment equipment, such as furnaces, cryostats or pressure cells. It's intrinsic spin angular momentum is 1/2 in nuclear units. The neutron has a magnetic moment, μ_n of -1.913 Bohr magnetons, which means that it can interact with other particles, either through a magnetic or the strong nuclear interaction.

1.2 Production of Neutrons

There are two different types of neutron source, those that provide a pulsed neutron beam and those that supply a continuous source of neutrons. Generally continuous sources are in the form of nuclear reactors, but it is also possible to generate a steady

accelerator-based source of neutrons using the spallation reaction, such as SINQ at the Paul Scherrer Institute, but this type of source will not be discussed here. What follows is a brief description of both a reactor (ILL) and a pulsed spallation source (ISIS).

1.2.1 High Flux Reactor (HFR) at the ILL

The traditional method of producing neutrons is by means of fission (Figure 1.1) in a nuclear reactor. The High-Flux Reactor at the Institut Max von Laue-Paul Langevin, Grenoble (Figure 1.2) is the most intense source of thermal neutrons for condensed matter research in the world. It operates at a thermal power of 58 MW using a single U^{235} fuel-element (9 kg) with an operating cycle of 50 days. This single fuel-element sits in the centre of a 2.5 metre diameter tank, containing the heavy water moderator. Cooling and moderation is by deuterated water circulation passing through heat exchangers. In addition the moderator also helps by reflecting the thermalized neutrons towards the fuel element.

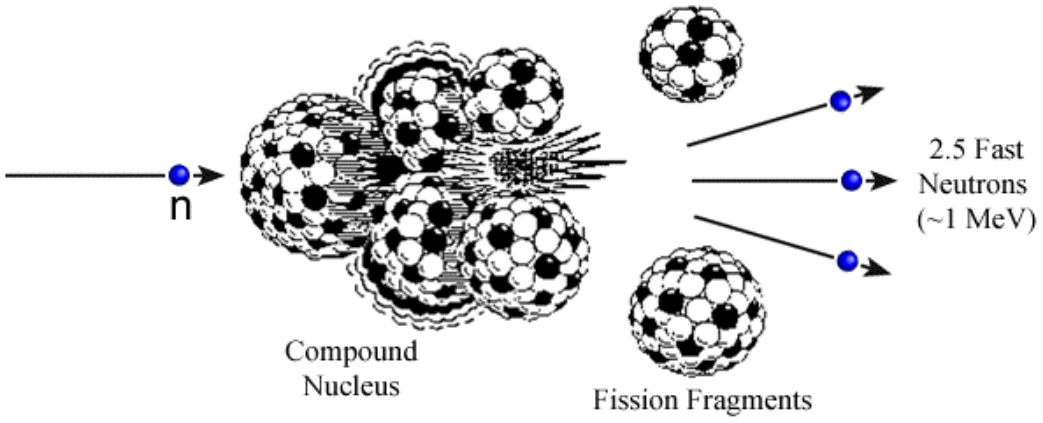

Figure 1.1: Production of neutrons by nuclear fission.

Biological shielding is provided by a light water swimming pool type assembly surrounding the reflector tank and encased in dense concrete. Neutron beams produced from reactors are very intense and give a continuous source of neutrons, which then thermalise in the moderator that surrounds the core, before being emitted

with a broad band of wavelengths. In addition to the thermal moderator there are an additional two different types of moderator that sit inside the reactor vessel, a graphite block which is heated to 2400K providing hot neutrons, while boiling deuterium at 25K produces cold neutrons. Wavelength selection is generally achieved by Bragg scattering from a crystal monochromator or by velocity selection through a mechanical chopper.

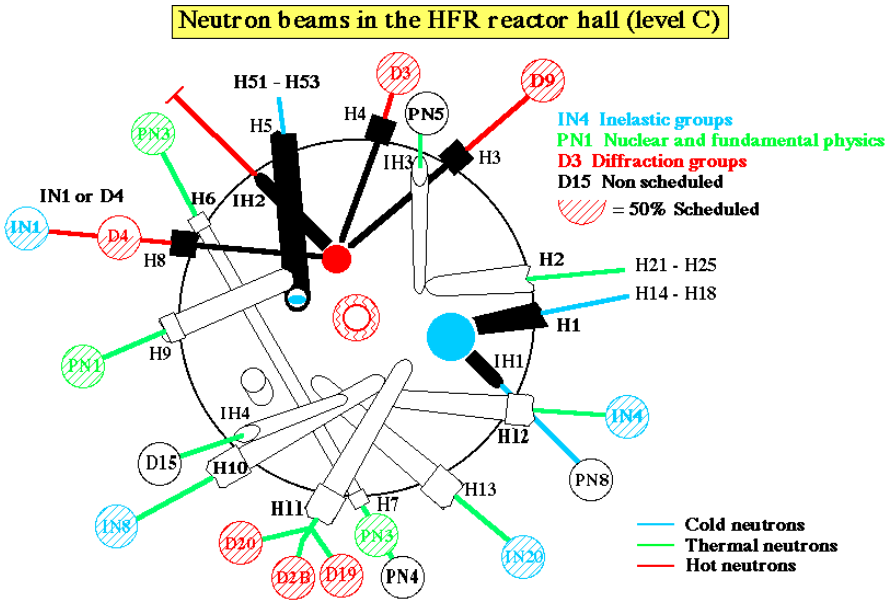

Figure 1.2: A vertical view of the ILL High Flux Reactor

1.2.2 Pulsed Spallation Source, ISIS

The ISIS Facility at the Rutherford Appleton Laboratory is the most intense pulsed spallation[1] source in the world. Steady state fission reactors dedicated to the production of neutrons for condensed matter research produce many tens of MW of heat within the reactor core. In the most advanced, heat dissipation in the core approaches the limits set by current materials technology. ISIS, on the other hand, produces neutrons in a different manner. The spallation process (Figure 1.3), in which neutrons are produced by bombarding a heavy metal target with highly energetic particles from a powerful accelerator, produces less heat per neutron and

can be pulsed at will. As a result of the low duty cycle of the ISIS accelerator, the time averaged heat production in the ISIS target is a modest 160 kW, but in the pulse, the neutron brightness exceeds that of the most advanced steady state sources.

The production of particles energetic enough to produce efficient spallation involves three stages. First, an ion source produces H^- ions, which are accelerated in a pre-injector column to 665 keV. In the second stage, a linear accelerator, the H^- ions pass through four accelerating r.f. cavities to reach an energy of 70 MeV. At injection into the third stage, which is the synchrotron itself, the electrons are stripped from the H^- ions by a very thin (0.25 mm) alumina foil, producing a beam of protons. The proton synchrotron has a diameter of 52 metres and accelerates 2.5×10^{13} protons per pulse to 800 MeV, when they are extracted and sent to the target station. This process is repeated 50 times a second. The spallation target is made from a heavy metal such as depleted uranium or tantalum. Each high energy proton produces ~10 neutrons by chipping nuclear fragments from the heavy metal nucleus.

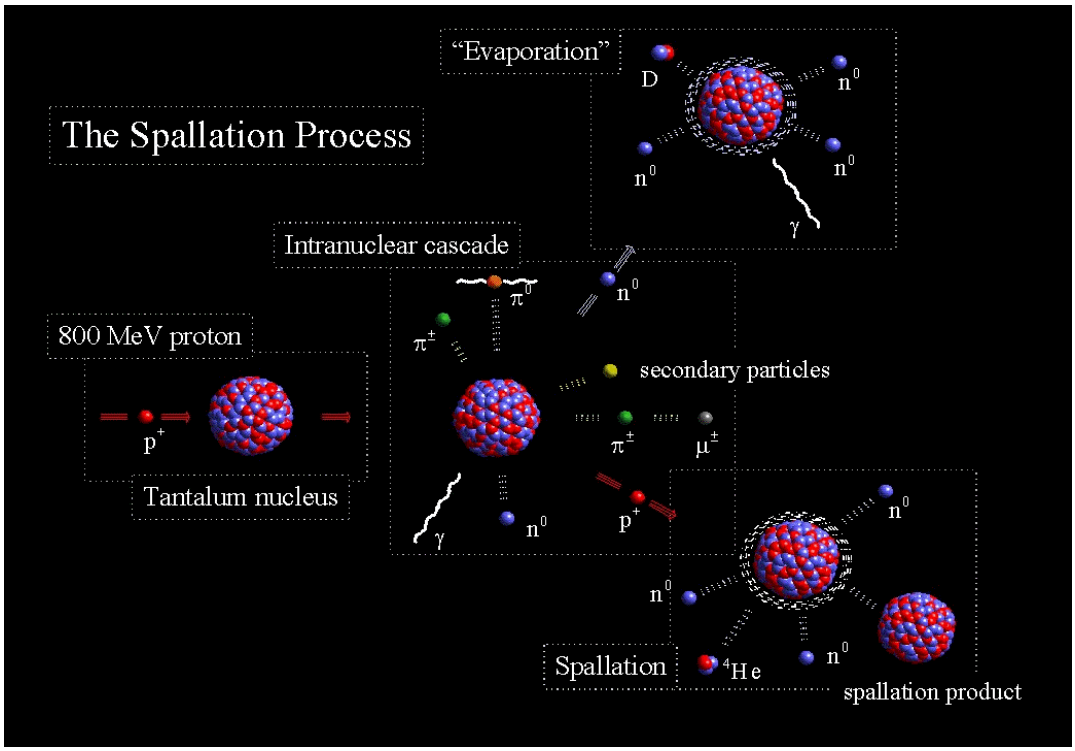

Figure 1.3: Neutron production process at a pulsed spallation source.

[1] From a mining term, the verb to spall, meaning to chip off.

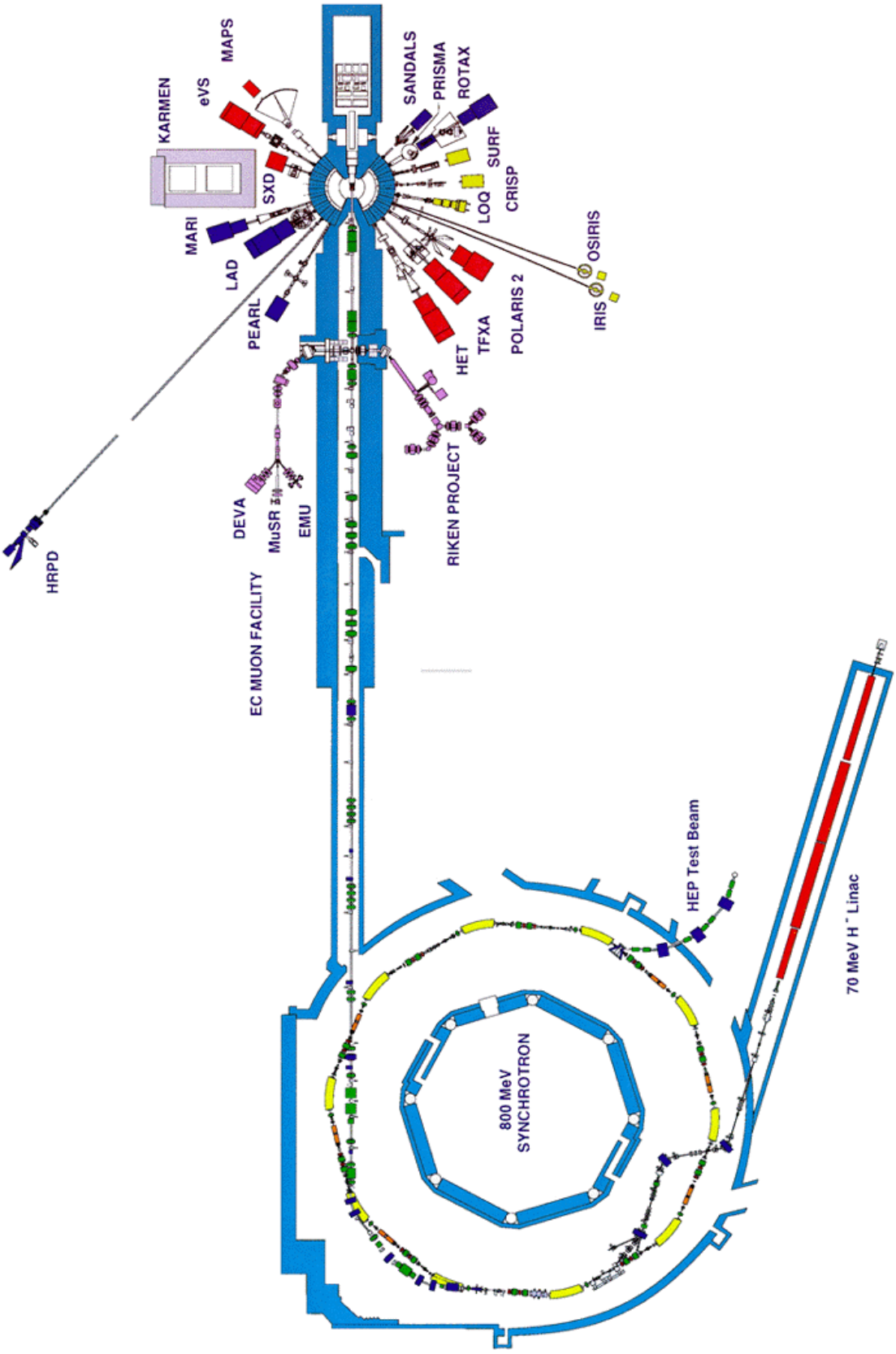

Figure 1.4: A Plan view of the ISIS Pulsed Neutron Source, showing its main components, the linear accelerator, synchrotron, target station and suite of instruments.

The neutrons produced in this process generally have very high energies and need to be slowed down before they can be of any use in condensed matter studies. We can achieve this by arranging a number of small hydrogenous moderators around the target. These exploit the large scattering cross-section of hydrogen to slow down the neutrons passing through, by repeated collisions with the hydrogen nuclei. The moderator temperature determines the final energy distribution of the neutrons produced, and this can be altered in order to perform different types of experiment. The moderators at ISIS consist of two ambient temperature water (315K, H_2O), a liquid methane (100K, CH_4) and a liquid hydrogen (20K, H_2). The design for a moderator on a pulsed source involves the trade off between maximising the flux whilst maintaining the pulsed width to a value that is consistent with the resolution requirements of the instruments. A plan view of the ISIS source and instrument suite can be seen in Figure 1.4. The 4π-equivalent fluxes for three of the ISIS moderators as calculated by Taylor (1984) are shown Figure 1.5, the equivalent curves for the moderators at the ILL have also been included for comparison.

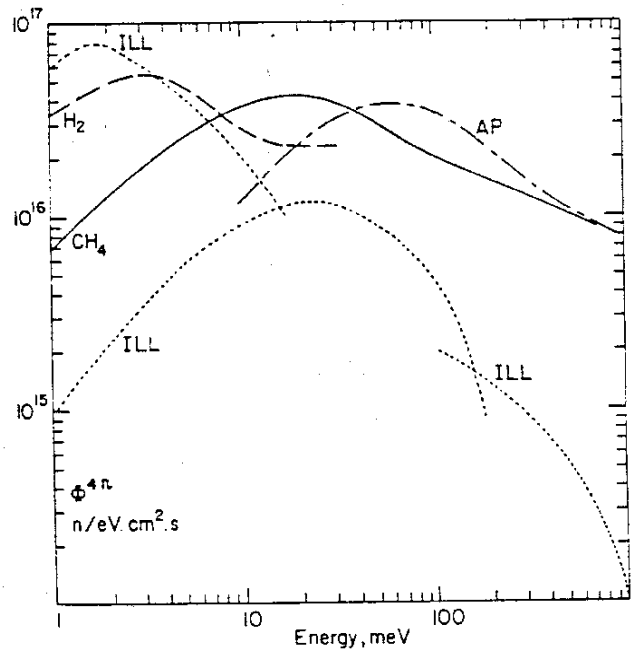

Figure 1.5: The predicted 4π equivalent fluxes for three ISIS moderators compared with the fluxes of the three moderators at the ILL (Taylor 1984). The designation AP refers to the asymmetric poisoned ambient water moderator.

The neutron spectrum that emerges from the small moderators is under-moderated, as the neutrons do not spend enough time in the moderators in order to achieve thermal equilibrium. Extending out from the target station there are a number of beamlines, at the end of which are situated the neutron instruments. Due to the nature of the source, time of flight techniques have to be employed, thereby imposing a constraint on the type of instrumentation that can be used. The consequences of this will be discussed in a later section.

It is also worth noting that in addition to a neutron source, the ISIS Facility is also an intense source of muons. Muons are produced by placing a graphite target in the initial proton beam. A small fraction of the protons collide with a proton or neutron of a carbon atom to produce pions. The pions are have a short half-life (~26 ns) and decay to produce muons which are then transported down beamlines with the aid of magnetic fields.

1.3 Laves Phase Intermetallic Compounds

In Chapter 5, a study of the hydrogen diffusion in a number of members of the C-15 Laves phase family of compounds is presented. C-15 Laves phase compounds, generally have the characteristic formula of AB_2 (where A can be a rare-earth and B is a transition metal). Examples of this type of compound are $TiCr_2$, HfV_2, TaV_2, $ZrCr_2$, and $ZrTi_2$, amongst others. These compounds have a space group of $Fd\bar{3}m$ ($N^{o.}$ 227). The hydrogen usually occupies one or more of three different types of tetrahedral interstitial site, one formed by four atoms of type B (b-site), another site formed by one atom of type A and three of type B (e-site) and a site formed by two A atoms and two B atoms (g-site). A list of atom and interstitial site positions are listed in Table 1.1. The structure is represented in Figure 1.6, the large blue spheres are A atoms and the smaller red spheres are the B atoms, the e, g and b tetrahedral interstitial sites are also shown.

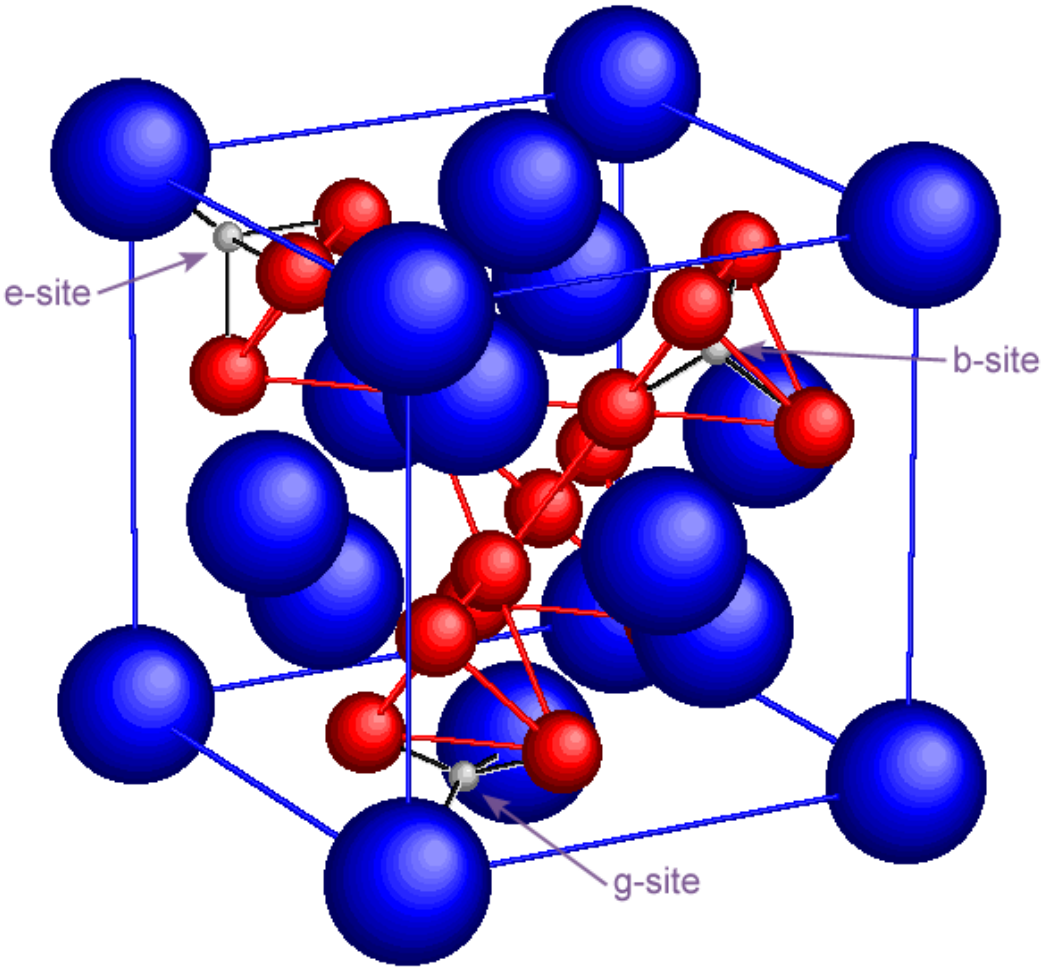

Figure 1.6: The C-15 Laves phase structure, illustrating the different types of interstitial site. The A atoms are the larger blue spheres, and the B are the smaller red spheres. Also shown are the b, e and g tetrahedral interstitial sites (grey spheres).

Table 1.1: Atoms and common interstitial sites for a AB_2 type C-15 compound.

Type of site	*Co-ordinates*	*$N^{o.}$ of sites*	*Wyckoff Notation*
A atom	(0.125, 0.125, 0.125)	8	a
B atom	(0.5 , 0.5, 0.5)	16	d
4B	(0.375, 0.375, 0.375)	8	b
1A-3B	(0.25, 0.25, 0.25)	32	e
2A-2B	(0.313, 0.125, 0.313)	96	g

If we assume a hard sphere model, where the metal atoms touch, then the hole size for each type of interstitial site can be calculated in terms of the lattice parameter. The hole sizes may be determined by the following expressions (Magee *et al.*, 1981);

$$R_{B_4} = \left(\sqrt{3} - \sqrt{2}\right)\frac{a_0}{8}$$

$$R_{AB_3} = \left(\frac{\sqrt{3}}{2+\sqrt{6}}\right)\frac{a_0}{8}$$

$$R_{A_2B_2} = \left[\frac{-\left(\sqrt{2}+\sqrt{3}\right) \pm \sqrt{2}\left(3+2\sqrt{6}\right)^{\frac{1}{2}}}{1+2\sqrt{6}}\right]\frac{3a_0}{8}$$

where a_0 is the lattice parameter of the given system. The radii of the metal atoms in order to obtain the hard sphere model are;

$$R_A = \sqrt{3}\,\frac{a_0}{8}$$

$$R_B = \sqrt{2}\,\frac{a_0}{8}$$

We can also, by using the above expressions, calculate the separation of nearest neighbour metal atoms, which turn out to be (Berry & Raynor, 1953);

$$d_{AA} = a_0\sqrt{3}/4,\ d_{BB} = a_0\sqrt{2}/4 \text{ and } d_{AB} = a_0\sqrt{11}/8.$$

Westlake (1983) has put forward two criteria that define whether a site can be occupied or not;

- That the hole diameter must exceed 0.4 Å.
- The distance between hydrogens must be greater than 2.1 Å.

These criteria have also proved successful in calculating the limiting hydrogen capacities. This “geometric model” has been used as a general guide throughout the analysis and discussion of the work presented in Chapter 5.

Chapter 2

Neutron Scattering Theory

In this chapter we will discuss the relevant basic concepts of neutron scattering. A number of comprehensive accounts have been made of the subject by a number of authors, (Squires, 1978; Turchin, 1965; Lovesey, 1984).

2.1 Neutron Scattering Length

The wavelength of a thermal neutron (~10^{-10} m) is much greater than the size of a nucleus (10^{-14} to 10^{-15}). Which means that the nucleus can be considered as a point scatterer. If a neutron is scattered by a nucleus the resulting scattered wave is therefore spherically symmetric.

Consider a neutron scattering experiment where the origin of the system is taken to be the nucleus, with the z-direction in the same direction as the wavevector, $\mathbf{k}_0$, of the incident neutrons, (as shown Figure 2.1).

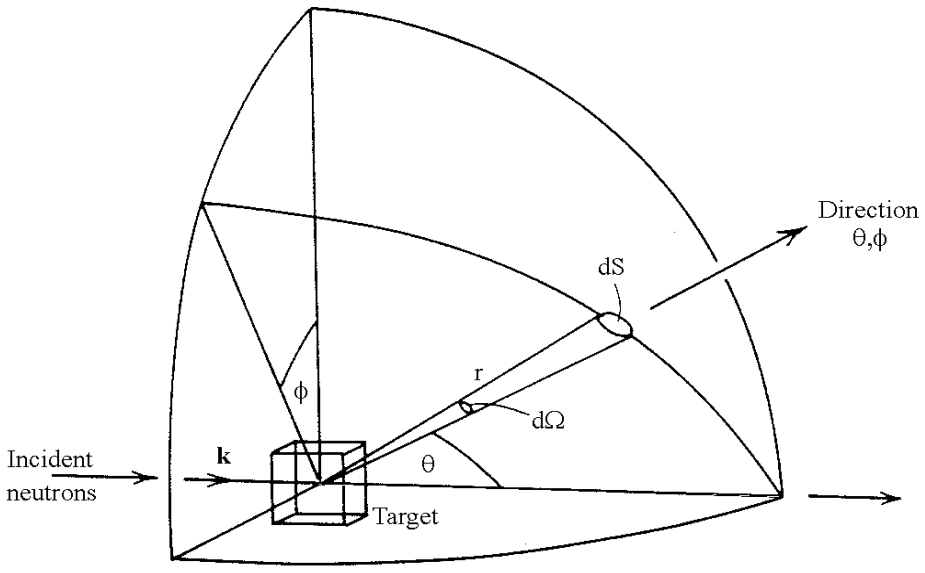

Figure 2.1: Geometry for a neutron scattering experiment.

The incident neutrons can be represented by the wave function

$$\psi_{inc} = e^{(i\mathbf{k}_0 z)} \tag{2.1}$$

As the scattered wave is spherically symmetric, then the wave function of the scattered neutrons can be written as

$$\psi_{sc} = -\frac{b}{r} e^{(i\mathbf{k}_1 r)} \tag{2.2}$$

where $\mathbf{k}_1$ is the wave vector of the scattered neutrons. The quantity b, which is constant and independent of the angles θ, ϕ, is known as the scattering length. The minus sign is conventionally inserted to make b positive for a repulsive potential. The scattering length is a complex quantity with the imaginary part corresponding to absorption of the neutron.

It is assumed that the interaction between the neutron and the nucleus is only a small perturbation in the potential field of the system, (the Born approximation[1]) and only weakly perturbs the wavefunction outside the nucleus. The implication of this is that for a nucleus at a position, r, then any neutron with a wavevector not at that position will not be scattered. We can describe the interaction potential as a delta function, the "Fermi pseudopotential" is conventionally used, as it gives the required isotropic scattering.

$$V(\mathbf{r}) = \left(\frac{2\pi\hbar^2}{m} \right) b\delta(\mathbf{r}) \tag{2.3}$$

[1] The Born approximation assumes that if a wavefunction is altered by an amount $\delta\psi$, then the second order terms, $\delta\psi^2$, can be ignored.

The scattering cross section is simply defined as the ratio of the number of neutrons scattered per unit time to the incident neutron flux,

$$\sigma = \frac{4\pi r^2 v \left| \frac{b}{r} e^{ikr} \right|^2}{v \left| e^{ik_0 z} \right|^2} = 4\pi b^2 \qquad (2.4)$$

where v is the velocity of the neutron. It is obvious that σ has the units of area and b the units of length. The scattering length is a quantity, which defines the amplitude of the scattering. Unlike x-rays, it does not follow a systematic variation with atomic number. The scattering length for elements that are next to each other in the periodic table (and even isotopes of the same element) can be very different and have to be defined empirically. This fact provides a means of distinguishing between individual species within a scattering sample, especially for studying light elements in the presence of much heavier ones, as in metal hydride systems or distinguishing between adjacent elements.

2.2 Coherent and Incoherent Scattering

A further random arrangement of isotopes within a sample of a single element type will result in a distribution in the scattering lengths throughout the sample, which will produce incoherent scattering. Even if the target isotope has non-zero spin, the state of the scattered wave, will depend upon the different possible configurations of the neutron and nuclear spins. Therefore the scattering length will have two possible values, b^+ and b^-. The total scattering cross section, σ, will therefore consist of two components; a coherent term σ_{coh}, which is given by

$$\sigma_{coh} = 4\pi \langle b \rangle^2 \qquad (2.5)$$

and an incoherent component, σ_{incoh}, given by :

$$\sigma_{incoh} = 4\pi \left\{ \langle b^2 \rangle - \langle b \rangle^2 \right\} \qquad (2.6)$$

A sample of relevant scattering lengths is given in Table 2.1.

Element	σ_{incoh} *(barns)*	σ_{coh} *(barns)*
H	80.27	1.7583
D	2.05	5.592
Hf	7.6	2.6
V	0.01838	5.08
Ti	1.485	2.87
Cr	1.66	1.83
Zr	6.44	0.02

Table 2.1 : The scattering cross sections for a number of nuclei that are commonly found in C-15 laves phase metal hydride systems.

2.3 Neutron Optics

Many components of the OSIRIS spectrometer make practical use of the theory presented below. In this section we will only briefly cover the theoretical aspects of neutron optics, fuller and more complete explanations can be found in numerous texts such as those by Sears (1989) and Squires (1978), along with the dynamical theory of neutron scattering.

Experiments have been performed to demonstrate the wave nature of the neutron. Phenomena more readily associated with optical processes such as refraction, total reflection, slit and grating diffraction have been observed using neutrons.

2.3.1 Refractive Index

Consider a thin slab of scattering material at a position z', with a small thickness $\Delta z'$, placed perpendicular to an incident neutron beam represented as $\exp(ikz)$, then each scattered wave is represented by $-(\bar{b}/r)\exp(ikr)$, where r is taken from the centre of the scattering nucleus to the observation point at z.

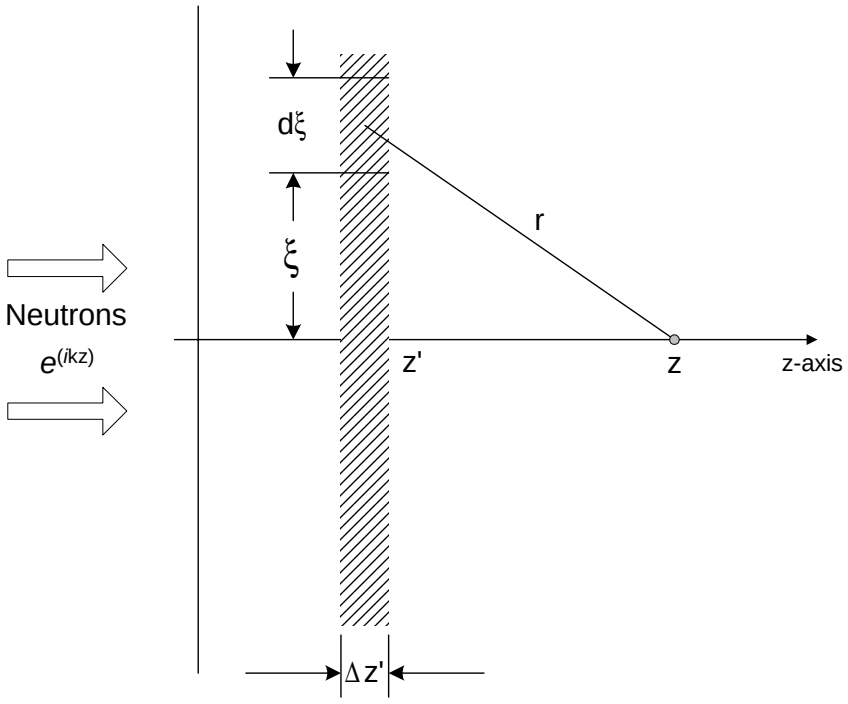

Figure 2.2: Geometrical convention used for neutron wave being scattered in a given direction.

The wave amplitude at the point z is just the sum of the amplitudes of the unscattered and scattered waves,

$$e^{ikz} - \int_0^{\infty} \sum b_i N_i \, 2\pi\xi d\xi \Delta z' e^{ikz'} \frac{e^{ikr}}{r} \tag{2.7}$$

where b_i is the coherent scattering length for an atom of the *i*'th type and N_i is the number of atoms of this type per unit volume. From Figure 2.2 we can see that

$$r = \sqrt{(z - z')^2 + \xi^2} \tag{2.8}$$

By integrating equation (2.7) with respect to *r*, we obtain

$$e^{ikz} - i\frac{2\pi}{k}\left(\sum_i b_i N_i\right) e^{ikz'} e^{ik|z-z'|} \Delta z' \tag{2.9}$$

For z'<z, the scattered wave is travelling in the same direction as the unscattered wave and if we add up the amplitudes at the point z we obtain

$$e^{ikz}\left[1-i\frac{2\pi}{k}\left(\sum_i b_i N_i\right)\Delta z'\right] \tag{2.10}$$

Therefore we can see that neutrons scattered from a layer of thickness Δz' and co-ordinate z', (0<z'<z), the wave amplitude at the point z is multiplied by a constant factor that is independent of z and z', which causes a phase shift. If we now place a number of layers of thickness Δz', so as to form a continuous medium in the range z'=0 to z'=z, we modify (2.10) to

$$e^{ikz}\left[1-i\frac{2\pi}{k}\left(\sum_i b_i N_i\right)\Delta z'\right]^{\frac{z}{\Delta z'}} \tag{2.11}$$

At the limit $\Delta z' \rightarrow 0$, equation (2.11) is transformed into the usual expression for a plane wave $\exp(ik'z)$, but with a wave vector k'.

$$k' = k - \frac{2\pi}{k}\sum_i b_i N_i \tag{2.12}$$

Hence the refractive index is

$$n = 1 - \frac{\lambda^2}{2\pi}\sum_i b_i N_i \tag{2.13}$$

2.3.2 The representation of scattering density by a virtual potential

It is possible to describe optical phenomena displayed by neutrons in terms of a coherent wave, $\psi(\mathbf{r})$, which obeys the one-body Schrödinger equation,

$$\left\{-\frac{\hbar^2}{2m}\Delta + V(\mathbf{r})\right\}\psi(\mathbf{r}) = E\psi(\mathbf{r}) \tag{2.14}$$

where $V(\mathbf{r})$ is the optical potential. Basically this is the effective interaction of the neutron with the material, and for a homogeneous medium this is

$$V(\mathbf{r}) = \begin{cases} v_0 & \text{inside medium} \\ 0 & \text{outside medium} \end{cases} \tag{2.15}$$

We can express the general solution of equation (2.14) by

$$\psi(\mathbf{r}) = \begin{cases} \sum A_1 \exp\left(i\mathbf{k}_1 \cdot \mathbf{r}\right) & \text{inside medium} \\ \sum A_2 \exp\left(i\mathbf{k}_2 \cdot \mathbf{r}\right) & \text{outside medium} \end{cases} \tag{2.16}$$

If we assume that the neutron has a kinetic energy of E_1 in medium (1) and E_2 in medium (2) then as we pass from one medium to another we experience a mean change of potential V_0 as we enter the medium.

$$E_1 = E_2 + V_0 \tag{2.17}$$

Expressed in terms of wave vectors, we have

$$E_1 = \frac{\hbar^2 k_2^2}{2m} + V_0 \tag{2.18}$$

As a neutron wave moves from one medium into another it will experience a change in its wave vector from $\mathbf{k}_1$ to $\mathbf{k}_2$. The index of reflection for the interface is generally defined as

$$n_{1,2} = \frac{k_1}{k_2} \tag{2.19}$$

therefore we can see from equation (2.18) that

$$n_{1,2} = \sqrt{\frac{E_1 - V_0}{E_1}}. \tag{2.20}$$

If we assume that $V_0 << E_1$ then we may write,

$$n_{1,2} \approx 1 - \frac{V_0}{2E_1} \tag{2.21}$$

We now consider the case of a neutron wave interacting with a magnetic material, as is the case for neutron polarisers. By assuming that medium (1) is a vacuum, we can present the energy E_1 as

$$E_1 = \frac{h^2}{2m\lambda^2} = \frac{2\pi^2\hbar^2}{m\lambda^2} \tag{2.22}$$

and that medium (2) is magnetic, and therefore has both a magnetic and a nuclear contribution to V_0. We can derive the nuclear part, V_N, from the Fermi pseudo potential (see section 2.1) to give,

$$V_N = \frac{2\pi\hbar^2}{m}\left(\overline{N}\,\overline{b}\right) \tag{2.23}$$

where $\overline{N}$ is the number density of scattering centres, and $\overline{b}$ is the mean bound coherent scattering length. The magnetic contribution, V_M, is expressed as

$$V_M = -\mu_n \cdot \mathbf{B} = \pm\mu_n B \tag{2.24}$$

where the ± refers to whether the neutron has a spin parallel or anti-parallel to the direction of the materials magnetic field, **B**. From equation (2.21) we obtain,

$$n_{\pm} = 1 - \lambda^2 \left(\frac{\overline{N}\,\overline{b}}{2\pi} \pm \frac{m\mu_n B}{h^2} \right) \tag{2.25}$$

From the above expression, we can see that the refractive index for neutrons is spin dependent. This property is extremely important and enables us to construct devices such as optical neutron polarisers, which allows one to select the neutron polarisation.

2.3.3 Mirror Reflection

Neutron guides and other such devices transport neutrons by the method of total external reflection. In the case of most substances we find that $\overline{b} > 0$ and therefore that the refractive index, $n < 1$. This means that a neutron passing from a vacuum into a medium, can, if the incident angle is sufficiently small, undergo total reflection. We can, by analogy, derive the critical angle at which reflection will take place from Snell's law for refraction, which states

$$n_{1,2} = \frac{\cos\theta_1}{\cos\theta_2} \tag{2.26}$$

Thus from Figure 2.3, we can see that the critical glancing angle is given by

$$n_{1,2} = \cos\theta_c \tag{2.27}$$

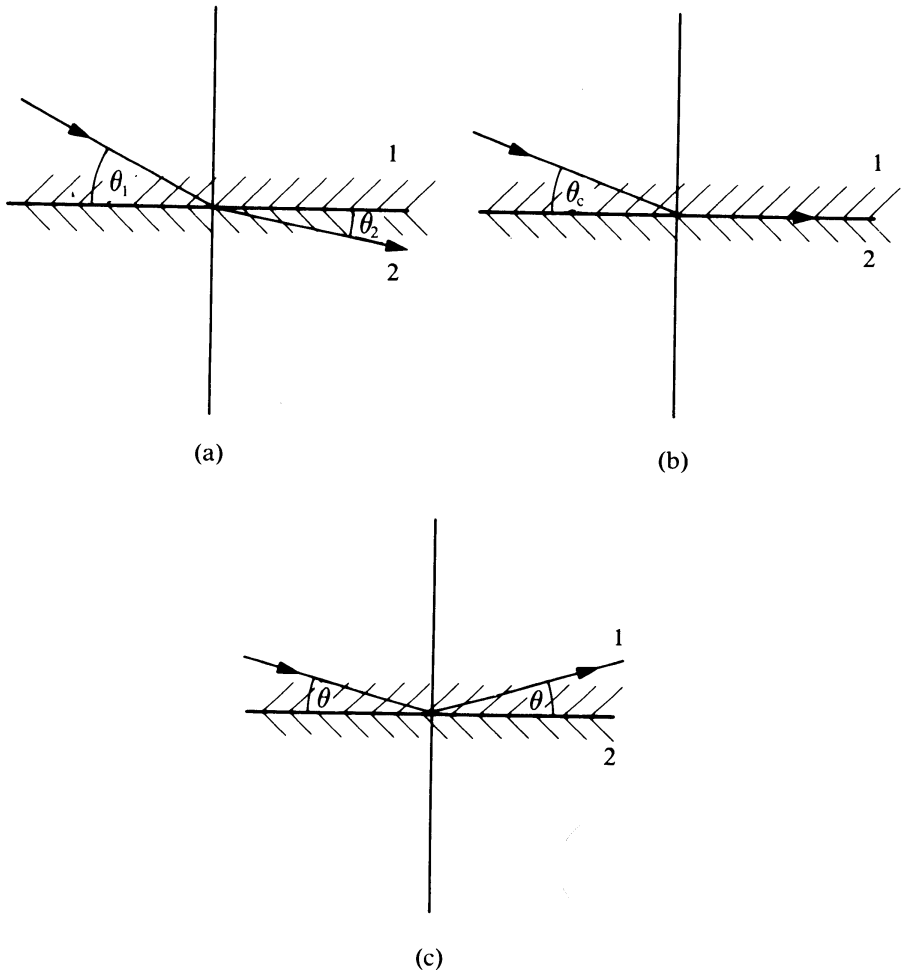

Figure 2.3: Neutron optical behaviour at an interface between media 1 and 2; (a) refraction, (b) critical glancing angle, and (c) total reflection (taken from Williams, 1988).

2.4 Quasi-elastic Neutron Scattering

If we start to consider inelastic scattering as opposed to the elastic scattering that has been considered so far then we must start to consider the time dependence of the scattering event. We now introduce a quantity that is know as the Double Differential Cross-section (DDCS) which is defined as

$$\left(\frac{d^2\sigma}{d\Omega dE'}\right) = \left(\frac{No.\,of\ \ particles\ scattered\ \ per\ unit\ time\ into\ d\Omega\ and\ dE'}{incident\ flux\ of\ \ energy\ E_0 \times d\Omega \times dE'}\right) \quad (2.28)$$

which is basically the probability that an incident neutron will be scattered by the sample into the solid angle $d\Omega$ about θ, with a final energy between *E'* and *E'+dE'*. In the present case we consider that the neutron undergoes an energy change due to random motion within the scattering volume (e.g. rotational or translational diffusion) producing a change in energy which is analogous to a Doppler shift. Quasi-elastic[2] scattering is distinct from true inelastic scattering due to the fact that no quanta of energy are absorbed or emitted by the system under study.

Van Hove (1954) first introduced the formalism for describing the DDCS in terms of a scattering function, $S(\mathbf{Q},\omega)$. For the case of incoherent scattering we define the incoherent scattering function, $S_{inc}(\mathbf{Q},\omega)$, which describes the distribution in the momentum, $(\hbar\mathbf{Q})$, and energy, $(\hbar\omega)$, transfer of the scattered neutrons, such that,

$$\frac{d^2\sigma_{inc}}{dE'd\Omega} = \left(\frac{\sigma_{inc}}{4\pi}\right)\left(\frac{k'}{k_0}\right)S_{inc}(\mathbf{Q},\omega) \tag{2.29}$$

and thus we also define the self correlation function, $G_s(\mathbf{r},t)$,

$$S_{inc}(\mathbf{Q},\omega) = \left(\frac{1}{2\pi}\right)\iint G_s(\mathbf{r},t)\exp[i(\mathbf{Q}\cdot\mathbf{r}-\omega t)]d\mathbf{r}dt. \tag{2.30}$$

where $\mathbf{k}_0$ and $\mathbf{k}$' represent the incident and final wave vectors which in turn define the neutron momentum transfer, $\hbar\mathbf{Q}$, by the relationship, $\mathbf{Q}=\mathbf{k}'-\mathbf{k}_0$. In an analogous way, we may define the coherent scattering function, $S_{coh}(\mathbf{Q},\omega)$ and the corresponding total correlation function, $G(\mathbf{r},t)$.

[2] The term "quasi…" derives from the Latin and literally means "as if it were" or "almost".

The scattering function is, in general, not symmetric due to factors such as the detailed balance condition, such that:

$$S(\mathbf{Q},-\omega)=e^{-\left(\frac{\hbar\omega}{kT}\right)}\cdot S(\mathbf{Q},\omega) \tag{2.31}$$

and hence the correlation functions are in general complex. For small ω, it is real and the self correlation function may be defined as the probability of finding a nucleus at position **r** at time *t*, given that the *same* nucleus was at the origin at *t*=0.

It should be pointed out that if one performs a time-of-flight experiment, then the relevant cross section that is measured is actually $\frac{d^2\sigma_{inc}}{d\Omega d\tau}$, where τ is the reciprocal velocity and is given by $\tau=\sqrt{\frac{m}{2E}}$.

We will now consider several models useful for describing the diffusive motions that are relevant to the studies performed in Chapter 5.

2.4.1 Jump Diffusion

The scattering function for times much greater than the jump time corresponding to this model is derived by solving Fick's 2nd Law, expressed in terms of the self correlation function:

$$D_t\nabla^2 G_s(\mathbf{r},t)=\frac{\partial}{\partial t}G_s(\mathbf{r},t) \tag{2.32}$$

where

$$\nabla^2=\frac{1}{\mathbf{r}^2}\frac{\partial}{\partial\mathbf{r}}\left(\mathbf{r}^2\frac{\partial}{\partial\mathbf{r}}\right) \tag{2.33}$$

for isotropic diffusion and D_t is the tracer diffusion coefficient. For the boundary condition that an atom is initially at the origin, $G_s(\mathbf{r},0)=\delta(\mathbf{r})$, the solution of equation (2.32) gives

$$G_s(\mathbf{r},t)=\left(4\pi D_t|t|\right)^{-\frac{3}{2}}\exp\left(-\frac{r^2}{4D_t t}\right) \tag{2.34}$$

The incoherent scattering function can be obtained by performing the Fourier transform of $G_s(\mathbf{r},t)$ in space and time (2.30) and therefore, we get;

$$S_{inc}(\mathbf{Q},\omega)=\frac{1}{\pi}\frac{D_t Q^2}{\left(D_t Q^2\right)^2+\omega^2} \tag{2.35}$$

This is a Lorentzian function in energy transfer with a full width at half maximum (FWHM) of $2D_t\mathbf{Q}^2$.

2.4.2 The Chudley-Elliott Model

This model describes quasi-elastic neutron scattering (QENS) for atoms hopping on a lattice. This idea was first proposed by Chudley and Elliott (1961). Although that their model was originally postulated for diffusive motions in liquids, it has found more applications in diffusion on a lattice. The Chudley-Elliott model involves the following assumptions:

- The diffusive motion is uncorrelated, (i.e. the jump direction of each jump is completely random).
- The lattice on which diffusion takes place is a Bravais lattice, (i.e. all sites involved are crystallographically equivalent. This includes, by definition, the same energy.)

- The residence time, τ, that a particle stays at a site is much larger than the time it takes to jump between sites.
- Only jumps between nearest neighbours are allowed.
- The diffusion is independent of other kinds of motion, in particular, vibrations.

The diffusion of an atom on a Bravais lattice which has *m* inter-site jump vectors, $\mathbf{l}_i$, may be described by the probability rate equation

$$\frac{\partial P(\mathbf{r},t)}{\partial t} = \frac{1}{m\tau}\sum_{i=1}^{m}\left[P(\mathbf{r}+\mathbf{l}_i,t) - P(\mathbf{r},t)\right] \tag{2.36}$$

where $P(\mathbf{r},t)$ is the probability of finding the particle at a distance $\mathbf{r}$ from an arbitrarily chosen origin. The self correlation function, $G_s(\mathbf{r},t)$, is the probability of finding the atom at $\mathbf{r}$ at the time *t*, for all possible starting positions.

$$G_s(\mathbf{r},t) \equiv P(\mathbf{r},t) \tag{2.37}$$

Introducing this into equation (2.36) and performing a Fourier transform in space, yields the rate equation for the intermediate function, $I(\mathbf{Q},t)$:

$$\frac{\partial I(\mathbf{Q},t)}{\partial t} = \frac{1}{m\tau}\sum_{i=1}^{m} I(\mathbf{Q},t)\left[e^{-i\mathbf{Q}\cdot\mathbf{l}_i} - 1\right] \tag{2.38}$$

with the boundary condition,

$$I(\mathbf{Q},0) = 1 \qquad \text{corresponding to} \qquad G_s(\mathbf{r},0) = \delta(\mathbf{r}) \tag{2.39}$$

The equation (2.38) is satisfied by substituting

$$I(\mathbf{Q},t) = I(Q,0)e^{-\Gamma(\mathbf{Q})t} \tag{2.40}$$

with

$$\Gamma(\mathbf{Q}) = \frac{1}{m\tau}\sum_{i=1}^{m}\left[1 - e^{-i\mathbf{Q}\cdot\mathbf{l}_i}\right] \tag{2.41}$$

Fourier transforming $I(\mathbf{Q},t)$ with respect to time, results in the incoherent scattering function;

$$S_{inc}^{CE}(\mathbf{Q},\omega) = \frac{1}{\pi}\frac{\Gamma(\mathbf{Q})}{[\Gamma(\mathbf{Q})]^2 + \omega^2} \tag{2.42}$$

which is a Lorentzian in energy with a half-width half maximum (HWHM) of $\Gamma(\mathbf{Q})$. The value of the width depends not only upon the residence time τ, but also on the geometry of the lattice sites. In a Bravais lattice, each site is an inversion centre; therefore, for each jump vector $\mathbf{l}_i$ there is a jump vector $-\mathbf{l}_i$.

The first experiment performed that tests the validity of the Chudley-Elliott model for hydrogen in metals was performed by Sköld and Nelin (1967) on a polycrystalline sample of Pd with small concentrations of hydrogen. For this case, equation (2.41) has to be averaged over all possible directions of the scattering vector. All the nearest neighbour jump sites have the same jump length ℓ between them, and therefore we get;

$$\Gamma(Q) = \frac{1}{\tau}\left(1 - \frac{\sin Q\ell}{Q\ell}\right) \tag{2.43}$$

If we expand this expression in the low-Q limit, in terms of $Q\ell$, up to the third order, gives

$$\Gamma(Q) = \frac{Q^2\ell^2}{6\tau} \tag{2.44}$$

and by substituting

$$D_t = \frac{\ell^2}{6\tau} \tag{2.45}$$

we get the result

$$\Gamma(Q) = D_t Q^2 \tag{2.46}$$

where D_t is the tracer diffusion coefficient. Therefore, in the low-Q limit, as $Q \rightarrow 0$, the scattering function reduces to the form given by the solution of Fick's law.

2.4.3 Jump Diffusion on Non-Bravais Lattices

The Chudley-Elliott model was extended for a general non-Bravais jump lattice by Blaesser and Peretti (1968) and later by Rowe *et al.* (1971) to the specific case of jump diffusion between the octahedral and tetrahedral sites in a bcc lattice and, subsequently, to the case of octahedral and tetrahedral sites in hcp lattices by Anderson *et al*. (1984). In these cases, due to the sites not being equivalent, we have to label each jump vector individually. The jump vectors are referred to in the notation $\mathbf{l}_{ijk}$, which represents a jump from the site of local symmetry *i* to the k^{th} site of local symmetry *j*. In order to simplify matters, the jumps are restricted to nearest-neighbour only with a single jump rate τ^{-1}, i.e. all jumps, even those to different sites with different symmetry, have the same probability, but for the case of different site energies, we need a different τ (Anderson *et al.*, 1984). This approximation is only realistic for the non interacting case and at low concentrations.

The probability of finding a atom at a position **r**, on a site of local symmetry *i*, is analogous to (2.36), and is given by

$$\frac{\partial P_i(\mathbf{r},t)}{\partial t} = \frac{1}{n\tau}\sum_{jk}\left[P_j(\mathbf{r}+\mathbf{l}_{ijk},t) - P_i(\mathbf{r},t)\right] \tag{2.47}$$

The sum over j, k is over all the *n* nearest-neighbour sites of the site *i*. The index *i* (*i*=1, 2, …, *m*) allows us to make a distinction between inequivalent types of sites, and we may write *m* equations to describe the probability of occupation of each type of site. The probability of finding an atom at any site in the unit cell at **r** is

$$P(\mathbf{r},t) = \sum_{i=1}^{m} P_i(\mathbf{r},t) \tag{2.48}$$

The self correlation function, $G_s(\mathbf{r},t)$, is the probability of finding the atom at **r** at the time *t*, given that the atom was at the origin, *j*, at *t* = 0, averaged over all possible starting positions of the atom.

$$P_j(\mathbf{r},t) = \sum_{i=1}^{m} P_i(\mathbf{r},t) \tag{2.49}$$

$$G_s(\mathbf{r},t) = \frac{1}{m}\sum_{j=1}^{m} P_j(\mathbf{r},t) \tag{2.50}$$

subject to the initial conditions

$$P_i(\mathbf{r},0) = \begin{cases} \delta(\mathbf{r}) & \text{if } i = j \\ 0 & \text{if } i \neq j \end{cases} \tag{2.51}$$

which ensures that the atom in question started on a site of local symmetry *j* at time zero.

$$\frac{\partial I_i(\mathbf{Q},t)}{\partial t} = \frac{1}{n\tau}\sum_{jk}\left[e^{-i\mathbf{Q}\cdot\mathbf{l}_{ijk}} I_j(\mathbf{Q},t) - I_i(\mathbf{Q},t)\right] \tag{2.52}$$

The equation (2.52) can be expressed in the form of a matrix, i.e.

$$\frac{\partial}{\partial t}[I]=[A][I] \tag{2.53}$$

where [A] is a $m \times m$ matrix, with elements

$$A_{ij}=\frac{1}{n\tau}\sum_{k} e^{-i\mathbf{Q}\cdot\mathbf{l}_{ijk}}-\frac{1}{\tau}\delta_{ij} \tag{2.54}$$

where the boundary conditions can be applied by Fourier transforming equations (2.48), (2.50), (2.51) obtaining

$$I^{j}(\mathbf{Q},t)=\sum_{i} I_{i}(\mathbf{Q},t) \tag{2.55}$$

and

$$I_{s}(\mathbf{Q},t)=\frac{1}{m}\sum_{j} I^{j}(\mathbf{Q},t) \tag{2.56}$$

subject to

$$I_{i}(\mathbf{Q},0)=\begin{cases}1 & \text{if } i=j\\ 0 & \text{if } i\neq j\end{cases} \tag{2.57}$$

The solution of equation (2.53) can be obtained by standard methods and are of the form

$$[I]=\sum_{j=1}^{m} C_{j}\boldsymbol{\alpha}_{j}e^{M_{j}t/\tau} \tag{2.58}$$

where M_j are the eigenvalues of the matrix [A] and $\boldsymbol{\alpha}_j$ is the eigenvector. The eigenvalues correspond to the widths of the different Lorenztian components of the quasi-elastic peak and the eigenvectors relate to the weights of the Lorenztian.

The dynamical matrix [A] can be evaluated by assigning a value, *i*, to each of the different site symmetries of the interstitial lattice and then considering which of the symmetries *j* are nearest neighbours. The matrix elements are calculated by applying equation (2.54). The matrix [A] for a bcc host lattice is given by Rowe *et al* (1971) and can be expressed as

$$[A]=\frac{1}{4}\begin{pmatrix} -4 & 0 & E_1 & E_4 & E_2^* & E_5^* \\ 0 & -4 & E_4^* & E_1^* & E_5 & E_2 \\ E_1^* & E_4 & -4 & 0 & E_3 & E_6 \\ E_4^* & E_1 & 0 & -4 & E_6^* & E_3^* \\ E_2 & E_5^* & E_3^* & E_6 & -4 & 0 \\ E_5 & E_2^* & E_6^* & E_3 & 0 & -4 \end{pmatrix} \tag{2.59}$$

where

$$\begin{aligned} E_1 &= e^{\frac{ia\mathbf{Q}}{4}\cdot(0,1,1)} \\ E_2 &= e^{\frac{ia\mathbf{Q}}{4}\cdot(1,0,1)} \\ E_3 &= e^{\frac{ia\mathbf{Q}}{4}\cdot(1,1,0)} \\ E_4 &= e^{\frac{ia\mathbf{Q}}{4}\cdot(0,-1,1)} \\ E_5 &= e^{\frac{ia\mathbf{Q}}{4}\cdot(-1,0,1)} \\ E_6 &= e^{\frac{ia\mathbf{Q}}{4}\cdot(-1,1,0)} \end{aligned} \tag{2.60}$$

where E^* represents the complex conjugate of E, it arises from the negative jump vectors.

At finite concentrations, we start to experience correlation effects, which are difficult to account for analytically, therefore a Monte Carlo approach is better suited (Bull, 1998).

Chapter 3

Neutron Instrumentation

3.1 Introduction

The relevant concepts needed to describe the operation of an inverted[1] geometry spectrometer such as OSIRIS will be discussed, pointing out known problems along with suggestions on how they might be improved. A number of actual instruments will also be described, the instruments chosen either have similarities in operation or use to OSIRIS, or have been used to carry out experiments that are included later in this thesis. For completeness, a description of a muon spectrometer is also included.

A neutron instrument can be thought of as two main sections; a primary and a secondary spectrometer. The primary spectrometer contains components such as a wave-tube or neutron guide, polarisers, collimators and also energy definition devices (monochromator or choppers), as well as one of the most crucial parts, the source of neutrons. A useful schematic diagram of an inverted geometry instrument can be seen in Figure 3.10.

3.2 Detection of neutrons

Since neutrons have no charge, the usual methods of detecting a particle by collecting the charge produced as it ionises the medium of the detector cannot be used. Therefore we must first use the neutron to create charged particles in a nuclear reaction. The three most commonly used in neutron detectors are:

[1] a type of neutron spectrometer in which the detected neutron energy is fixed.

$$^{3}He + n \rightarrow {}^{3}H + p + 0.764\,\text{MeV} \quad \text{(a)}$$
$$^{10}B + n \rightarrow {}^{7}Li + {}^{4}He + 2.785\,\text{MeV} \quad \text{(b)}$$
$$^{6}Li + n \rightarrow {}^{4}He + {}^{3}H + 4.78\,\text{MeV} \quad \text{(c)}$$

Here we will only describe the two types of detector that are to be installed in the main detector banks of the OSIRIS spectrometer. The inelastic detector bank will employ a series of He gas tubes and the diffraction detector will consist of a large position sensitive ZnS sintillator detector.

3.2.1 The 3He Gas Detector

This is basically a stainless steel tube that is filled with a given pressure (a usual figure is ~10 bars) of ^{3}He gas (see reaction (a) above) that has a thin wire anode running through its centre. The electrons that are produced from ionization of He molecules, and are collected by the anode, which registers the existence of a neutron as a small pulse of current. The dead time depends on the size and voltage of the counter, but is usually in the order of 2 μs.

3.2.2 The Zinc Sulphide Detector

The gas detector has one main important restriction, which is the pressure of gas that can be inside the tube. The effective length of a tube cannot be reduced below ~1 cm, if we still wish to preserve the efficiency. A scintillator uses a much denser neutron absorber to give comparable efficiencies within a few millimetres. One such typical absorber is ^{6}Li (reaction (c) above). The products of the reaction are detected by a crystal such as ZnS. This is often mixed with the absorber, and emits a flash of light as the ionising particle passes through it. This light is then detected by a photomultiplier tube. One major drawback is that this type of detector is very sensitive to γ-rays so we have to employ a coincidence

methods to determine what is a ‘true’ count. These detectors are also useless in the presence of a strong magnetic field.

3.3 Neutron Transport

3.3.1 Supermirrors

Supermirrors are becoming more widely used as a coating for neutron guides due to their improved transmission over more traditional nickel coated guides. A supermirror basically comprises a stack of metallic bilayers (usually Ni/Ti) with varying thicknesses (ranges from ~40 Å to ~300 Å), in order to extend the region of total reflection of a neutron from a surface. The range to which the critical angle has been extended is often referred to as the *m*-value. In this case the *m* represents the critical angle of a normal nickel coated surface (e.g. a 2*m* supermirror has a critical angle twice as large a normal nickel). In Figure 3.1 we can see how the reflective characteristics of different types of surface alter with angle. For a single monolayer reflective material, we will get total reflection upto some critical angle, θ_c, and for the case of a multilayer (with constant layer spacing) we will also observe an additional “pseudo” Bragg peak at an angle corresponding to the spacing between the layers. Whereas for the case of a supermirror, which has a varying bilayer thickness, we see a number of these “pseudo”-Bragg peaks which overlap each other with the effect of extending the total angle over which neutrons are reflected, this was first suggested by Mezei (1976). The layer spacings for the supermirrors used in the construction of the OSIRIS spectrometer were obtained by employing an algorithm developed by John Hayter (Hayter & Mook, 1989).

Supermirrors have found uses in many neutron optical devices, such as guides and polarising benders, which will be discussed later. An overview of the development of supermirrors can be found in Anderson (1992).

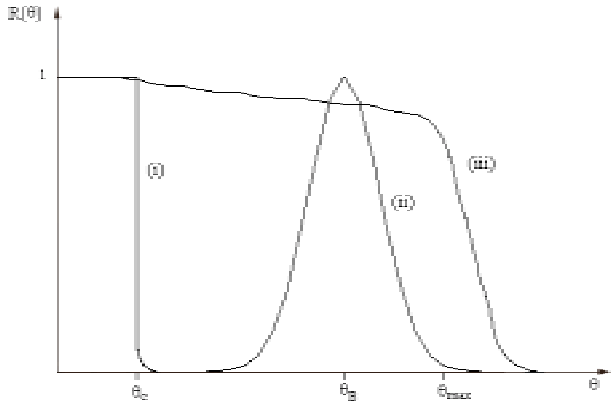

Figure 3.1: A schematic sketch of how the reflectivity of a surface compares for a (i) monolayer reflective surface, (ii) a multilayer of constant thickness and (iii) a supermirror.

3.3.2 Neutron Guides

As mentioned earlier the neutron exhibits a number of wave like properties (c.f. Chapter 2) and hence it is possible to construct devices that take advantage of this characteristic. Maier-Leibnitz and Springer (1963) first pointed their possible use. Neutron guides provide a method of transporting a neutron beam over a long distance with little loss in intensity and over areas that are determined by the guide's cross-section. If we assume that the guide surfaces are coated with the same material, then the neutron guide will transmit all neutrons lying within a solid angle of $4\gamma_c^2$, where γ_c is the critical glancing angle of a neutron at the surface. This can be particularly important in making it possible to locate samples in remote areas of low background, well away from the actual source.

Neutron guides have been used extensively at steady state reactor sources, but here we will concentrate on their use at a pulsed source. What follows is a brief overview of some of the theoretical and practical aspects of using a neutron guide as part of an instrument on a pulsed source (Carlile *et al.*, 1979).

One aspect of neutron guides that is useful, especially at pulsed sources is that if we use a straight guide, then we may have large fluxes of high energy neutrons

and gamma rays hitting the sample. One method of significantly attenuating these, is by curving the guide over a distance that is greater than the "line of direct sight", L_0 (Figure 3.2). For a curved guide, which has an aperture of *a* in the plane of curvature, the "direct line of sight" is given by;

$$L_0 = \sqrt{8aR} \tag{3.1}$$

this is related to a characteristic angle γ^* by

$$\gamma^* = \sqrt{\frac{2a}{R}} = \frac{L_0}{2R} \tag{3.2}$$

Neutrons which have wavelengths, $\lambda < \lambda^*$ are transmitted only by single or garland reflections along the outer concave surface of the guide. Neutrons with $\lambda > \lambda^*$ will be transmitted by both zig-zag and garland reflections. One consequence of this, is that at wavelengths ~λ^*, the beam profile at the guide exit is asymmetric, and this situation worsens as we decrease the wavelength.

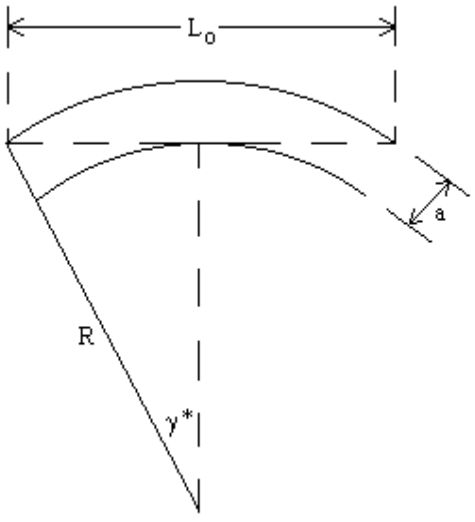

Figure 3.2: Definition of the line of sight, L_o and characteristic angle γ^* for a circularly curved guide.

3.3.2.1 Converging Guides

Converging guides provide a useful way of achieving an increase in intensity on a smaller area in a manner analogous to that of an optical lens. The main use of this type of guide is at the end of length of neutron guide, immediately before the sample, in order to reduce (or focus) the beam onto the sample. This can result in an appreciably enhanced flux, with only a relatively modest loss in total intensity. It should also be noted, that by having a converging guide section before the sample, it is possible to reduce the sample size thereby increasing the time-of-flight resolution. There is an undesirable effect of an increased beam divergence, so positioning the sample at the correct distance from the guide exit becomes crucial. The optimisation of these components can be achieved by either analytical calculations or Monte Carlo simulations.

3.3.2.2 Loss Mechanisms within Neutron Guides

The basic theory of neutron conduction in guides applies to an ideal case, in which the guide is perfectly smooth, continuous and which have reflectivities of 100%. There are a number of processes which introduce a reduction in the ideal case;

- **Penetration depth**
- **Microscopic surface defects** - *introduce step discontinuities in the surface (atomic dislocations, grain boundaries, crystal plane slips)*
- **Macroscopic surface defects** - *due to a physical roughness or waviness*
- **Imperfect mechanical construction**
    - $\Rightarrow$ Imperfect spatial alignment
    - $\Rightarrow$ Gaps between sections
    - $\Rightarrow$ Imperfect angular alignment
    - $\Rightarrow$ Curved guides constructed from straight sections

3.4 Polarised Neutrons

There are many methods that may be employed to produce a polarised neutron beam. What follows is a description of the main tried and tested experimental apparatus in this area as well as some selected instrumentation used in conjunction with polarised neutron beams. An important parameter in determining how good a neutron polariser is its polarising efficiency *P*. This is defined as the polarisation of the outgoing beam after an unpolarised beam passes through it, and may be expressed as,

$$P = \frac{N_{\uparrow} - N_{\downarrow}}{N_{\uparrow} + N_{\downarrow}} \tag{3.3}$$

where $N_{\uparrow}$ and $N_{\downarrow}$ are number of $\uparrow$ and $\downarrow$ spin neutrons in the outgoing beam. For the case were $P=0$, then the neutron beam is unpolarised. The main other factor is the intensity lost during the polarisation process.

3.4.1 Polarising Benders

A polarising bender is very similar in concept to a Soller type collimator, in that it consists of a number of vertical dividers which have polarising supermirror deposited onto their surface, thus creating many channels through the device (see Figure 3.3 and Figure 3.4). If we now curve these substrates to a sufficient degree so that we no longer have a direct line of sight through the device, then neutrons entered this section must undergo at least one reflection in order to reach the other side. The blades of such a device are usually parallel but it is possible to arrange them so they also focus the beam (Hahn and Schweika, 1997).

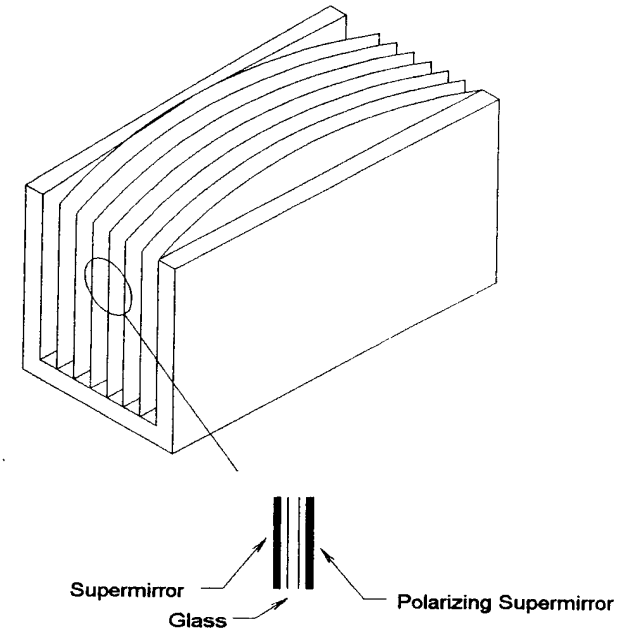

Figure 3.3: A schematic representation of a polarising bender.

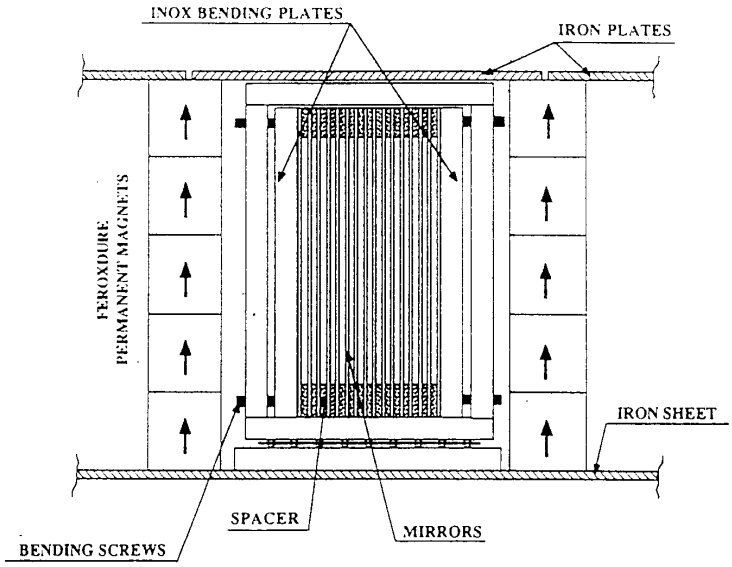

Figure 3.4: A cross sectional view of a polarising supermirror bender as used on the D7 instrument at the ILL. (Schärpf, 1989b). The feroxide magnets shown are to produce the field mentioned in section 2.3.2.

3.4.2 He^3 Filter

These in contrast to optical polarisers, such as benders, show greater potential for higher energy neutrons, where the critical angle would be very small, and therefore we would obtain poor transmission in the case of optical polarisers. Another possible use of such a filter would be in instruments which require large divergent beam areas to be polarised, such as in a scattered beam spin analyser. The basic technique relies on the fact that the neutron cross section of He^3 for absorption is highly spin dependent. Therefore if we have a cell of polarised He^3 then the cross section for parallel spins is huge (~3000λ) and so only neutrons with spins anti-parallel are transmitted (Figure 3.5).

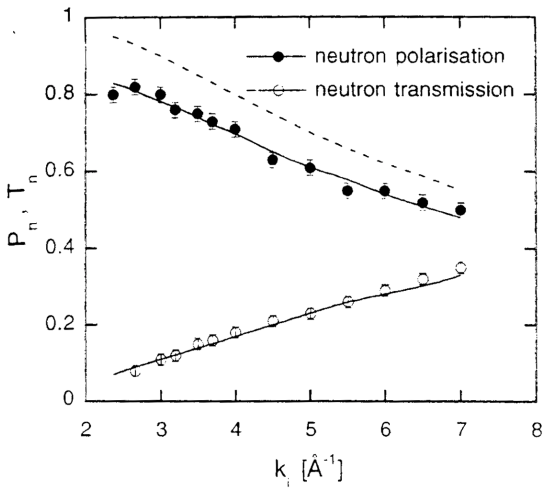

Figure 3.5: Measured neutron polarisation and transmission for an ILL He^3 filter. The dotted curve represents the neutron polarisation corrected for losses in the magnetic shielding (Kulda et al. 1998).

3.4.3 Spin Flippers

Once we have polarised a neutron beam we might want to alter the orientation of the polarization with respect to the sample (or other spectrometer components). In general, the polarisation is either required to be reversed (π-flipper) or rotated by 90° (π/2-flipper). There are many different types of spin flipper, a description of the main types can be found in Williams (1988).

3.5 Neutron Energy Selection

3.5.1 Monochromators and Analysers

Crystal Monochromators are widely used at neutron facilities, more so at a steady state source than a pulsed, due to their use as incident wavelength selectors. Pulsed sources generally use high speed Fermi choppers for this purpose, but it must be stressed that this statement is not necessarily true as there is no reason why monochromators could not be used to define the incident energy of a pulsed spectrometer. The use of a monochromator in the scattered beam as an energy analyser is identical at both steady and pulsed sources.

Monochromators are single crystals that select a neutron energy by means of Bragg reflection, so for a white beam, the neutron wavelength that is selected, satisfies the Bragg condition

$$n\lambda = 2d\sin\theta \tag{3.4}$$

where d is the separation of the reflecting planes and θ is the angle subtended between the incident beam and the crystal planes. If we differentiate Bragg's Law, $\lambda = 2d\sin\theta$, we obtain an expression for the resolution

$$\frac{\Delta\lambda}{\lambda} \approx \cot\theta\,\Delta\theta + \frac{\Delta d}{d} \tag{3.5}$$

By using the relationship

$$E = \frac{p^2}{2m} = \frac{h^2}{2m\lambda^2} \tag{3.6}$$

we get an expression for the energy resolution;

$$\frac{\Delta E}{E} = \frac{2\Delta\lambda}{\lambda} = 2\cot\theta\Delta\theta + \frac{2\Delta d}{d} \qquad (3.7)$$

From this we can see that as we move towards exact backscattering geometry (i.e. as $2\theta \rightarrow \pi$), the cotθ term goes to zero. In this limit, the energy resolution is dependent only upon the fractional uncertainty in the lattice parameter. This idea is employed in high-resolution backscattering spectrometers, such as IN10 at the ILL.

3.5.2 Thermal Diffuse Scattering and Effect of Cooling Analyser Crystals

One of the main drawbacks of a high resolution indirect geometry (fixed E_f) instrument such as OSIRIS/IRIS is its analyser-detector configuration, it is very susceptible to any non-Bragg diffraction process in the analysers. In the case of a pyrolitic graphite analyser, we have a incoherent scattering cross section of approximately zero, but we may have coherent inelastic scattering from phonons which is called thermal diffuse scattering (TDS). In an analyser consisting of mica, in which the non-specular scattering is predominately incoherent (due to the large OH^- ion content) there is very little contribution from TDS. Therefore if we choose to have a graphite analyser then the resolution function at room temperature will be the characteristic asymmetric peak of pulsed instruments with an underlying broad flat background due to TDS. It is known (Carlile *et al.*, 1994) that the ratio of the elastic peak height to the broad background is about 120. In Figure 3.6 we can see the spectrum obtained on IRIS using its diffraction detector with a graphite crystal sample, that has been illuminated by a white beam. It is shown as a function of angular offset from the Bragg condition. We can see two distinct wings that represent phonon creation and annihilation (Willis *et al.*, 1986), that when added together result in the broad underlying feature that can be seen in a single detector.

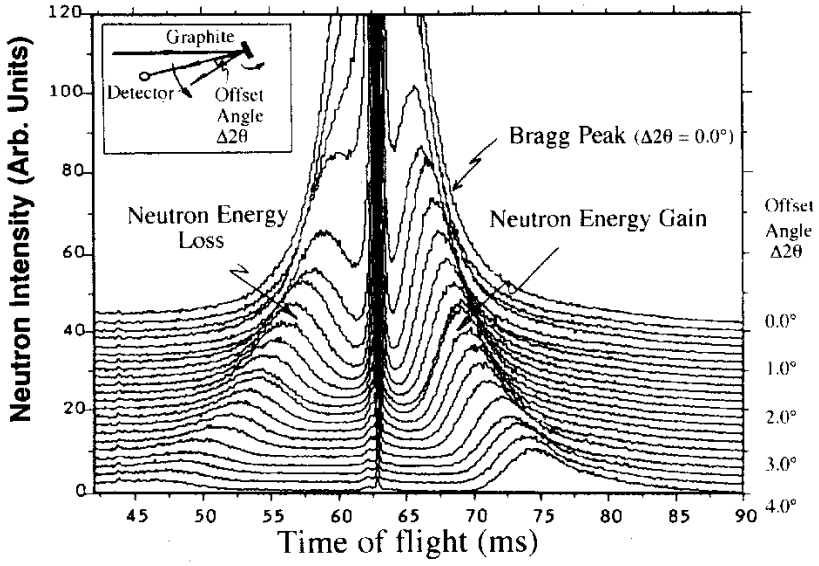

Figure 3.6: Single crystal of pyrolitic graphite diffraction pattern shown as a function of offset angle from the Bragg condition (Carlile et al.*, 1994).*

A method of reducing the TDS intensity when we move away from the Bragg condition would be to introduce collimation between the analyser and the detector, but this would be useless for the most intense contribution to the TDS signal, as it is, in and around the position of the Bragg peak. It would however be of use to perform a detailed study to investigate the effect of collimation on TDS, and how severe the collimation would have to be in order to have any noticeable effect on the TDS.

Another method, and the one employed on IRIS, is to cool down the analysers in order to reduce the phonon population and therefore minimise the effects of TDS. Figure 3.7 shows the effect of reducing the temperature on the diffraction pattern observed at an offset of 4° from the (002) Bragg condition. It has been shown by Carlile *et al.* (1994) that the integrated TDS intensity for phonon creation and annihilation is roughly linear with temperature. The result of cooling the analysers on IRIS to 25 K, has been a reduction in the signal to background from 120-to-1 to 1350-to-1. It is expected that a further reduction in temperature to 5 K (Balchin, 1996) would yield a further reduction in the background by a factor

of 4. The disadvantage in this solution is that the cooling system required is costly and technically complicated.

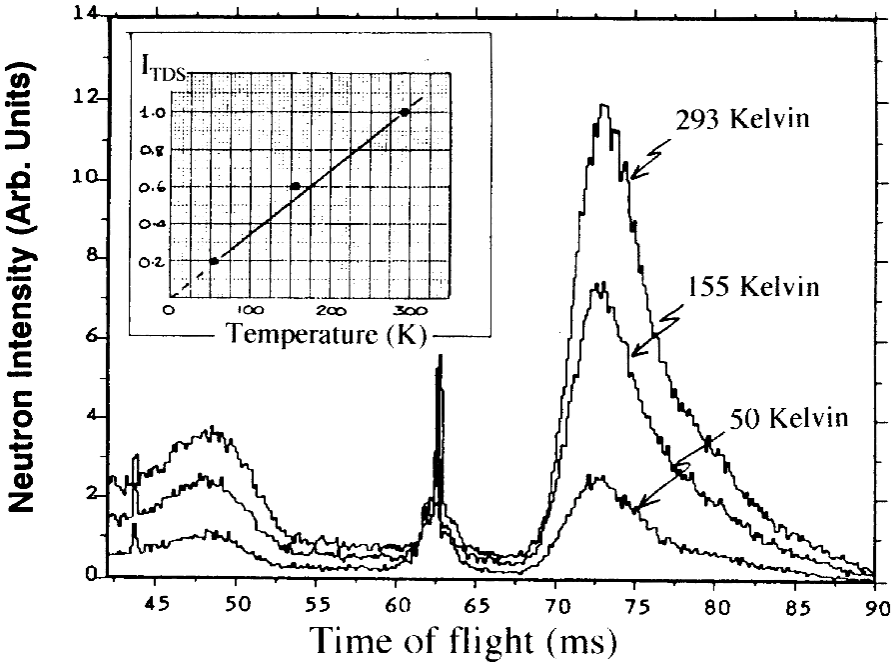

Figure 3.7: Scattering patterns from pyrolitic graphite showing the reduction in intensity of the phonon peaks with fall in temperature (Carlile et al.*, 1994).*

3.5.3 Choppers

In a disc chopper (Figure 3.8) a large disc rotates perpendicular to the direction of the neutron beam with its axis of rotation parallel to the beam. The outer edge of the disc consists of a neutron absorber, except for a "window" which is transparent to neutrons. As this "window" passes through the incident beam, we will get a range of times corresponding to a range of neutron wavelengths that are transmitted. This type of chopper is mainly used to prevent frame overlap on pulsed sources or as one element of a phased chopper system on a steady state source.

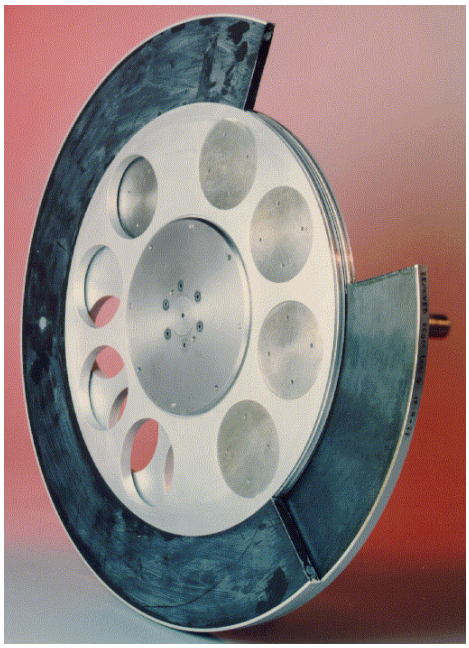

Figure 3.8: A neutron disc chopper.

In addition to disc choppers, there are two further types that are employed particularly at pulsed sources, a Fermi and the T_0 or "nimonic" chopper. A Fermi chopper is usually used as a method of defining a particular incident energy for a direct geometry spectrometer. It consists of a number of parallel slits, which rotate at a high frequency, so that only a particular neutron energy will be able to travel through the slit package in the required time. A nimonic chopper on the other hand shuts off the beam at zero time in order to protect spectrometer components from the very high energy neutrons.

3.6 Neutron Instruments

3.6.1 The High Resolution Inelastic Spectrometer, IRIS

The IRIS spectrometer (as shown in Figure 3.9) is similar in concept to the OSIRIS spectrometer the design of which is discussed in a later chapter, but there is a number of important differences between the two instruments. Carlile and Adams (1992) have given a more complete description of the IRIS spectrometer.

The main spectrometer sits at the end of a 36.5 m long curved neutron guide which views the liquid hydrogen moderator of the ISIS source.

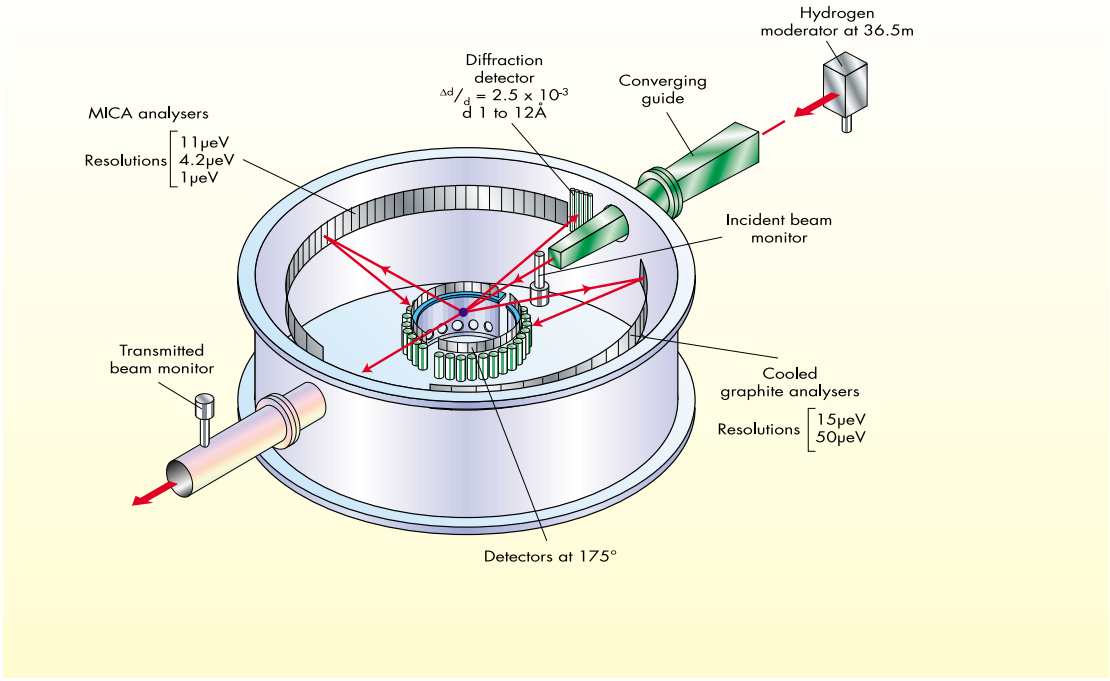

Figure 3.9: The IRIS high-resolution spectrometer at the ISIS pulsed neutron source.

The sample is illuminated by an incident white pulsed neutron beam, the energy of the neutrons is determined by the time-of-flight technique. It is important that we can accurately measure the incident energy to micro-electronvolt precision hence the long incident path. The scattered beam is analysed by one of two banks of single crystals which reflect a single neutron energy to the ZnS scintillator detectors that are situated in just off backscattering geometry (θ_B=87.5°). The scattering angle covered by the analyser crystals is 15° to 165°, which consists of either pyrolytic graphite or muscovite mica elements. The resolution may be altered by choosing different diffraction orders of the analysers, which gives us values of ΔE ranging from 1.1 μeV to 50 μeV. A summary of the individual settings can be seen in Table 3.1.

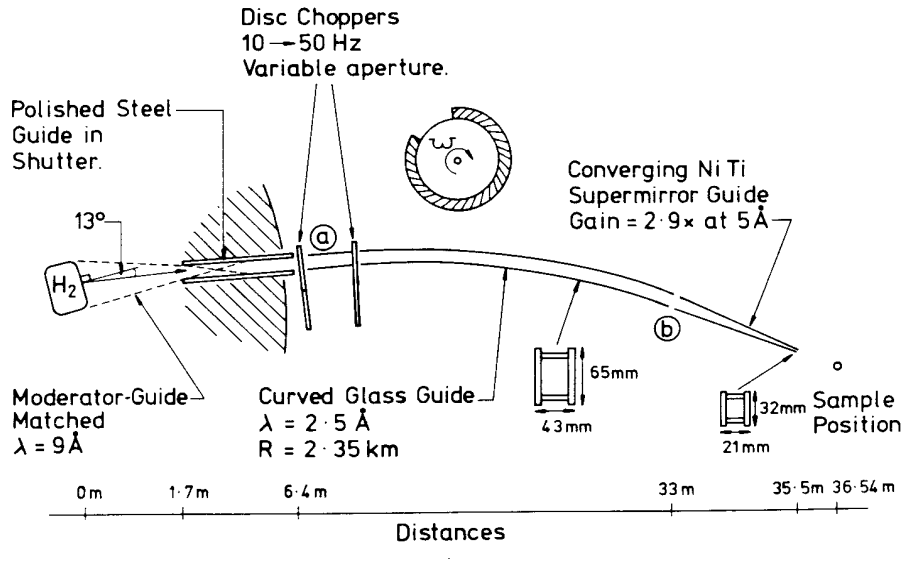

Figure 3.10: The primary flight path of the IRIS spectrometer (taken from Carlile and Adams; 1992)

In having the sample illuminated by an incident white beam it is possible in theory to perform simultaneous diffraction and spectroscopic measurements, but on many instruments this is impossible to achieve in practice due to the geometry of the instrument. However, on IRIS this can be easily performed, by situating a diffraction detector consisting of ten high-pressure He^3 tubes at a scattering angle of approximately 175°. This yields a resolution of $\Delta d/d = 2.5 \times 10^{-3}$ over a d-spacing range of 2 to 13 Å.

Table 3.1: Characteristics of the IRIS analyser arrays.

Analyser Reflection	*Analyser wavelength (Å)*	*Analyser energy (meV)*	*Energy resolution (μeV)*	*Energy and momentum transfer ranges*
Mica (002)	19.8	0.208	1.1	-100 to +300 μeV 0.1 to 0.6 $Å^{-1}$
Mica (004)	9.9	0.832	4.2	-400 to +500 μeV 0.2 to 1.2 $Å^{-1}$
Mica (006)	6.6	1.87	11	-0.5 to +1 meV 0.3 to 1.8 $Å^{-1}$
Graphite (002)	6.7	1.82	15	-0.8 meV to +2.2 μeV 0.3 to 1.8 $Å^{-1}$
Graphite (004)	3.35	7.28	50	-3 meV to +5 μeV 0.5 to 3.7 $Å^{-1}$

3.6.2 The IN10 High Resolution Back-scattering Spectrometer.

The IN10 spectrometer (Figure 3.11) is situated at the ILL, Grenoble. It has a high resolution that is achieved mainly through the back scattering arrangement of the scattered beam analysers. It is located 50 m from the reactor core on the H15 curved neutron guide. The incident beam energy is selected by means of a monochromator crystal, which is driven by a Doppler drive in order to obtain a small range of neutron wavelengths. These are then deflected by a (002) orientated pyrolytic graphite crystal (which is situated just below the incoming primary beam) towards the sample. Before the sample, the neutrons pass through a chopper and incident beam monitor. The scattered neutrons are analysed by an array of crystals which are situated on a spherical surface that is centred on the sample. The analysed neutrons are focussed onto an array of eight ^{3}He detectors, situated behind the sample. The chopper is phased to the counting electronics so that neutrons that are scattered directly into the sample are not counted. The whole of the secondary spectrometer (from the graphite deflector) can be rotated around the incident beam. Both the monochromator and the analyser crystals can be altered in order to give a range of incident energies, count rates and resolutions (full characteristics are shown in Table 3.2). In addition to the Doppler driven monochromator, there is the option to use a monochromator that is thermally cycled to vary its d-spacing and thereby produce a spread of wavelengths.

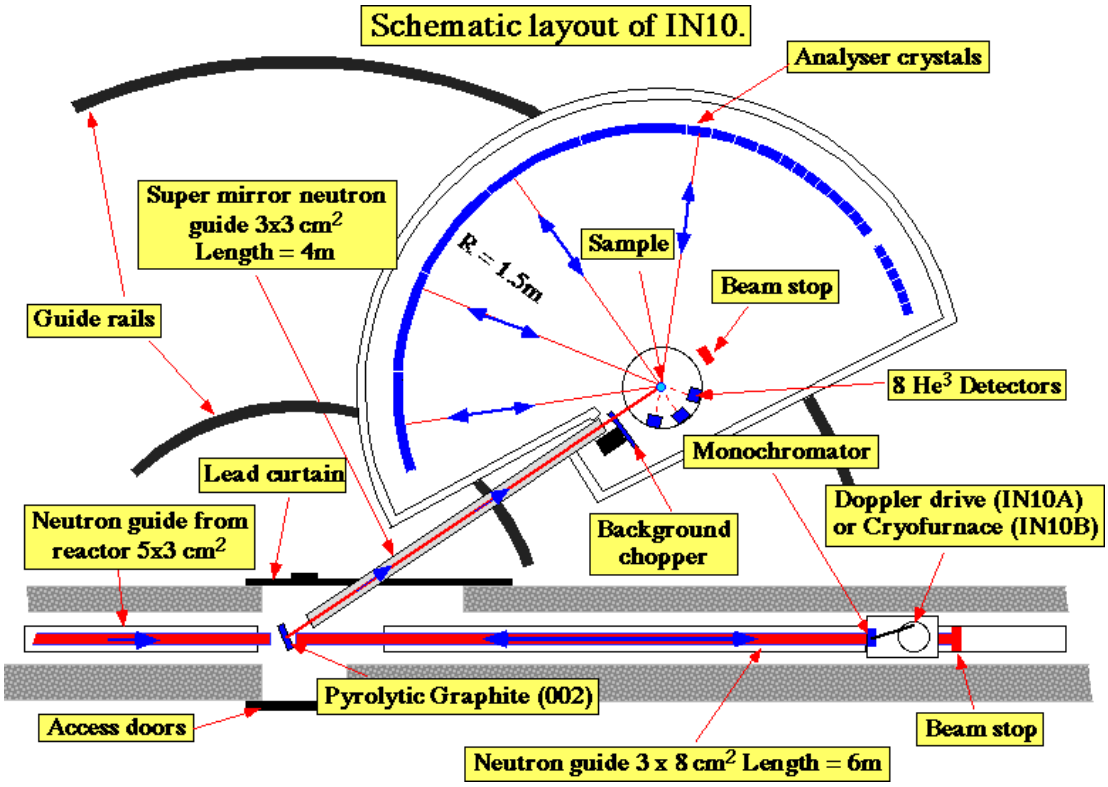

Figure 3.11: Layout of the IN10 back-scattering spectrometer at the ILL.

Table 3.2: Characteristics of the IN10 spectrometer for different monochromator/analyser configurations.

IN10A					
monochromator	Si(111)	Si(311)	$Si_{0.9}Ge_{0.1}$(111)	CaF_2(111)	Ge(111)
analyser	Si(111)	Si(311)	Si(111)	Si(111)	Si(111)
flux at sample in n $cm^{-2}s^{-1}$	$4x10^3$; (polished) $2x10^4$ (unpolished)	$2x10^3$	$3x10^4$	$2x10^4$	$4x10^4$
incident energy	2.080	7.627	2.06	2.056	1.92
incident wave length λ in Å	6.271	3.275	6.30	6.308	6.53
energy transfer range ΔE in µeV	−15 to +15	−28 to 28	−2 to 27	9 to 39	148-178
energy resolution δE in µeV (FWHM)	0.3-1.5	2-4	1	0.8-1.5	1
elastic Q-range in $Å^{-1}$	0.07-2.0	1.7-3.7	0.07-2.0	0.07-2.0	0.07-1.9
beam size at sample	3.5x3.5 cm^2				

3.6.3 The Diffuse Scattering Spectrometer, D7 with Polarisation Analysis.

A schematic diagram of the general layout of the instrument is shown Figure 3.12. The incident beam is monochromated by a triple, horizontally and vertically focusing graphite monochromator. Due to the configuration of the machine, different wavelengths can be selected by moving the entire instrument around an axis centred on the monochromator. The incident beam is passed through a supermirror polarising bender and then through a spin flipper. The flipper is a coil device that flips the neutron spin direction by π when activated. After this, the beam is passed through a four slit disk chopper to produce the time-of-flight pulse. Alternatively, a pseudostatistical chopper may be used.

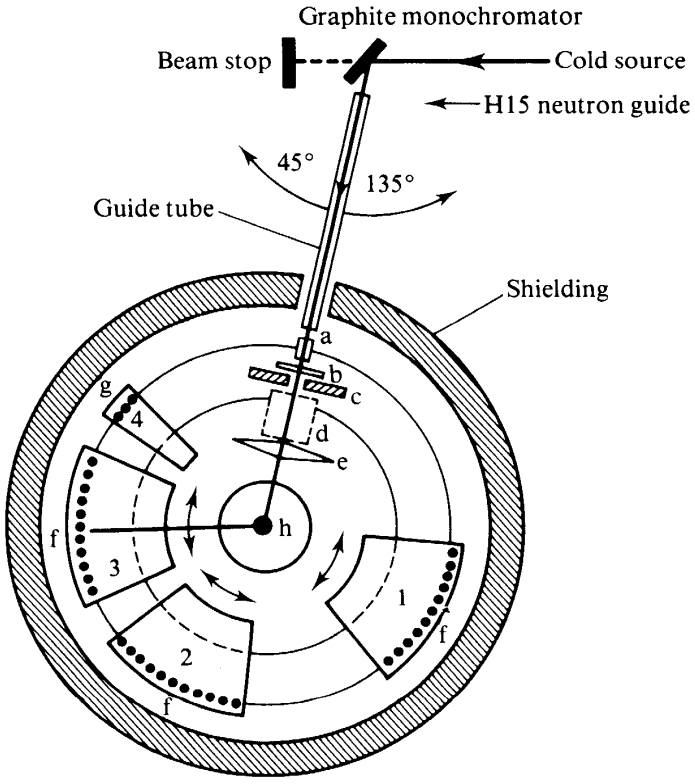

Figure 3.12: Schematic diagram of the diffuse scattering instrument D7 at the ILL, Grenoble. (a) Be filter or polarizer; (b) main monitor; (c) slit system; (d) flipper and second polarizer for psueudostatistical chopper; (e) disc chopper or flipper; (f) detector banks 1-3 with supermirror polarizing Sollers; (g) vertical detector bank 4; (h) sample, (taken from Bank and Maier, 1988).

3.6.4 Time-Focused Crystal Analyser Spectrometer, TFXA.

A more detailed description of TFXA can be found in Penfold and Tomkinson (1986). This instrument (see Figure 3.13) is an inverted geometry spectrometer which also uses a graphite crystal to define a final energy of 4 meV for a wide range of incident energies. It gives very good resolution ($\hbar\omega \leq 2\%$, $\Delta Q \approx 0.2 Å^{-1}$) at incident energies below about 100 meV. Due to the fact that a white beam is incident on the sample, generally speaking, we would expect to have a relatively high background. Also since Q increases as $E^{½}$, the Debye-Waller factor drastically reduces the intensity of the higher energy hydrogen modes. In addition, it is worth noting that there are a number of diffraction detectors situated around the sample. This enables us to measure an in-situ diffraction pattern and confirm the phase of the sample under investigation.

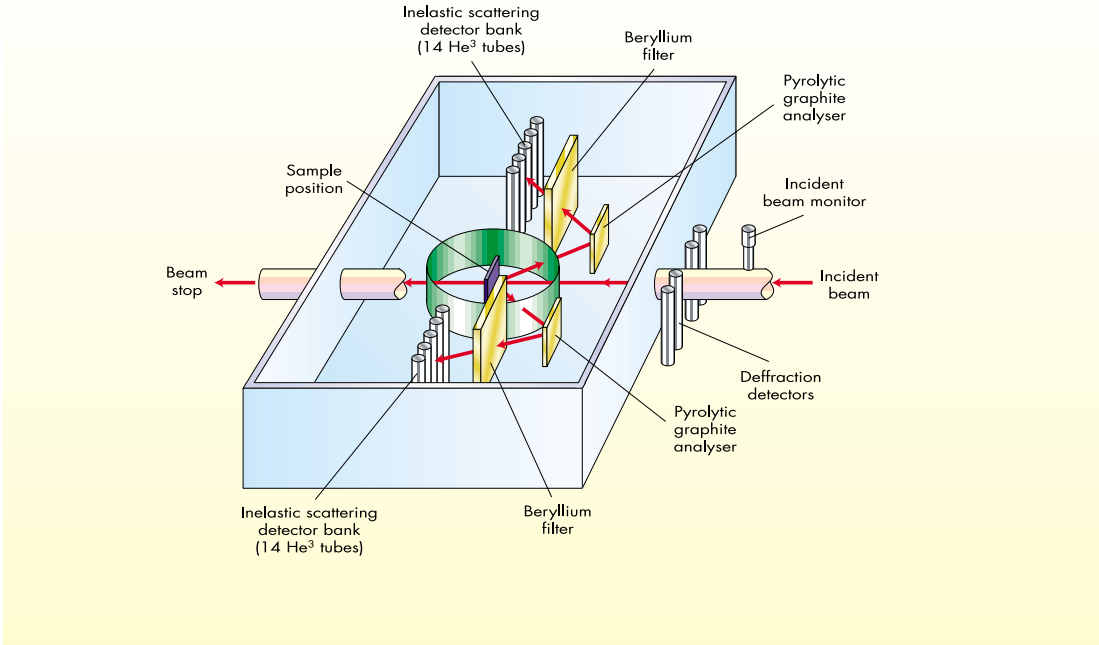

Figure 3.13: The TFXA crystal analyser spectrometer at the ISIS Facility.

3.6.5 The MuSR Muon Spectrometer at ISIS.

This instrument differs from others described here in that it uses muons not neutrons to probe the sample under investigation. The main detector banks are situated in a ring around the sample and are positioned symmetrically in forward and backward scattering directions (see Figure 3.14), when the spectrometer is in its longitudinal configuration (which was used for all the measurements that are presented here). The measurement time to collect ~15 million events that are necessary for good statistics is approximately 45 mins. A detailed description of the technique can be found in chapter 5.

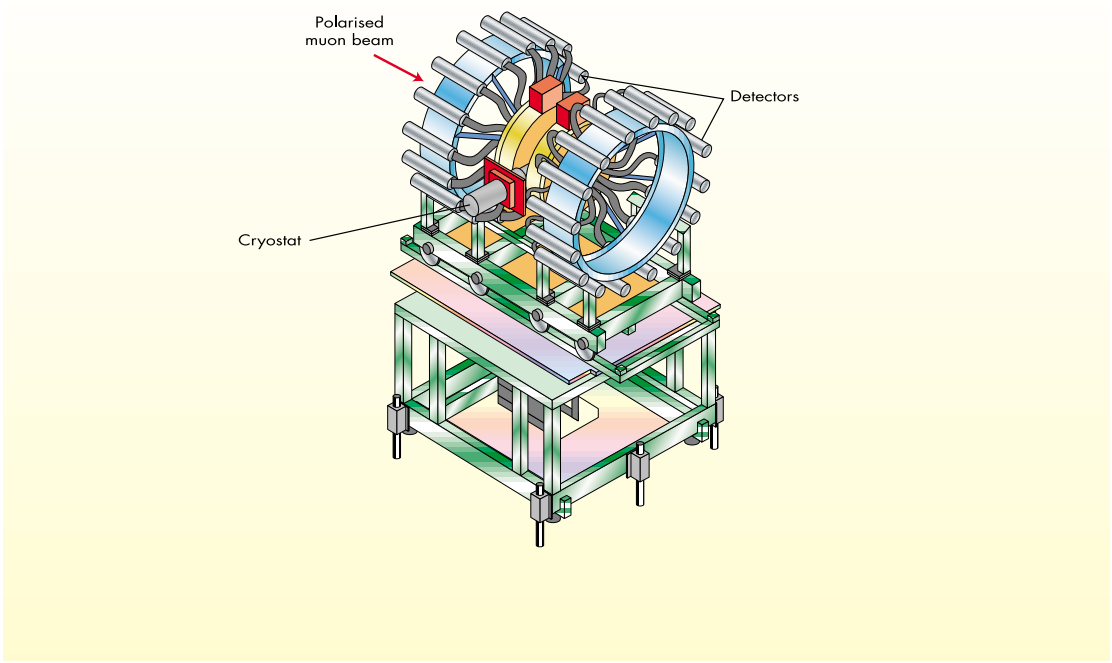

Figure 3.14: The MuSR muon spectrometer situated at the ISIS Facility, Rutherford Appleton Laboratory.

Chapter 4

The Design and Simulation of the OSIRIS Spectrometer.

4.1 Introduction

This chapter describes a number of studies that have made use of the Monte Carlo technique. One of the main uses of these simulations was to optimise the geometry for the neutron polarising benders. Also discussed are various issues that arose during the construction of the spectrometer in which the use of simulations proved a valuable tool in assessing the impact on the spectrometers performance. Below is a brief description of its basic concepts and uses, and why it is becoming such an important tool for neutron instrument design.

4.2 Overview of the OSIRIS Project.

The main function of the OSIRIS project was to explore the instrumental possibilities of using cold neutrons on a pulsed source especially in the area of polarised neutrons. Pulsed sources, due to their very nature provide a large potential for high resolution polarised spectroscopy. The project is an international collaboration with the participation of India, Spain, Sweden, Switzerland and the United Kingdom.

The project has three well-defined phases:

- Phase I is the extraction of a second cold beam guide from the IRIS beam line.

- Phase II is the construction of the large d-spacing powder diffractometer and polarisation of the incident beam.
- Phase III contains; high resolution spectroscopy, spectroscopy polarisation analysis, diffraction polarisation analysis.

Phase I was completed in early 1996 leading to the first diffraction experiment in December 1997. Progression to Phase II will only require the installation of the incident beam polarisers.

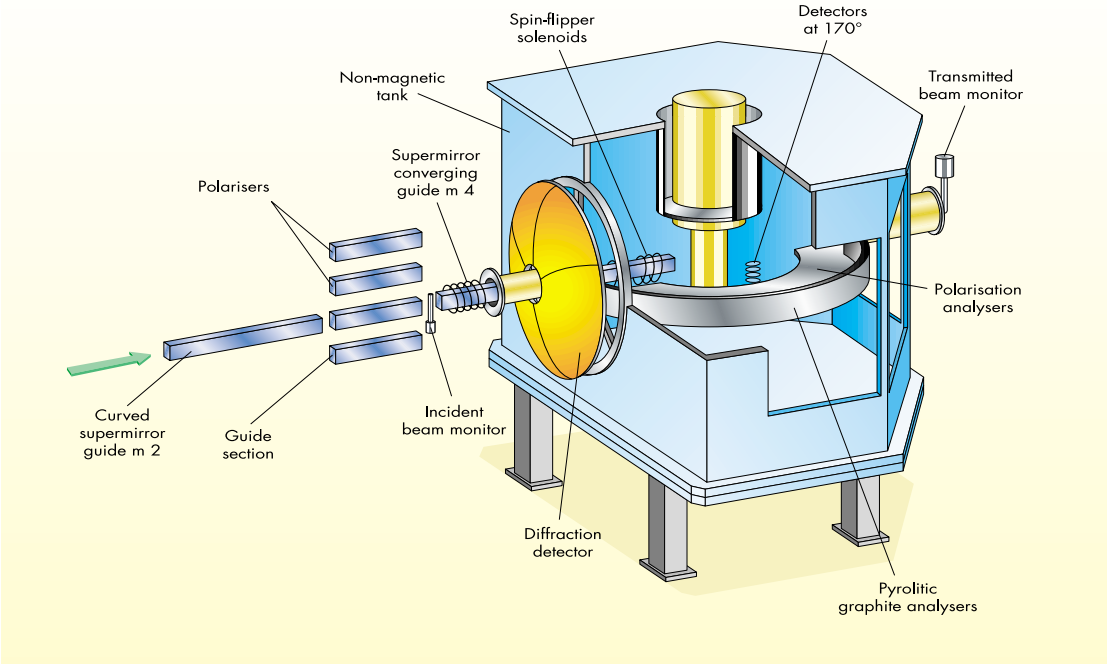

Figure 4.1: A schematic diagram of the OSIRIS spectrometer and diffractometer.

4.3 History of Monte Carlo Technique

The method was developed by Nicholas Metropolis and Stanislaw Ulam during the 1940's at Los Alamos National Laboratory, USA as part of the Manhattan Project to develop the nuclear bomb. The method was used to attempt to

calculate the trajectory of a neutron as it was scattered by nuclei in a nuclear explosion or reactor. This is a task that is very difficult to perform analytically due to the fact that the number of possible paths involved is very large. Typical trajectories were generated and chosen by applying a number of probabilities to given events. At first, this procedure had to be performed by hand, but, with the development of computers, the number of possible uses for the Monte Carlo technique grew tremendously. At present Monte Carlo techniques are still widely used for modelling radiation transport in many systems, which seems to make this technique an obvious choice to simulate neutron transport within various components that join to form a neutron scattering instrument.

4.4 Basic Design Considerations

There are a number of factors that increase the complexity of using analytical calculations for instrument design, for example describing the use of nickel and supermirror guides. Geometric complexities and asymmetries are also difficult to deal with analytically. It makes more sense, in such circumstances to take advantage of the Monte Carlo technique to determine various characteristics of the spectrometer, where it is possible to extract various parameters and distributions at various intermediate parts of the spectrometer that would be otherwise impossible to achieve.

The design of neutron scattering instruments usually involves, at some point, a compromise of some sort. Generally speaking, if we make an instrument with excellent resolution, then we have the penalty of a lower neutron flux, and similarly, if we want a higher flux, then we have to relax the instrumental resolution.

Firstly it was important to determine what purpose the instrument was going to be primarily used for. In the case of OSIRIS, if we take the resolution of IRIS as a starting point, then did we want to improve resolution or go for improved intensity? If we opted for higher resolution then the main design criterion would

have been to move the sample position further away from the moderator than is the case on IRIS. As OSIRIS was to be a polarisation analysis instrument, then we might be expected to maximise flux, especially on the pulsed spallation source such as ISIS, where the flux of 'cold' neutrons is lower than from a reactor source such as the ILL in Grenoble. In this case we should move the OSIRIS sample position towards the moderator rather than further away. This will mean that the resolution of the primary spectrometer will be poorer than IRIS, but the intensity will be higher. The main objective of the guide design was to maximise the intensity for a given value of the resolution. The resolution of the instrument can be split into two parts, that of the primary and secondary spectrometers. If these two components are of similar widths then we may add them in quadrature. If one of the resolutions is much wider than the other, then it is the broader term that will dominate the overall resolution. So, we may argue that if we increase the resolution of a single component to the resolution, hence reducing the intensity, it will have little effect on the overall resolution, but will reduce the total intensity.

4.5 Description of the program

The Monte Carlo program used to investigate the properties of various components of the spectrometer and how they affected the final performance of the instrument, was developed from a program written by M.W. Johnson in 1978. This program mainly dealt with the behaviour of neutron guides. It has now been extended so that various optical elements can be inserted into the incident (or indeed secondary) flight path in addition to providing a method of simulating the entire spectrometer. Various other Monte Carlo ray tracing simulations have been written to aid in the design and optimisation of various components of the spectrometer (e.g. crystal analyser bank).

The basic program requires an input (or geometry) file that describes the positions and properties of the spectrometer's various surfaces and components. The generation of this geometry file is done by an external program. The description of the different surfaces is controlled by various parameters. An

overview of how we define the geometry of a particular surface may be found in the appendix.

The program consists of two distinct simulations; (i) the primary and (ii) secondary spectrometer components.

The simulation of the primary spectrometer is relatively straight forward. For each neutron, a random starting position and direction is selected on the entrance plane of the guide. From this, we extrapolate backwards to ensure that the neutron could have originated at the moderator. Each neutron is then assigned a 'weight' which depends on the neutron intensity at a given wavelength for a particular moderator, which for our case is the 25 K hydrogen moderator at ISIS. The trajectory of the neutron is then followed down the length of the guide; at each collision with a surface, the neutron will undergo total external reflection if it has an incident angle less than the critical angle of that particular surface, θ_c. After each reflection, the 'weight' of the neutron is modified by the reflectivity of the surface. In order to make the simulation as realistic as possible, measured values for the reflectivity have been used. A measurement of the normal supermirror reflectivity is shown in Figure 4.2 and that of the polarising supermirror in Figure 4.3. The output gives a number of useful quantities, the flux and intensity at both the exit of the guide and the sample position, the average number of reflections along the length of the guide, the final beam asymmetry, the flight path uncertainty $(\Delta\ell/\ell)$ and the transmission of the guide. The simulation of the energy resolution function will be described in a later section.

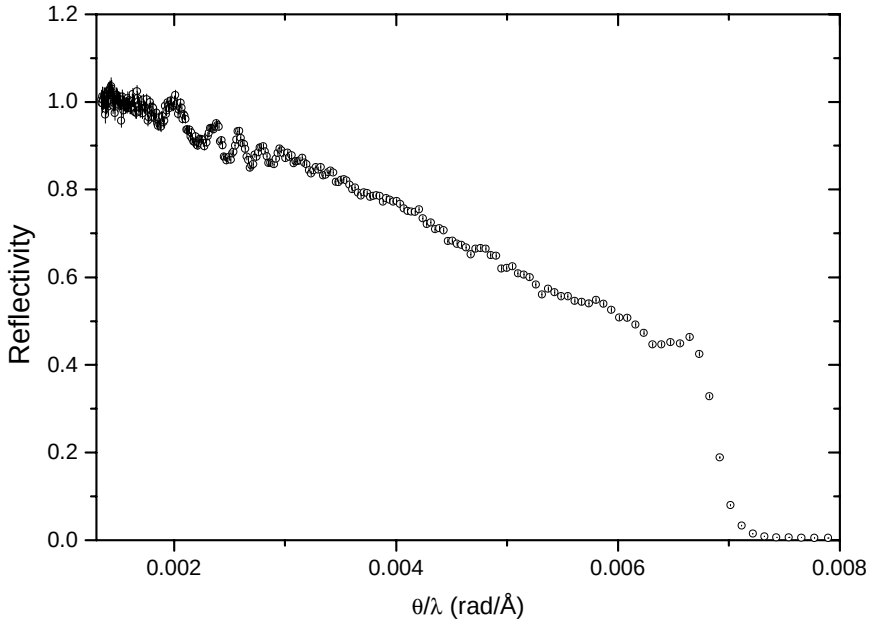

Figure 4.2: Reflectivity curve for a "m" = 4 supermirror (used in simulation).

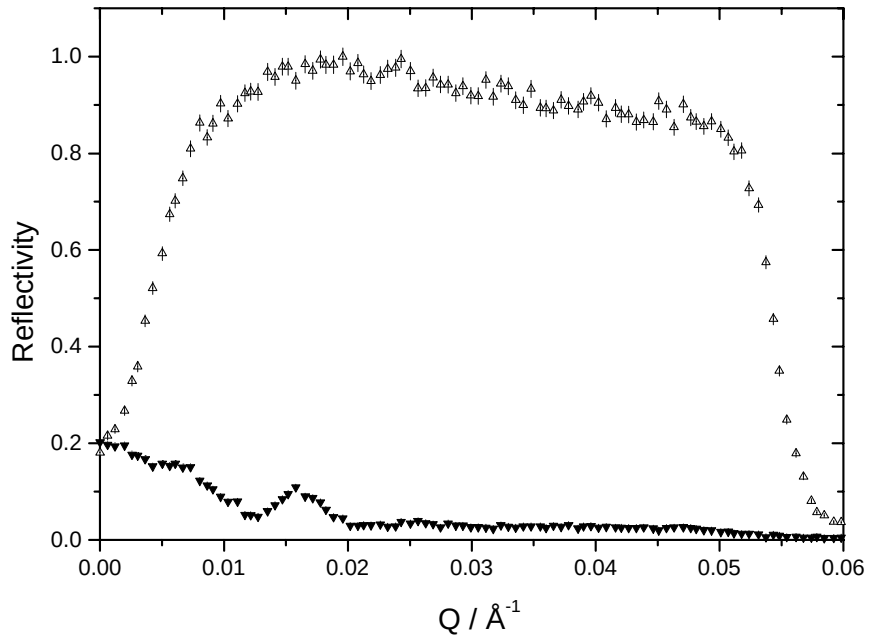

Figure 4.3: Measured reflectivity profile for neutrons of up (Δ) *and down* (τ) *spin states for a "m" = 2 polarising Co/Ti supermirror (Hahn, 1997b).*

4.5.1 Effect of Gravity

One important effect that was not included in the original program was that of gravity. The distance that a neutron, initially travelling horizontally, with a given wavelength, λ, falls as it travels over a flight distance, L, is given by the expression.

$$f(\lambda, L) = \frac{g}{2}\left(\frac{mL\lambda}{h}\right)^2 \qquad (4.1)$$

A plot of the distance that a neutron will fall as a function of the flight distance for a range of different wavelengths is shown in Figure 4.4. We can see that gravitational effects become increasingly more important at longer wavelengths.

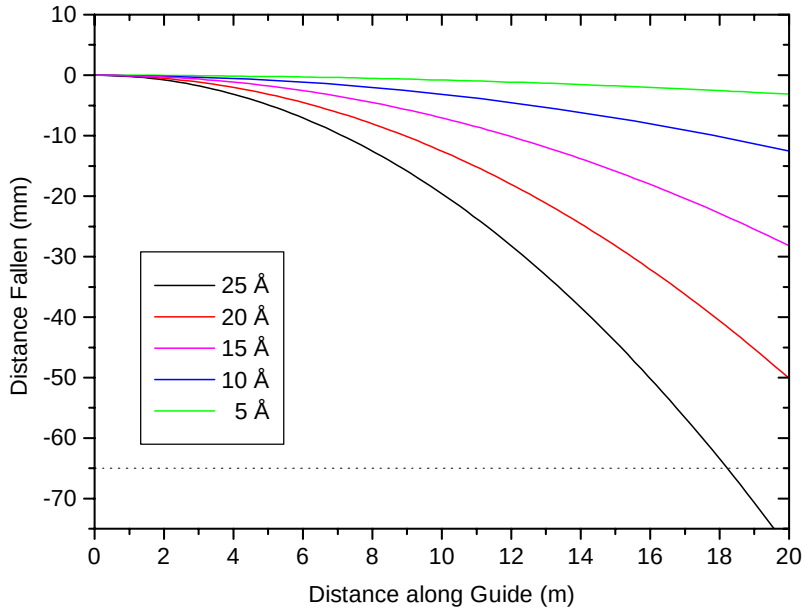

Figure 4.4: The distance a neutron falls as a function of the flight distance for a range of neutron wavelengths. The dotted line indicates the distance a neutron would have to fall to reach the bottom of the OSIRIS guide, assuming that it had entered the guide at the very top and only has a horizontal velocity component.

4.5.2 Moderator energy structure

The energy structure of the neutron pulse (Figure 4.5) was measured for the ISIS liquid hydrogen moderator using the CRISP reflectometer, (Martín, 1996).

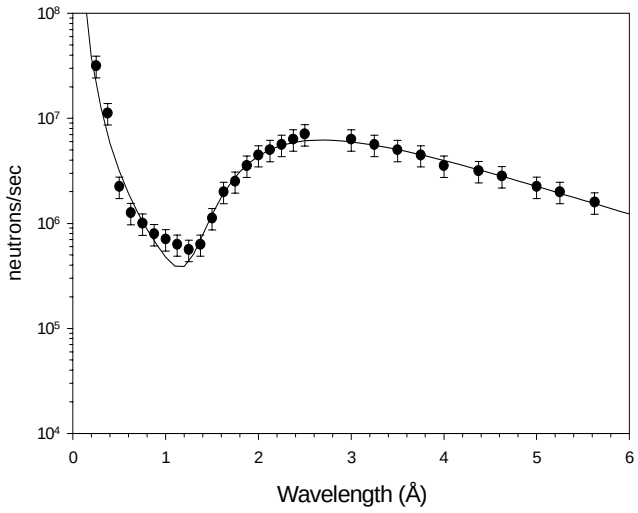

Figure 4.5:The experimental and fitted moderator shapes as measured on CRISP (Martín, 1996)

4.5.3 Model used for moderator time distribution

The distribution used for the moderator time uncertainty (Figure 4.6) is based upon a measured spectrum obtained on the VESTA neutron storage instrument at ISIS (Carlile, 1996).

The time-of-flight shape has been expressed by Ikeda-Carpenter (1985) as

$$P(t) = \frac{t^2}{2\tau_f^3}\exp\left(\frac{-t}{\tau_f}\right) * \left\{(1-R)\delta(t) + R\tau_s^{-1}\exp\left(\frac{-t}{\tau_f}\right)\right\} * \frac{1}{\sigma\sqrt{2\pi}}\exp\left(\frac{-t^2}{2\sigma^2}\right)$$

where t is the time of flight, τ_f and τ_s are time constants, R is switch function and σ is a Gaussian width parameter.

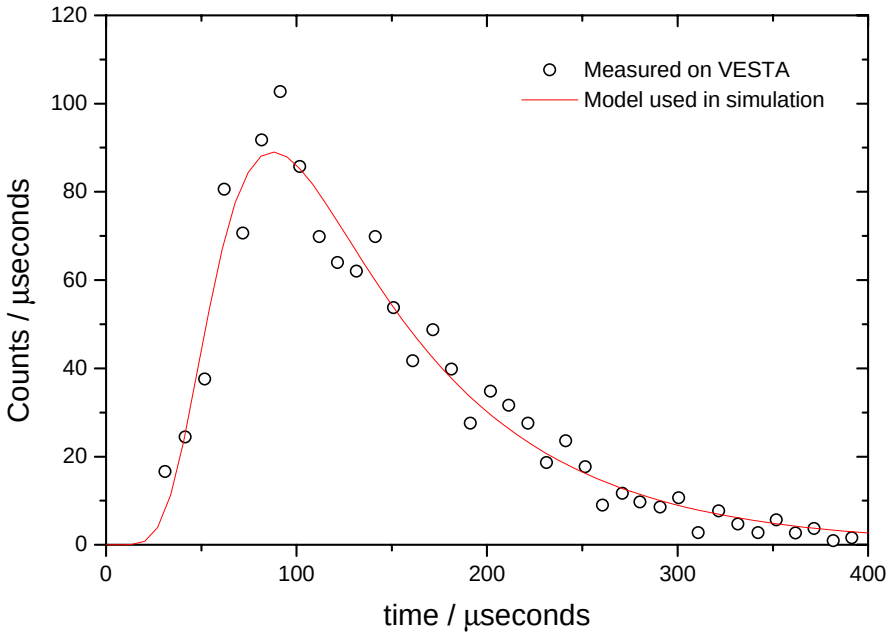

Figure 4.6: Time structure of the neutron pulse emanating from the 25 K ISIS moderator for a wavelength of 6.28 Å. The data points are measured values from VESTA (Carlile, 1996) and the solid line is the model used in the Monte Carlo simulations (equation 4.2).

The first two terms represent the physics of the moderator with the 3rd term being a simple Gaussian representing the instrumental resolution describing the beam divergence, sample size and other effects.

The short time constant, τ_f, is used to describe the contribution of the epithermal or 'slowing down' neutrons in the pulse as it arrives at the sample. The long time constant, on the other hand, describes the contribution from the Maxwellian flux. In between these regimes the factor, R is used to describe how the two contributions change as a function of time.

In order to reduce the time taken by the algorithm, a simplified model has been used (see Figure 4.6). The distribution used is of the form;

$$f(x) = y_0 + A\left(1-\exp\left(-\frac{x-x_0}{\tau_1}\right)\right)^P \exp\left(-\frac{x-x_0}{\tau_2}\right) \qquad (4.2)$$

from which we obtain a number of parameters y_0, A, x_0, τ_1 and τ_2. A random emission time is generated by use of a subroutine employing the rejection method.

4.6 Results of Guide Simulations

In this section, in the interest of brevity, only a few of the many simulations performed to investigate various properties of neutron guide systems will be presented, a more detailed account my be found in Campbell, 1998. It has been fortunate for this study that a similar neutron spectrometer, IRIS, also has a neutron guide as part of its primary spectrometer. The IRIS spectrometer has a nickel (m = 1) coated neutron guide, with a length of 36.54 metres. In order to prohibit fast neutrons hitting the sample, the guide is slightly curved past its line of direct sight. The curvature for the IRIS guide is 1.97 km. In order to ensure that the simulation was providing the correct results, a simulation of the IRIS neutron guide was performed and then compared with experimental data points (see Figure 4.7 - blue curve). The simulation is in general agreement with the measured values (Krishna, 1992). The main discrepancy being the extra intensity in the simulated peak, this is due to Bragg scattering from the aluminium windows, which is an effect that has not been included in the present simulations. A simulation of OSIRIS and the corresponding experimental data can be seen in Figure 4.7 (red curve). The parameters used for the IRIS and OSIRIS guides can be seen in Table 4.1 and Table 4.2 respectively.

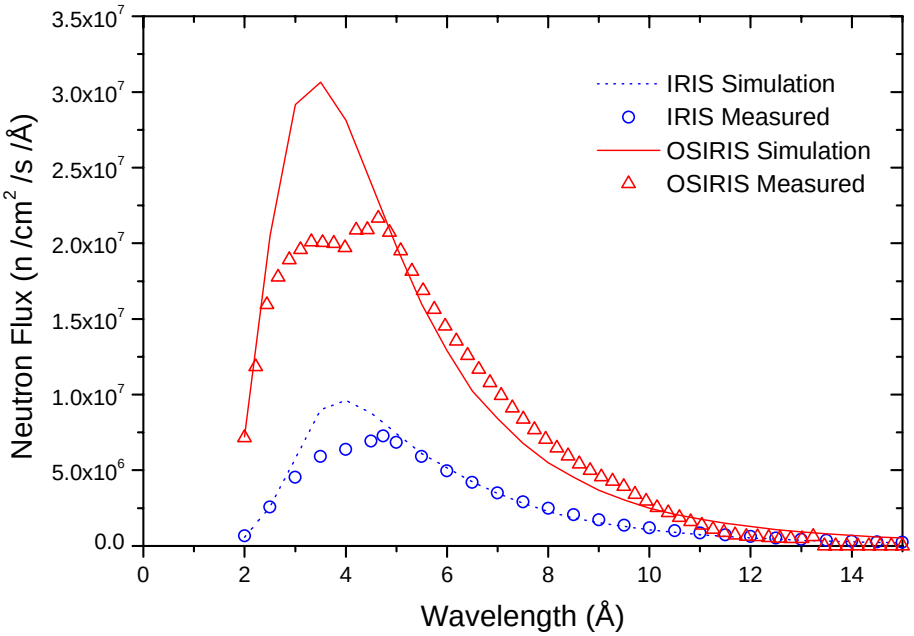

Figure 4.7: Comparison between measured intensity and Monte Carlo simulations for the IRIS spectrometer.

Table 4.1 : Detailed OSIRIS guide parameters.

Length (cm)	*Width (cm)*	*Height (cm)*	*Radius of Curvature (km)*	γ_c/λ *(rad/Å)*
150.0	4.5	6.7	∞	0.00346
46.8	4.5	6.7	∞	0.00346
7.85	4.5	6.7	∞	Gap
200.0	4.3	6.5	∞	0.00346
43.0	4.3	6.5	∞	0.00346
11.75	4.3	6.5	∞	Chopper
300.0	4.3	6.5	2.05	0.00346
68.2	4.3	6.5	2.05	0.00346
7.56	4.3	6.5	2.05	Chopper
2100.0	4.3	6.5	2.05	0.00346
64.39	4.3	6.5	2.05	0.00346
1.15	4.3	6.5	∞	Gap
50.0	4.3	6.5	∞	0.00346
3.0	4.3	6.5	∞	Monitor
150.0	4.3 → 2.2	6.5 → 4.4	∞	0.00692

Table 4.2: Detailed IRIS guide parameters.

Length (cm)	Width (cm)	Height (cm)	Radius of Curvature (km)	γ_c/λ (rad/Å)
196.8	4.5	6.7	∞	Steel
6.7	4.5	6.7	∞	Gap
46.8	4.3	6.5	∞	0.00173
36.7	4.3	6.5	∞	Gap
162.8	4.3	6.5	∞	0.00173
19.8	4.3	6.5	2.35	Chopper
300.0	4.3	6.5	2.35	0.00173
40.0	4.3	6.5	2.35	0.00173
19.1	4.3	6.5	2.35	Chopper
60.0	4.3	6.5	2.35	0.00173
2000.0	4.3	6.5	2.35	0.00173
300.0	4.3	6.5	∞	0.00173
250.0	4.3 ➔ 2.1	6.5 ➔3.2	∞	0.00346

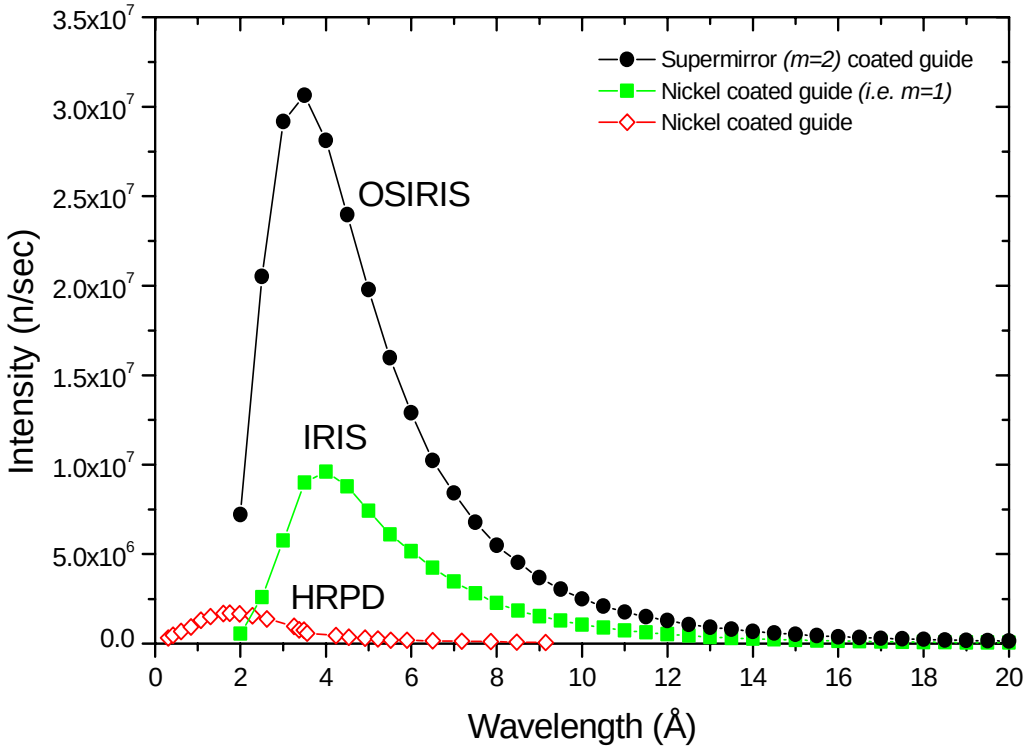

Figure 4.8: The neutron intensity of HRPD, IRIS and OSIRIS as a function of wavelength. The HRPD results are measured intensities. IRIS and OSIRIS results are Monte Carlo simulations.

4.6.1 Effect of altering the converging guide coating.

Originally, at the time of the design of the guide, it was envisaged that a supermirror with a critical angle of m = 4 would be available to use for the final double converging section. At the time of the construction of the guide, such a coating was unavailable. This was due to the high levels of stress within the supermirror film, which resulted in it flaking off the glass substrate after a relatively short period of time. A series of Monte Carlo simulations were performed in order to investigate the effect of reducing the "m"-value of its coating on the final intensity at the sample position (Figure 4.9). The guide geometry was fixed for the case of the OSIRIS guide (see Table 4.1).

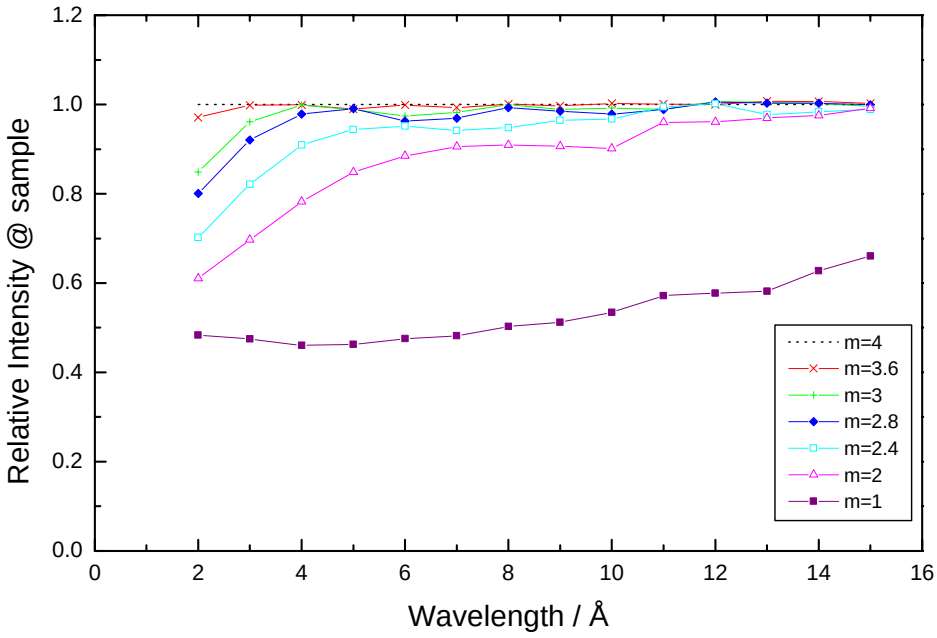

Figure 4.9: Intensities for different converging guide coatings relative to the intensity observed with a m = 4 supermirror.

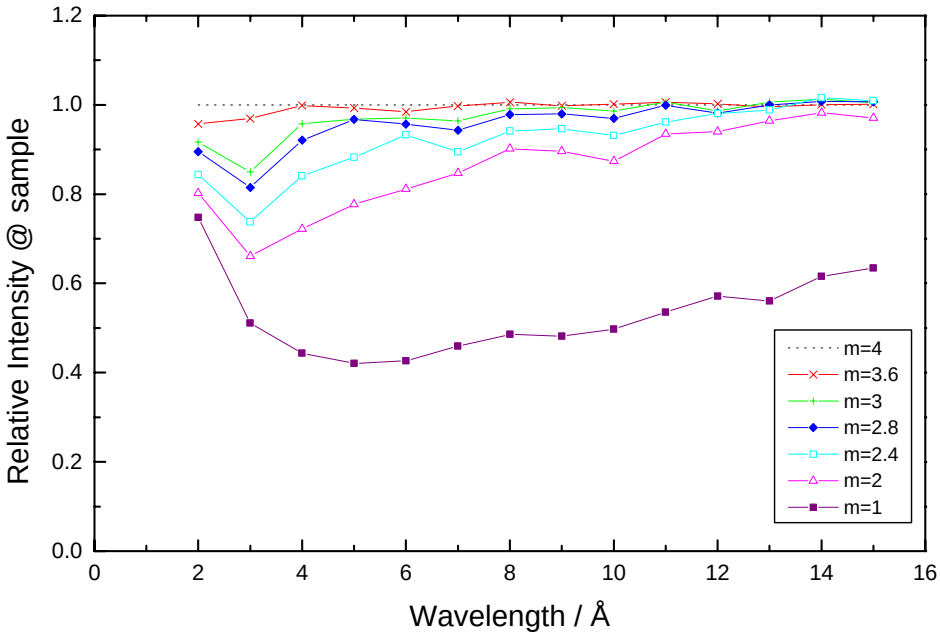

Figure 4.10: Relative intensities for different converging guide coatings to the intensity observed with a m = 4 supermirror. A bender is also present in the incident beam.

The wavelength range used for was $2 < \lambda < 15$ Å. Simulations were also done with the same OSIRIS guide, but with a bender (λ^*=2.317 Å) inserted in the incident beam directly before the converging guide section (Figure 4.10). From these simulations it can be seen that a value of m = 3.6 results in very little loss in intensity over the entire wavelength range.

4.6.2 The Impact of the "m"-value with guide length

A number of simulations were performed to observe the effect of increasing the critical angle has as a function of neutron guide length . The simulations were performed for a straight guide of varying length ($5 < L < 120$ m) over a neutron wavelength range of $2 < \lambda < 20$ Å for m = 1, 2, 3 and 4 supermirror coatings. The results are displayed as a ratio of the intensity (at the guide exit) to that for the m = 1 case, and can be seen in Figure 4.11.

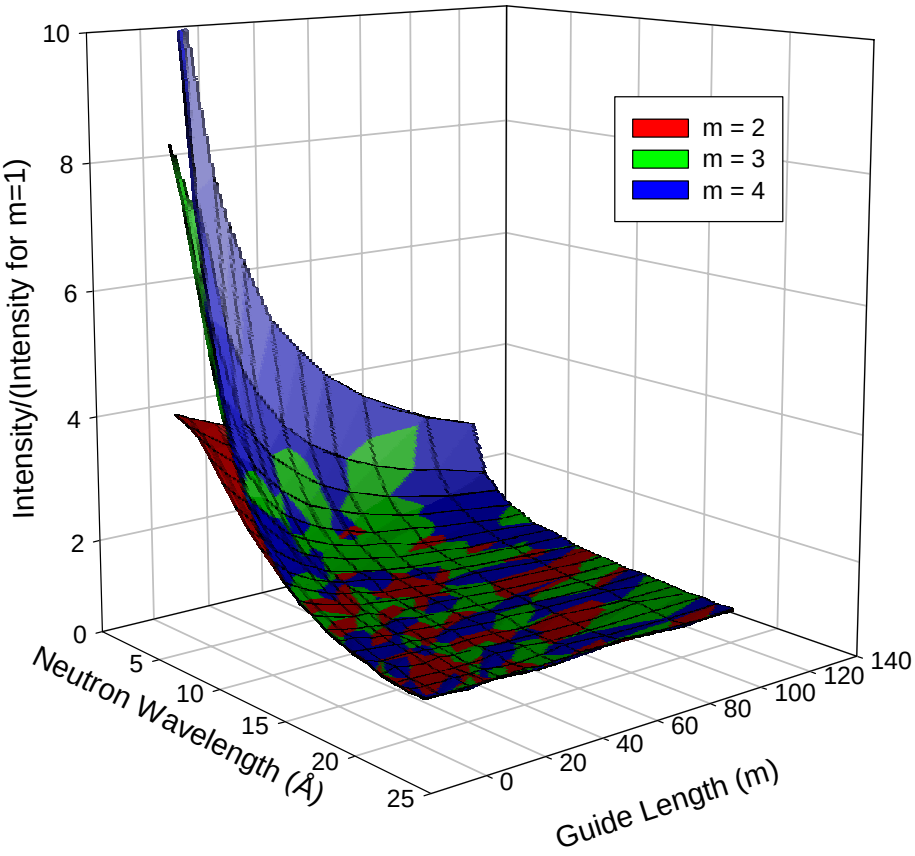

Figure 4.11: Ratio of the increase in intensity for different guide coatings over that m = 1 case as a function of the neutron wavelength and the length of the guide.

It can be seen that as we increase the length of the neutron guide, the benefits of using a supermirror with a higher "m"-value are reduced, especially for longer wavelengths (see Figure 4.12). As the cost of producing supermirrors with a m=4 coating is quite high, there must be a careful assessment of whether an acceptable result could be obtained by using a coating with a smaller m-value and thus lower cost.

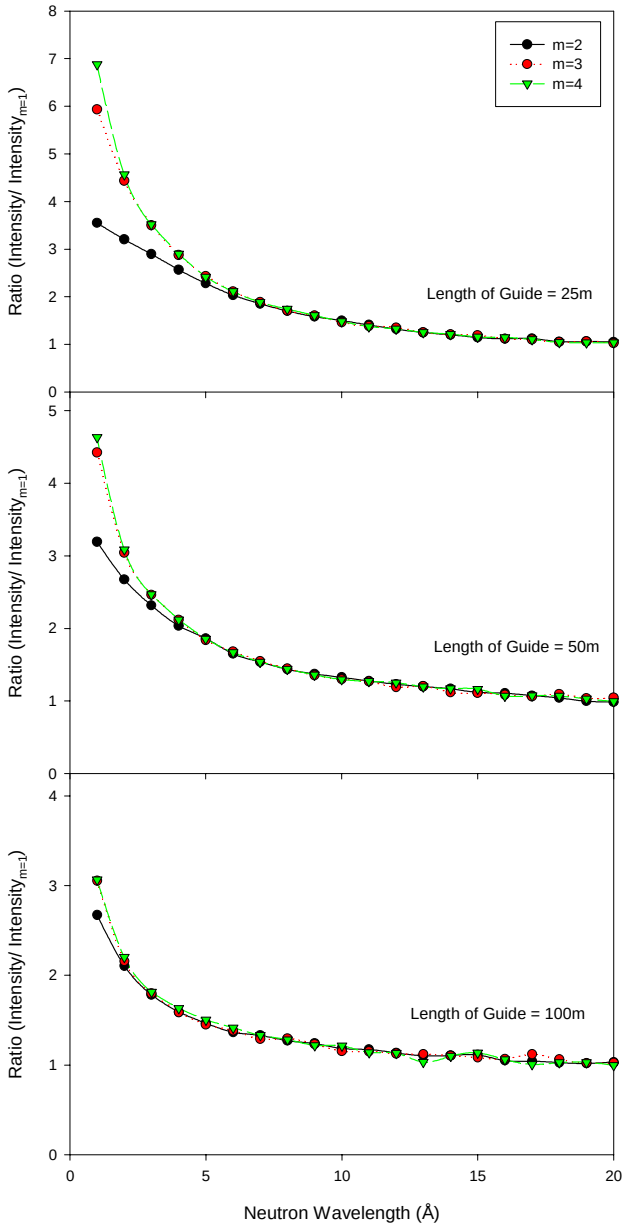

Figure 4.12: A cut through the surface shown in Figure 4.11 for discrete values of the guide length

4.6.3 Improvements to the IRIS guide.

When IRIS was first constructed there were many areas of the guide that were not complete. This was for a number of reasons, one being that originally a Fermi chopper was going to be included into the guide. With the construction of OSIRIS, it has been possible to fill in these gaps. A Ni/Ti supermirror (m = 2)

deposited onto float glass has been used to bridge these discontinuities in the IRIS guide. Simulations have been performed to predict the effect of adding these new sections. Results of these simulations can be seen in Figure 4.13.

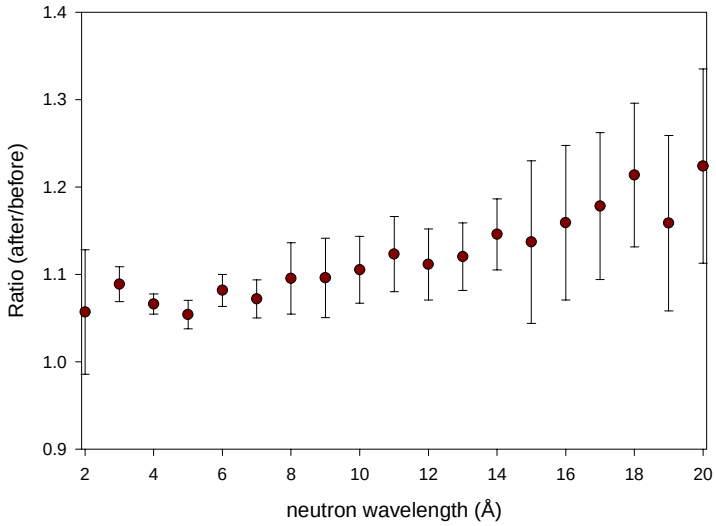

Figure 4.13: The simulated increase in flux of IRIS as a result of closing missing sections of the guide (installed during the OSIRIS construction).

Another obvious avenue for upgrading the IRIS guide is to replace the existing nickel coated guide with a supermirror coated one. It might be said that, if we increase the critical angle of the guide then we will have a wider range of possible trajectories for each neutron and hence the uncertainty in the incident flight path length will increase. In practice, however, this effect has been found to be negligible.

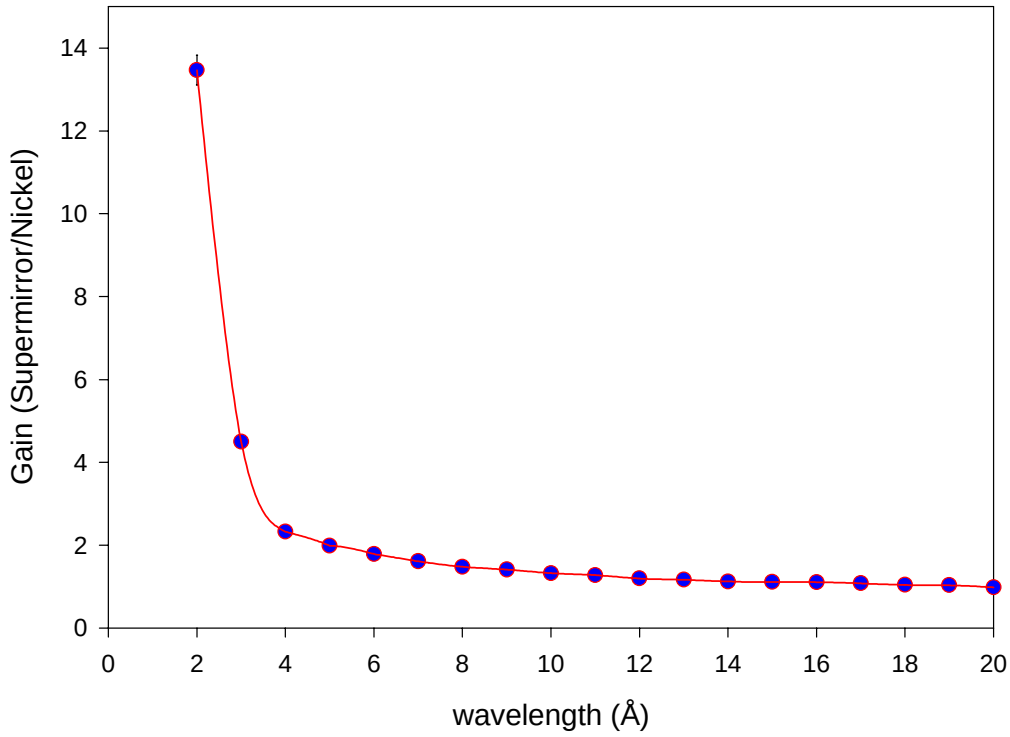

Figure 4.14: The intensity gain factor for the IRIS guide if we replace the existing nickel guide with a supermirror coated one.

4.6.4 Effect of missing section in shutter guide.

During the installation of the OSIRIS/IRIS shutter it was found that there was a section of glass missing on one side of the OSIRIS beamline. It was important to evaluate what the effect of this missing piece would be, so that a decision could be made on how to proceed. The gap was length 47.5 cm long, but it was possible to show that by inserting a 20 cm supermirror coated glass section (so as to reduce the gap to 27.5 cm) the reduction in intensity could be minimised (Figure 4.15).

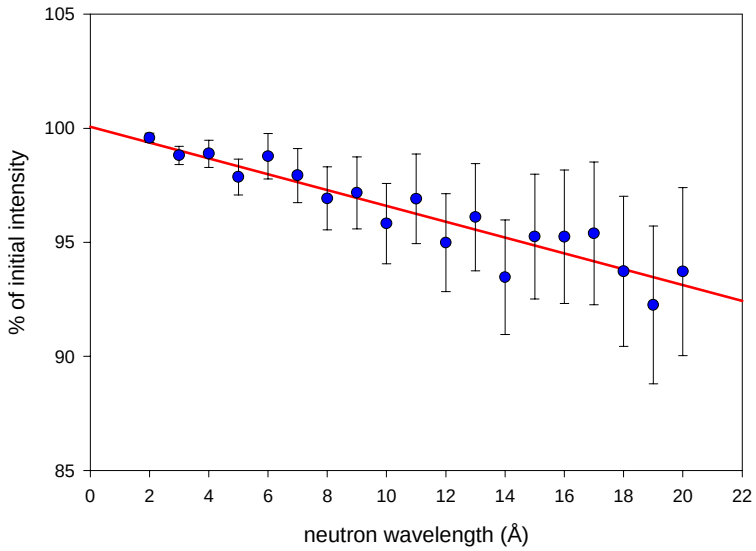

Figure 4.15: The reduction in intensity as a result of having a gap on one side of the OSIRIS shutter guide section. The red solid line is a linear fit to the data which has a gradient of -0.347 ± 0.033.

4.6.5 Symmetry of transmitted beam

When a curved section of neutron guide is used, an additional straight section is placed directly after it to reduce the beam asymmetry at the guide exit (Carlile *et al.*, 1979). The origin of this asymmetry lies in the garland reflections that are found around the edge of the guide. This garland effect will only occur if we either have a coating with a small critical angle or at short wavelengths ($\lambda \leq \lambda_c$). Otherwise we will get a mixed of garland and zigzag reflections ($\lambda > \lambda_c$). The critical wavelength, λ_c, is given by the expression

$$\lambda_c = \frac{1}{\gamma_c}\sqrt{\frac{2a}{\rho}} \qquad (4.3)$$

where a is the width of the guide, and ρ is the radius of curvature. We have shown that if a supermirror coating (m = 2) is used, then the beam asymmetry at the end of a curved guide is comparable to that at the end of a nickel guide (m = 1) consisting of curved and straight sections. This is due to the increased critical

angle per unit wavelength (γ_c), which results in a reduced λ_c, therefore giving a smaller region where only garland reflections occur. We can see in Figure 4.16 that, by using a guide with an m = 2 supermirror coating, we get a more constant beam symmetry over the whole wavelength range than the m = 1 nickel guide (curved & straight).

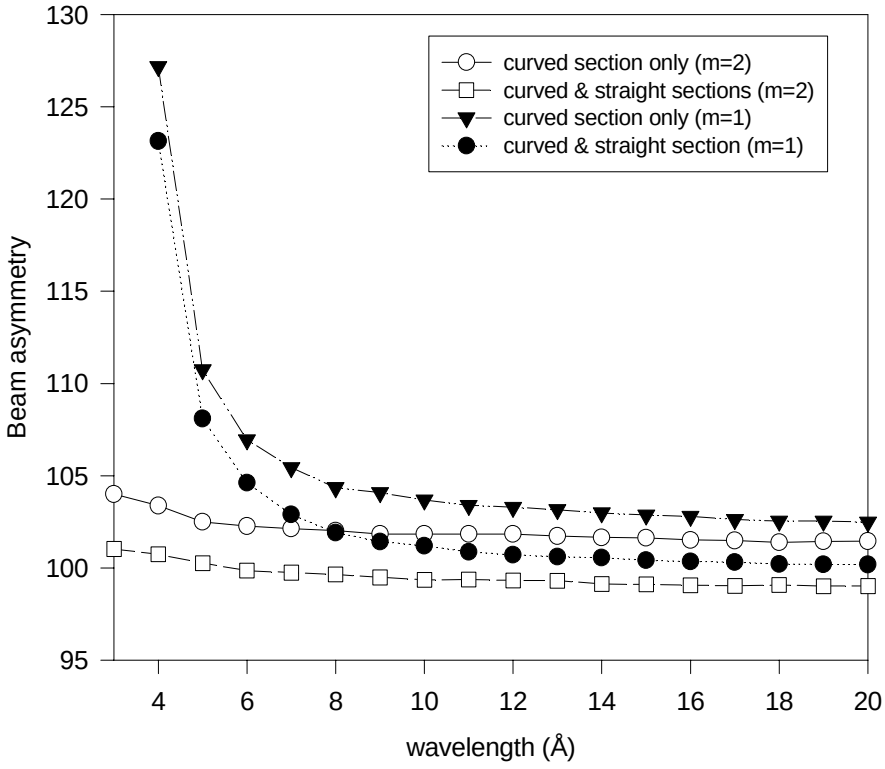

Figure 4.16: Beam asymmetry at the guide exit as a function of different surface coatings and guide geometries. The asymmetry ratio is defined as the number of neutrons that exit on the concave side of the guide divided by those which exit on the convex

4.6.6 Transmission

A comparison of Monte Carlo simulations of the transmission (see *Figure 4.17*) of a curved guide using a constant reflectivity up to the critical angle shows almost identical results to theoretical calculations by Dubbers (1994). If the reflectivity used in the theory is the average measured reflectivity over the simulated range, there is also close agreement between simulation and

theory for a nickel guide (m = 1). Although, for a supermirror (m = 2) the curves clearly disagree. This is mainly due to the fact that at long wavelengths, the reflectivity will be higher than the average value used, and vice-versa at short wavelengths. If we now perform the simulations again, but this time using a constant reflectivity profile instead of a measured one. The comparison with analytical calculations can be seen in Figure 4.18, from this it can be seen that there is excellent agreement between the curves. The analytical calculations looked at here required that the guide be fully illuminated at all wavelengths, so in order to be able to compare directly, all the simulations have been performed using a moderator with infinite height (and width).

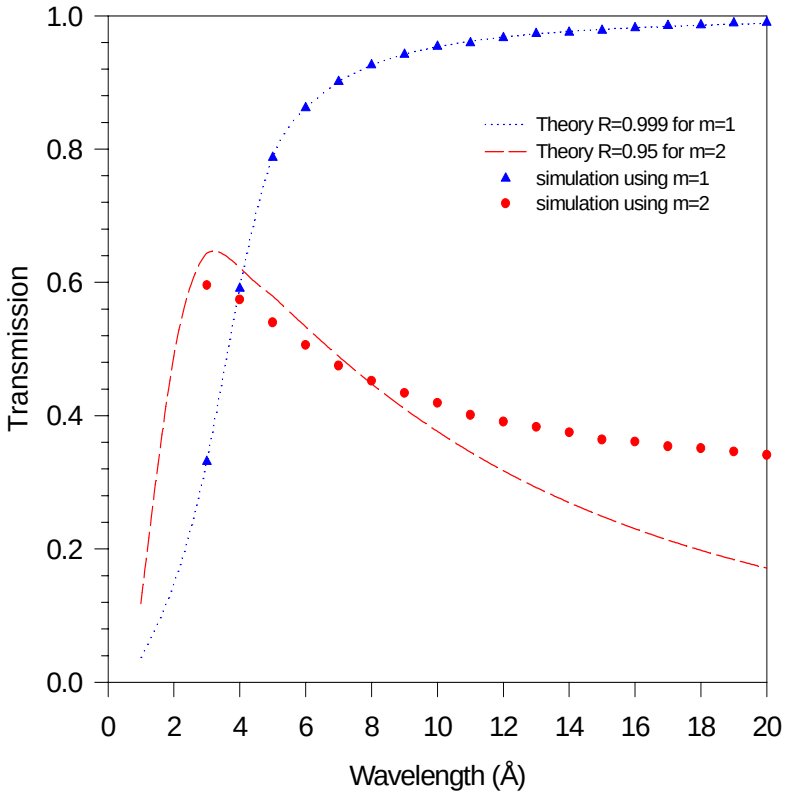

Figure 4.17: Comparison of theoretical and simulated transmission for curved supermirror guides with nickel (m = 1) and supermirror (m = 2) coatings.

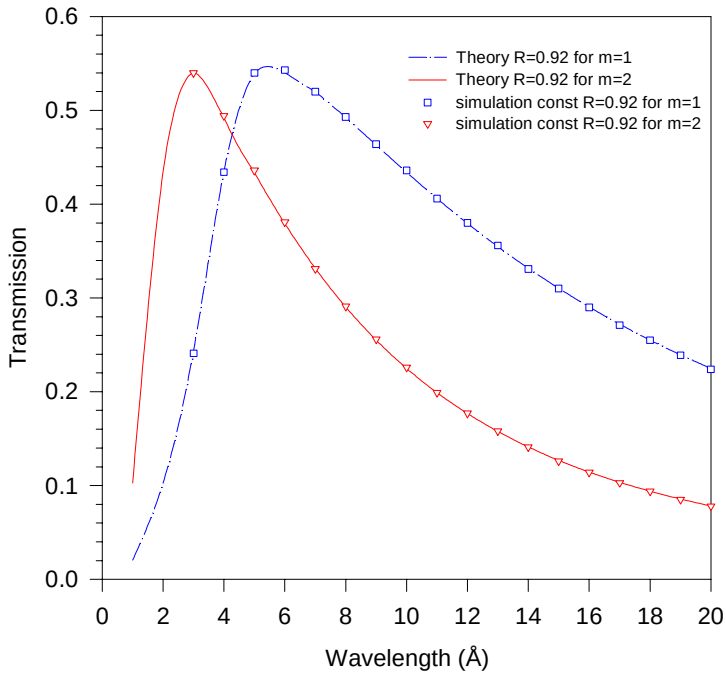

Figure 4.18: Theoretical and simulated transmission for a lossy curved guide. The reflectivity of the surfaces was fixed at R=0.92 for all cases.

4.7 Optimisation of Polarising Supermirror Benders.

A polarising bender is a curved multi-channel Soller type device, consisting of supermirrors that preferentially reflect one spin state. The bender itself was included as a "special" neutron guide section, so that its effect on the performance of the guide as a whole could be observed. The main parameters that needed to be optimised were the radius of curvature and the number of channels in the bender, as the length of bender section had already been fixed by the guide geometry. A number of simulations on different bender geometries have been performed in order to determine the optimum configuration for an actual guide geometry. As the number of internal glass substrates (typical thickness = 0.2 mm) is increased, the transmission increases. This is because the channel width, *a*, is decreasing, therefore the curvature required[1] to bend past the

[1] Here we assume that the curvature is adjusted to match the spacing, *a*, as implied by equation 3.1.

line of direct sight is less. As we decrease the curvature, the incident angle is smaller, so a larger number of neutrons are reflected. At the point ($\lambda > \lambda_c$), (see equation (4.3)), there is an increase in the number of reflections, and, because we have a reflectivity, R < 1, there is a reduction in the transmitted intensity (see Figure *4.17*). Due to the time and cost involved in the production of benders of this type, a compromise had to be reached. By looking at Figure 4.19 we can see that a bender with ~35 glass spacers would give a good transmission for all wavelengths. The transmission of this bender as a function of neutron wavelength is shown in Figure 4.20.

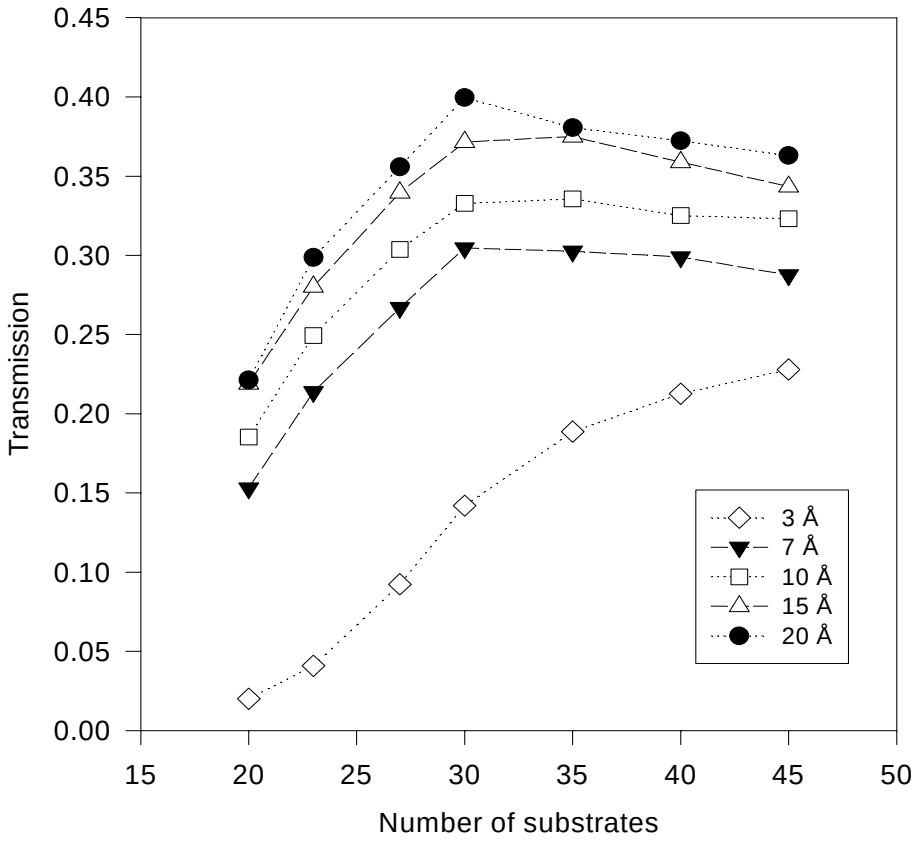

Figure 4.19: Transmission of polarising supermirror benders (m = 2) as a function of number of internal glass substrates and wavelength. Beam area = 4.3 ×6.5 cm.

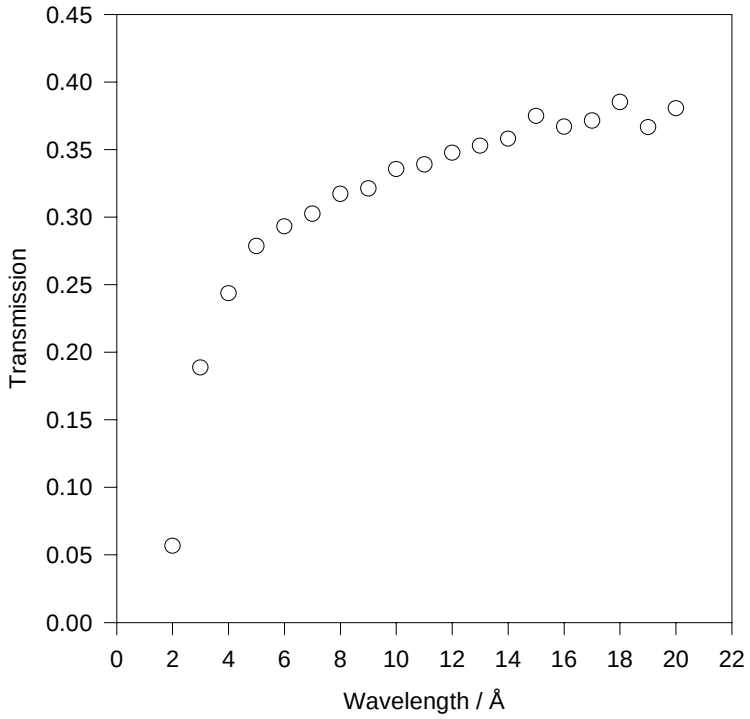

Figure 4.20: Transmission curve for a 35 substrate bender with a characteristic wavelength, λ=2.317 Å, which has a length of 50 cm and radius 3112.513 cm.*

4.8 Microguide Testing device, MITED

To ensure the high reflectivity of the guide sections, a microguide testing device (MITED) was installed as a parasitic instrument on the IRIS beamline with the capability of being able to operate simultaneously and independently of IRIS.

4.8.1 The microguide technique

Neutron reflectivity provides us with a direct means of characterising multilayer devices such as supermirrors. It is difficult to measure with good accuracy the reflectivity using the classical one reflection technique. This is because the differences between the incident and reflected beams are small. It has been previously shown (Ballot *et al*; 1993 & 1994) that by employing a method of multireflectivity, it is possible to increase the precision on the deviation from 1 of the reflectivity by a factor up to twelve.

For the case of a single reflection, the reflected intensity I is proportional to the intensity of the incident beam I_0 for a given value of the momentum transfer Q.

$$\mathrm{I}(\mathrm{Q}) = \mathrm{R}(\mathrm{Q})\mathrm{I}_0(\mathrm{Q}) \tag{4.4}$$

where the constant of proportionality is the reflectivity value for the mirror and where

$$\mathrm{Q} = \frac{4\pi}{\lambda}\sin\theta \tag{4.5}$$

In the case of a multireflectivity experiment, we measure the intensity after N reflections

$$I(Q) = R^N I_0(Q) \tag{4.6}$$

We can now express the measured multireflectivity R' for an integer number of reflections as a function of the single reflectivity R

$$R' = R^N \tag{4.7}$$

When the value of N is not an integer, which means that part of the beam is reflected N times and part reflected N+1 time, the measured reflectivity is

$$R' = (1-x)R^N + xR^{N+1} \tag{4.8}$$

where N and x are functions of the length of the mirrors L, the incident angle θ, and the width between the two mirrors e.

$$L = (N+x)\frac{e}{\tan\theta} \tag{4.9}$$

We do not consider either the beam divergence or the surface roughness in the calculation of equation (4.8). This expression does not present an analytical solution and has to be solved numerically.

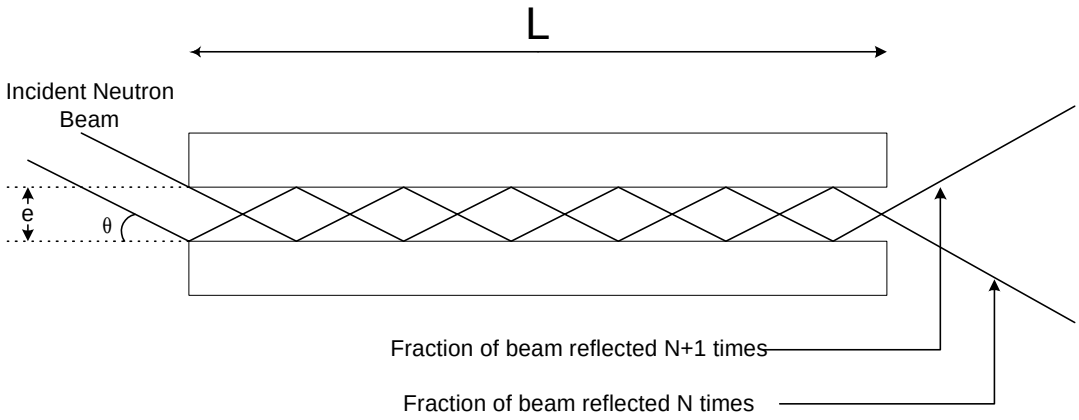

Figure 4.21: Configuration of microguide for a non-integer number of reflections

4.8.2 Experimental Setup and Results

The MITED instrument (Figure 4.22) is situated in the position usually occupied by VESTA. A detailed description of VESTA and its applications can be found in Jericha *et al.*, 1996. A pyrolytic monochromator is inserted into the IRIS beamline (N6) at an angle of 43° giving a beam of monochromatic neutrons with a wavelength $\lambda = 6.27$ Å for the PG002 reflection. The monochromatic beam is collimated by two variable width slits, the beam width is usually set to be the same as the microguide glass separation (typically a value of ~ 1 mm is used). There is a single He^3 detector tube positioned at the end of the microguide, which can either be moved in unison with the glass sections or independently around the end of the microguide.

Due to the fact that we are using a monochromatic beam, we need to make a scan in θ in order to obtain the whole reflectivity profile. The beam intensity is measured as a function of angle, θ. Two identical mirror surfaces are separated by six individual spacers (3 on the top and 3 along the bottom). The glass

sections are held in place by means of three clamps. To obtain a measurement of the incident beam the microguide is placed at an angle of $\theta = 0°$.

A total of six different pairs of mirrors have been measured. They have all been supermirrors (m = 2) of the type $NiN_xO_y/TiV_{0.05}$. Measurements were made at angles in the range $0.0 < \theta < 1.4°$.

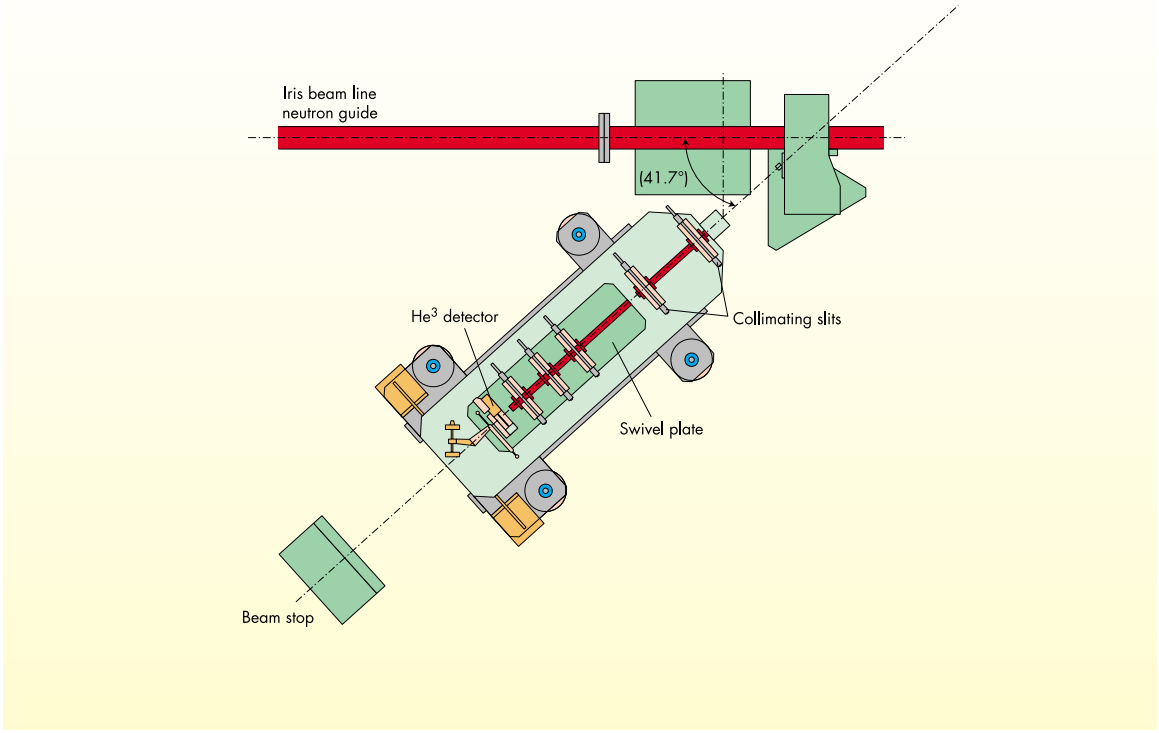

Figure 4.22: Plan View of the MITED instrument.

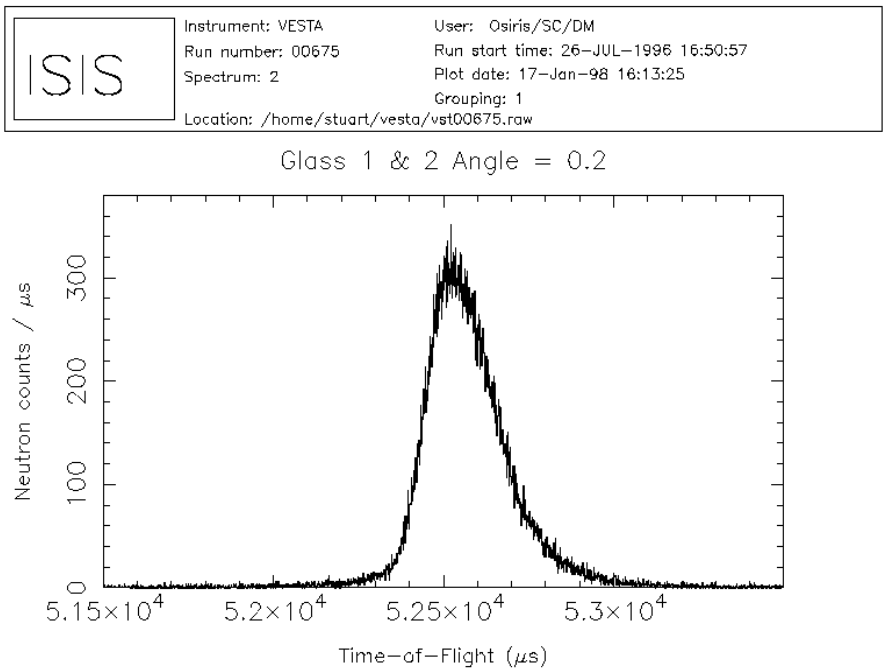

Figure 4.23: Typical spectrum obtained from the MITED instrument.

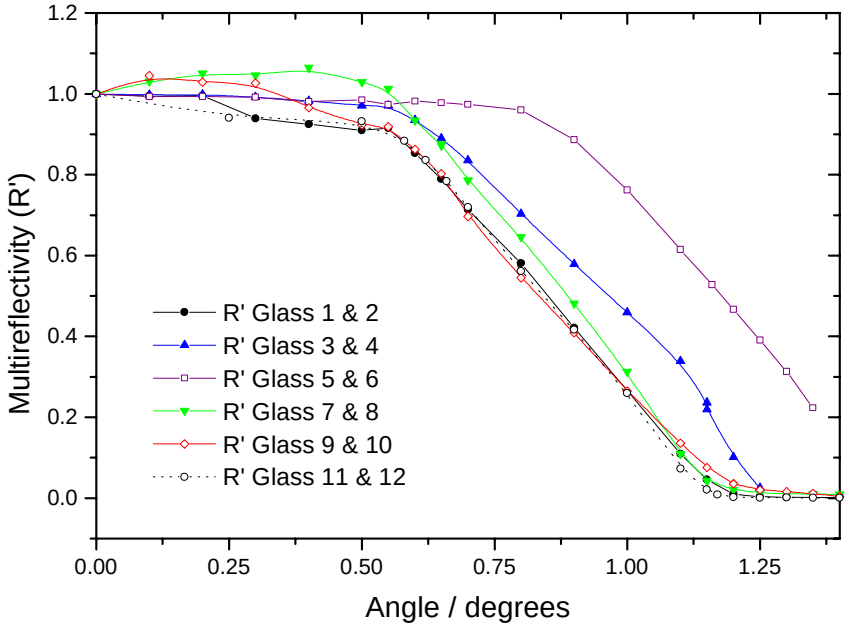

Figure 4.24: The measured multireflectivity of a number of coated guide sections.

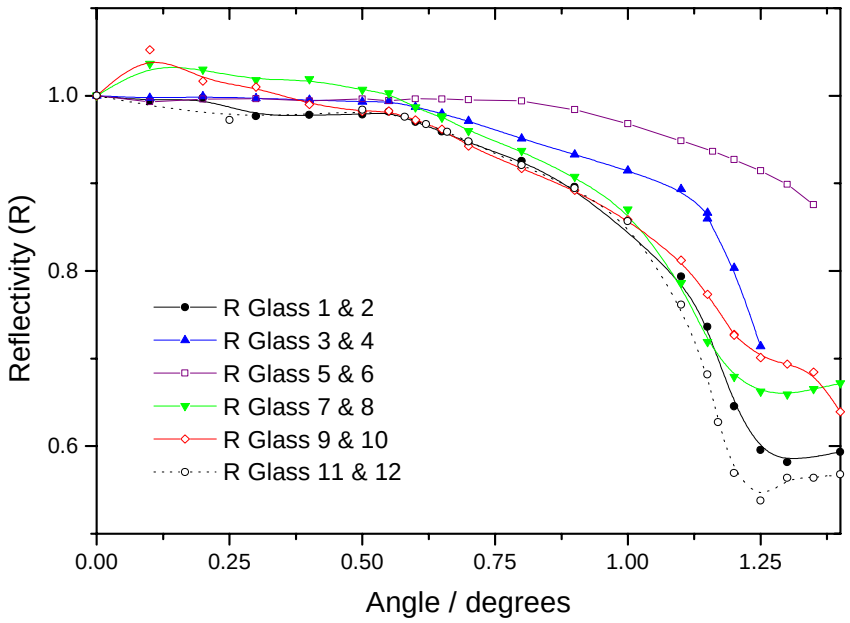

Figure 4.25: The reflectivity values extracted from the data shown in Figure 4.24.

4.9 Reflectivity of coated stainless steel

Classical one reflection measurements have been made for a supermirror deposited onto a polished stainless steel substrate (Martín, 1997). The results can be seen in Figure 4.26. It is clear from this, that the sample has a small critical angle and therefore would be unsuitable for use in the guide.

4.10 Surface Roughness Measurements

Due to the high levels of radiation at positions close to the target, there is a possibility of radiation damage of the glass sections. This is usually dealt with by replacing the glass substrates either by a coated stainless steel substrate or more often, just plain stainless steel. The much lower reflectivity of the steel as opposed to the glass can be understood by realising that steel has a much greater surface roughness than that of float glass.

Atomic force microscopy (AFM) measurements have been carried out for three different supermirror samples, two of which had been deposited onto glass substrates and the other onto a steel substrate. The AFM used is a Nanoscope manufactured by Digital Instruments Inc. For each sample three different scans were performed over different scan sizes, 50 μm, 10 μm and 1 μm. The r.m.s. roughness values obtained are given in Table 4.3. Two different areas were studied for one of the glass samples and the steel sample, this was in order to investigate the uniformity of the films.

The measurements made for the supermirror with a steel substrate, were performed on the most visibly unmarked areas that could be found. We should note that area #2 for the steel sample looked better than area #1, and this is upheld by the r.m.s. roughness values obtained. Cross sections profiles of various scans can be seen in Figure 4.27.

We can see from Table 4.3 that the roughness values obtained for the smallest scan area (1 μm) are similar for all the samples. This becomes decreasingly the case as we increase the scan size. One possibility for this kind of correlation is that that the roughness at longer scan sizes is due to polishing scratches.

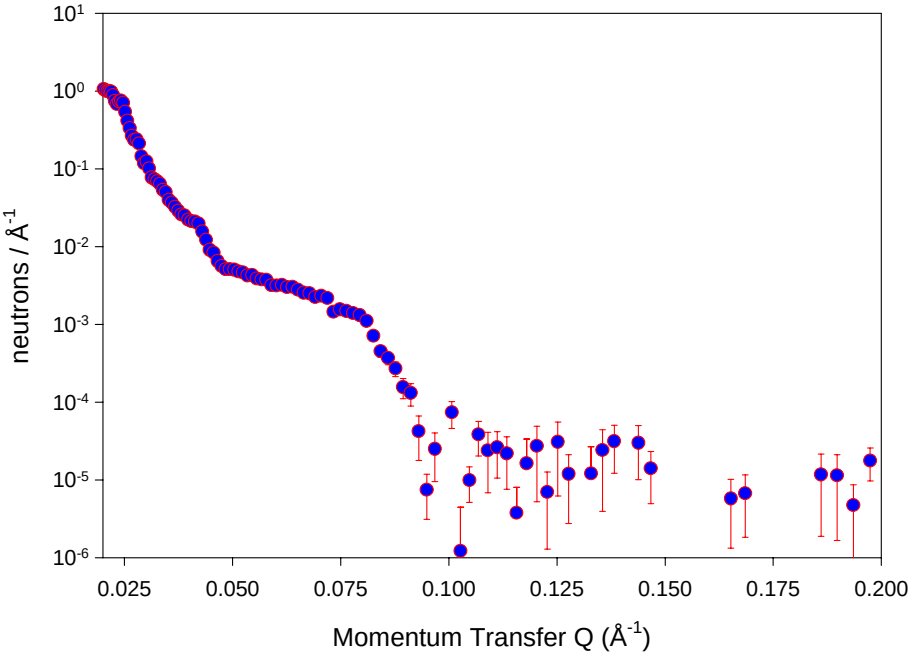

Figure 4.26 : Neutron reflectivity measurement of supermirror deposited onto a steel substrate measured on the CRISP reflectometer at ISIS.

Table 4.3: R.M.S. roughness values obtained for various supermirror samples.

Scan area :	*50 μm*	*10 μm*	*1 μm*
	R_a (nm)	R_a (nm)	R_a (nm)
Glass #1 (area #1)	0.598	0.887	0.974
Glass #1 (area #2)	0.633	0.957	0.912
Glass #2	0.530	0.917	0.817
Steel (area #1)	4.684	2.959	1.678
Steel (area #2)	3.682	2.598	1.197

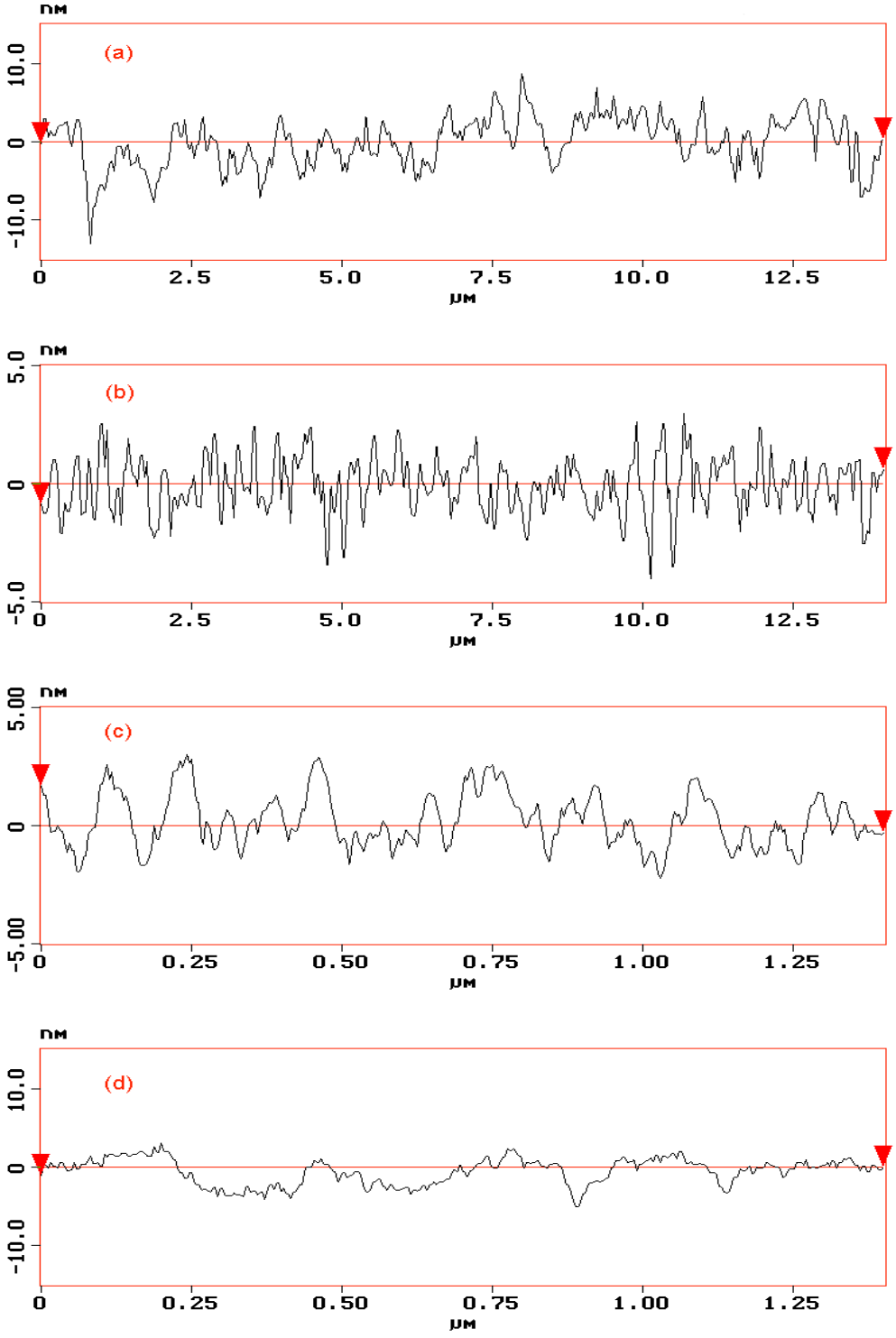

Figure 4.27: AFM roughness profile cross sections (a) Steel 10 µm scan, (b) Glass #1 10 µm scan, (c) Glass #1 1 µm scan, (d) Steel 1 µm scan.

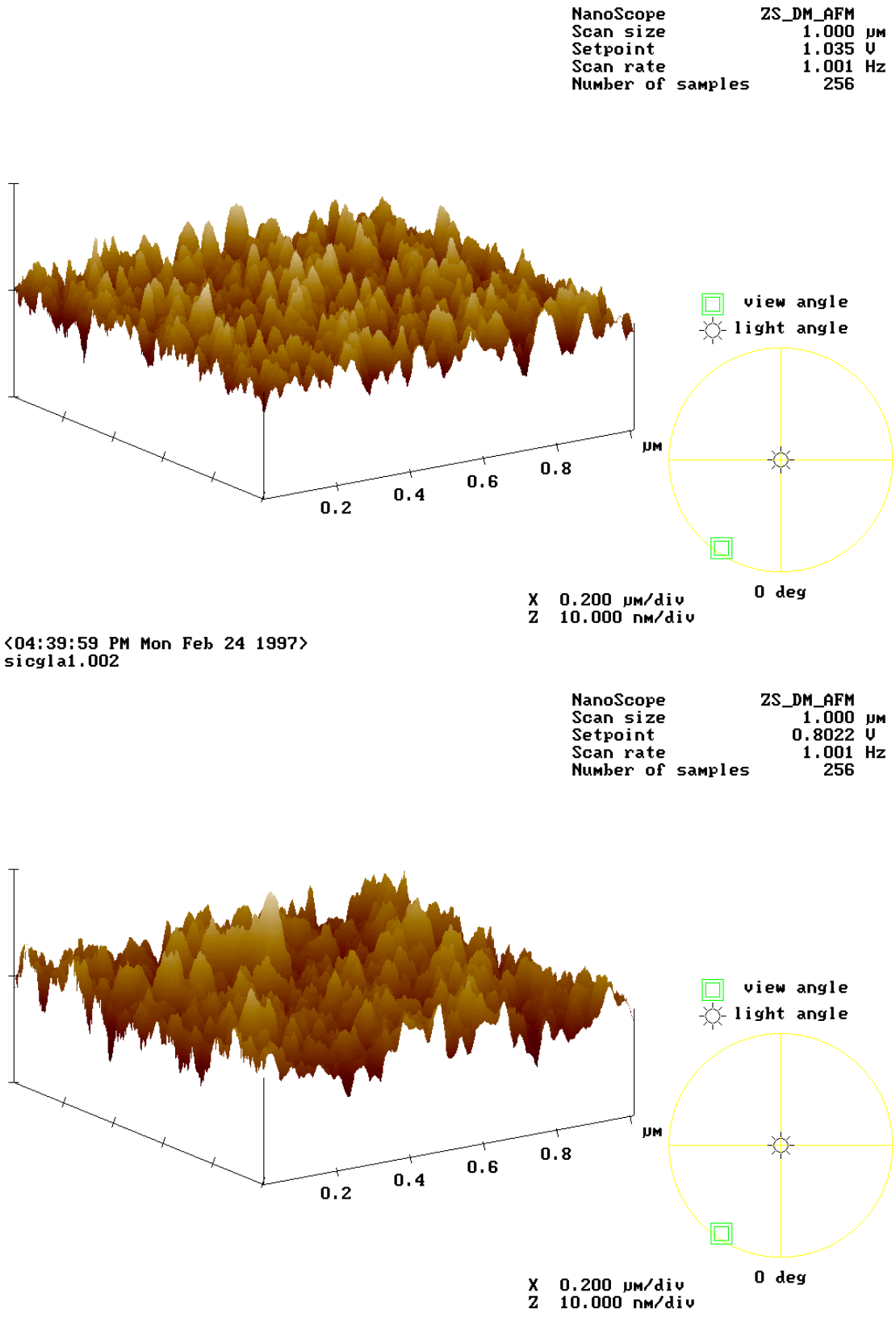

Figure 4.28: A comparison AFM measurements made for a supermirror deposited onto float glass (top) and one deposited onto polished steel (bottom).

4.11 Study of the Resolution function

4.11.1 Why do we need to understand resolution functions?

In a neutron scattering experiment it is impossible to measure the scattering function S(**Q**,ω) directly without it being influenced by the resolution (or response) function of the spectrometer used. The actual quantity that is measured can be expressed as,

$$S^{meas}(\mathbf{Q},\omega) = S(\mathbf{Q},\omega) \otimes R(\mathbf{Q},\omega) \tag{4.10}$$

where R(**Q**,ω) is the resolution function of the spectrometer used and ⊗ represents a convolution. It is therefore extremely important to have a detailed understanding of what different factors contribute to the final resolution function. It is standard practice to measure the resolution of a given spectrometer[2] using an incoherent scattering sample (e.g. vanadium), but from this we are not be able to extract any information about which effects are dominant.

4.12 Energy Resolution

For the case of an inverted geometry spectrometer with analyser crystals in near backscattering geometry the energy resolution is given by the expresssion;

$$\frac{\Delta E}{E} \approx 2\left[\frac{\Delta t_m}{t}\right] \otimes \left[\cot\theta \Delta\theta\right] \otimes \left[\frac{\Delta d}{d}\right] \tag{4.11}$$

[2] In this sense the term *spectrometer* explicitly refers to an instrument which measures *inelastic* scattering events.

where t is the total time of flight from the moderator to the detector plane, $\Delta\theta$ is the uncertainty in the Bragg angle at the analyser and $\Delta d/d$ is the uncertainty in the lattice spacing of the analyser crystal. The term, Δt_m, is the moderator pulse width for a given neutron energy, E. The ISIS hydrogen moderator will generate a width of $22\times\lambda$ (Å) μs at neutron wavelengths up to the peak of the Maxwellian, but at longer wavelengths the pulse width remains roughly constant (~120 μs). It should be noted that the first term will also included the timing variation due to the fact that each neutron will not travel along exactly the same path to reach the detector. In practice this is found to be a minor contribution.

4.13 Analyser Geometry

If the detectors are placed at the sample position, which is of course a physical impossibility, we will have a very high resolution, due to the fact that the analysed neutrons would have been totally back scattered, (i.e. $2\theta_A = 180°$), but we will be unable to obtain any information that is Q dependent. This is due to the fact that all the neutrons scattered at different angles would all be detected in the same detector. In order to resolve this problem, it make sense to move the detectors out from the sample either towards or away from the analysers, the former case is illustrated in Figure 4.29.

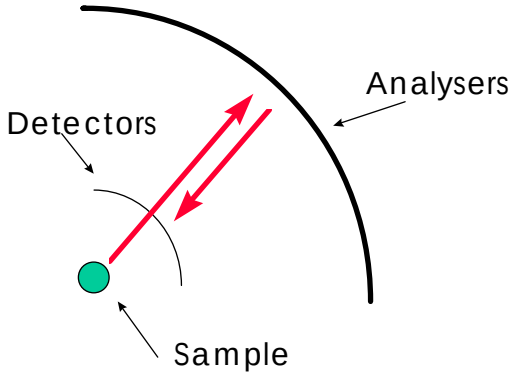

Figure 4.29: Movement of detectors from sample position outwards to enable Q dependent information to be resolved.

If we move the detectors to an off back-scattering geometry, we will lose resolution but gain intensity. For a totally back-scattering spectrometer the analyser crystals are mounted on a spherical surface. We therefore get no optical aberration caused by the analyser geometry, but once we move to an off back scattering geometry, we introduce aberration caused by the finite size of the sample and detector.

By using different crystal reflections, it is possible to achieve a different number resolutions, but still maintaining a fixed geometry, as can be seen in Figure 4.30 for the IRIS spectrometer. It must be noted that the intensities of the curves are not relative, but have been normalised to unity to enable greater clarity.

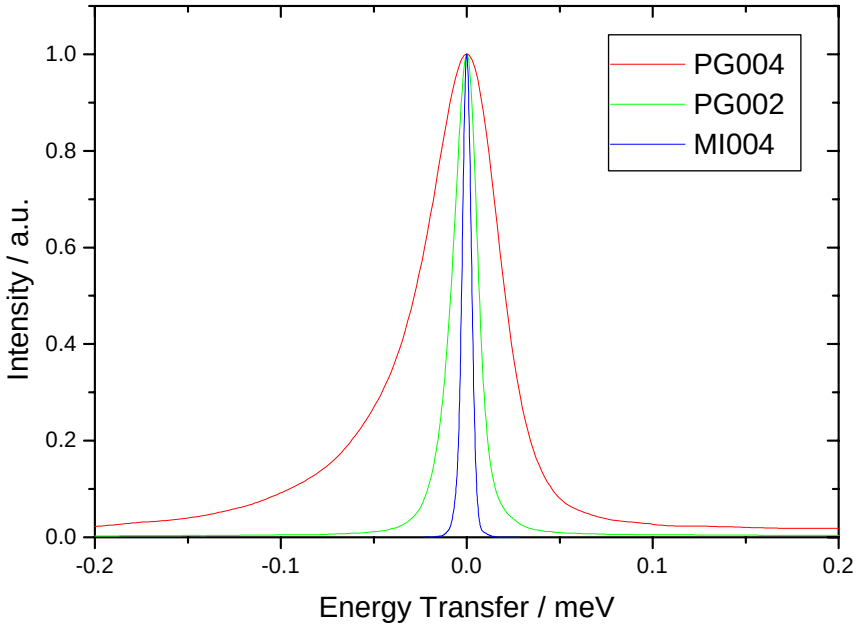

Figure 4.30: Measured resolution functions for several different analyser reflections for the IRIS spectrometer at the ISIS Facility.

4.14 Resolution Considerations

The resolution of the entire spectrometer can be separated into two distinct parts; the resolutions of the incident and secondary spectrometers. If we first consider the incident resolution, this is dominated by the contribution corresponding to the timing uncertainty in the time that the neutron was released from the moderator. In addition to this there is a contribution from the fact that all the neutrons do not travel the same distance in order to reach the sample. This is due to the fact that a certain number of neutrons will undergo reflections off the walls of the guide, resulting in a zig-zag trajectory to the sample. Also, the finite size and geometry of the sample and detector contribute to the variation in flight path.

It is important to have an understanding of which of these contributions is most important. A number of simulations were performed, each eliminating (where possible) a single component of the resolution (Figure 4.31). From these, it was seen that the most significant contributions were those from the $\Delta d/d$ and the

moderator time uncertainty. In order to investigate further the effect that the uncertainty in the lattice parameter of the analyser has on the final resolution, a number of simulations were performed in which Δd/d was varied from zero to 0.02. The results of these simulations can be seen in Figure 4.32.

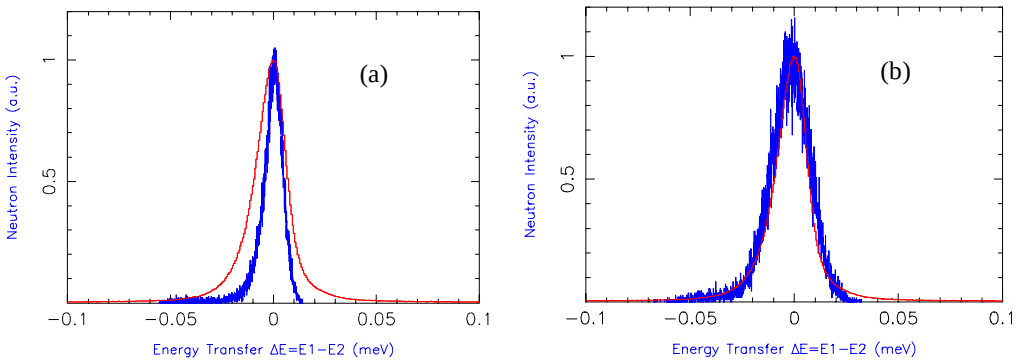

Figure 4.31: An illustration of how the resolution changes as we vary different contributions. By setting various contributions to zero such as (a) Δd/d and (b) the mosaic spread of the analyser crystals. The red curve is a vanadium measurement.

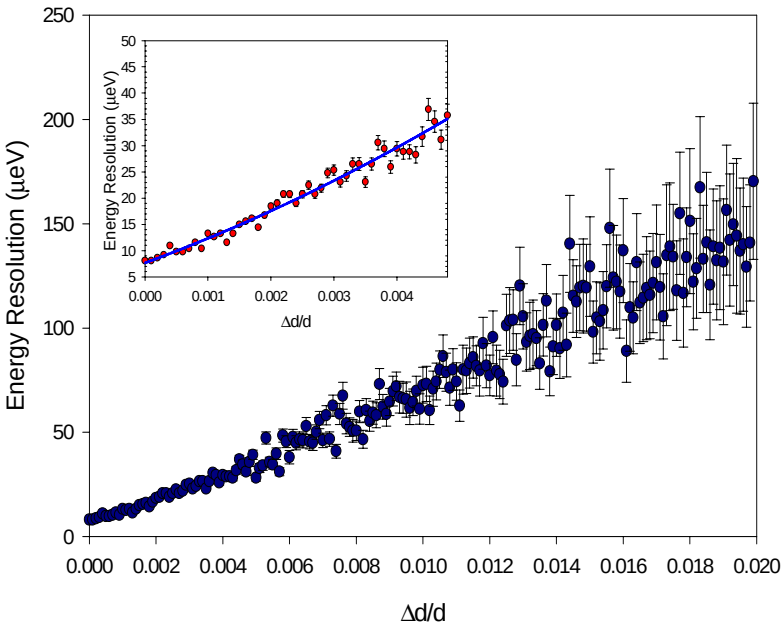

Figure 4.32: Effect on the energy resolution as we vary Δd/d for the analyser crystal. The inset graph is an enlargement of the region for values of Δd/d which are near to those quoted for the IRIS analysers. The solid line is a least squares fit to the polynomial $f(x) = ax^2 + bx + c$, *where* $a = 2.7 \times 10^5 \pm 1.3 \times 10^5$, $b = 4.4 \times 10^3 \pm 6.4 \times 10^2$ *and* $c = 7.7 \pm 0.7$. *The fit is only included as a guide for the eye.*

At a value for Δd/d = 0, then from Figure 4.32, we can see that the resolution reduces to 7.7 μeV. This value must include the angular and moderator contributions. In Figure 4.33 we can see the variation of the main components to the resolution. Therefore, we can see that a resolution of 7.7 μeV corresponds to a backscattering angle,θ , of ~88°, which is very similar to the design value of 87.5°.

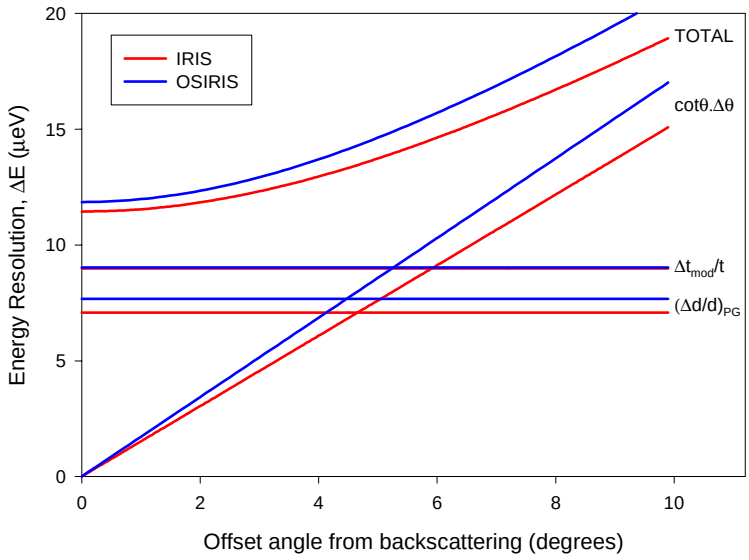

Figure 4.33:Simple analytical calculations of the energy resolution of the IRIS and OSIRIS spectrometers as a function of the angular offset from exact backscattering for the PG002 analyser reflection.

In order to ensure that the simulation was performing correctly a simulation of the IRIS spectrometer was performed and the results compared with a standard vanadium measurement. If we look at Figure 4.34, we can see that there is a shift in the peak position between the simulation and measurement. This is due to the fact that a number of the dimensions of IRIS are undocumented, so the distances used in the simulation may be slightly incorrect.

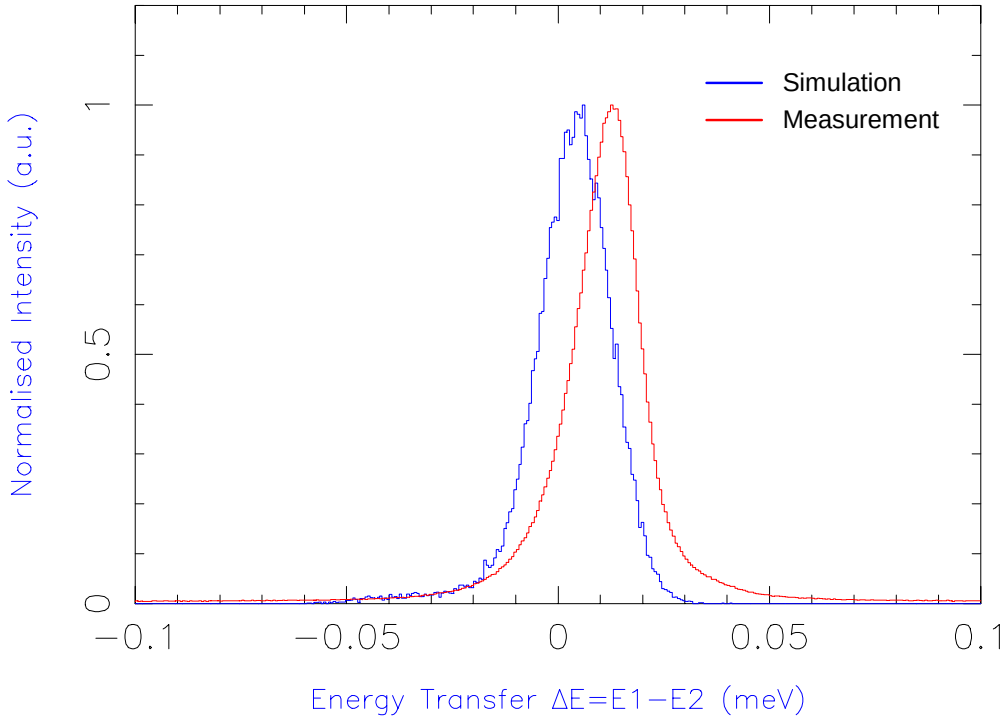

Figure 4.34: Simulation of the present IRIS spectrometer compared with a measured vanadium spectrum (run no. 11944) for an analyser with a value for Δd/d = 2.46 ×10-3.

4.15 Possible designs for the Analyser Bank

As mentioned earlier, as we move the detector into an off backscattering condition, then we introduce optical aberration effects which appears as a modified time-of-flight spread at the detector. This is due to either a variation in the analysed neutron energy or in difference in scattered path lengths between the sample and detector for different positions on the analyser bank. The shape of the analysers needs therefore to be modified in order to minimise these effects. Two configurations of the analyser are immediately obvious, one which provides a constant scattering angle at the analyser (hence constant wavelength) and the other that will give a constant flight path, see Figure 4.35. In reality, it is probably more sensible to use a combination of these two geometric shapes. For a constant flight path, the most obvious shape would be an ellipse with focii at the centres of the detector and sample, this however introduces quite a large variation in the resolution as we extend the analyser bank out of the sample

plane. It has been found that if we place the centre of each individual analyser crystal on a locus of constant path length and then rotate until we obtain a constant value for $2\theta_B$ at each crystal then we obtain the best overall resolution.

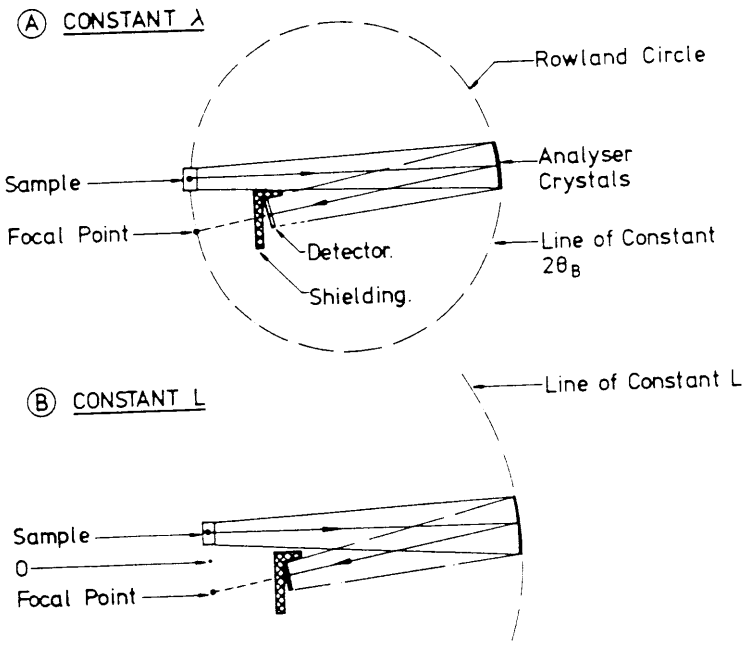

Figure 4.35: Two possible geometric configurations for the analyser banks in a off backscattering geometry. One of which provides a constant analysed wavelength and the other a constant secondary flight path. Taken from Carlile and Adams (1992).

4.15.1 Extending the IRIS Analyser bank

Recently, it has been decided to increase the area of the graphite analyser bank on IRIS and also cool the analyser down to 5 K. A proposed configuration for this upgrade of the IRIS analyser bank is detailed in Table 4.4. The sample position is assumed to be at the origin. The angles that are given indicate a rotation about the crystal centre, positive values indicate a clockwise rotation. This configuration will give an average secondary flight path of 1.485 m and an analysed energy of 1.823 meV. The expected resolution profile is shown in Figure 4.36 together with a simulation of the IRIS spectrometer with its present

configuration. Also listed in Table 4.4 are orientation angles for each crystal if they were positioned as to always reflect neutrons towards the centre of the detector.

Table 4.4: Co-ordinates and orientations of the graphite analyser crystals for the proposed IRIS upgrade. The values stated are for a vertical section through the sample tank at a scattering angle of 90°. Also shown are the orientation angles required to focus the neutrons onto the detector.

X (cm)	*Y (cm)*	*Angle (°)*	*Focus (°)*
84.415	5.500	-6.228	-8.242
84.553	4.500	-5.546	-7.450
84.677	3.500	-4.867	-6.660
84.787	2.500	-4.189	-5.871
84.882	1.500	-3.512	-5.082
84.965	0.500	-2.837	-4.294
85.033	-0.500	-2.163	-3.506
85.087	-1.500	-1.490	-2.719
85.128	-2.500	-0.818	-1.932
85.155	-3.500	-0.146	-1.145
85.168	-4.500	0.525	-0.358
85.167	-5.500	1.195	0.429
85.153	-6.500	1.865	1.217
85.125	-7.500	2.535	2.005
85.083	-8.500	3.205	2.794
85.027	-9.500	3.875	3.583

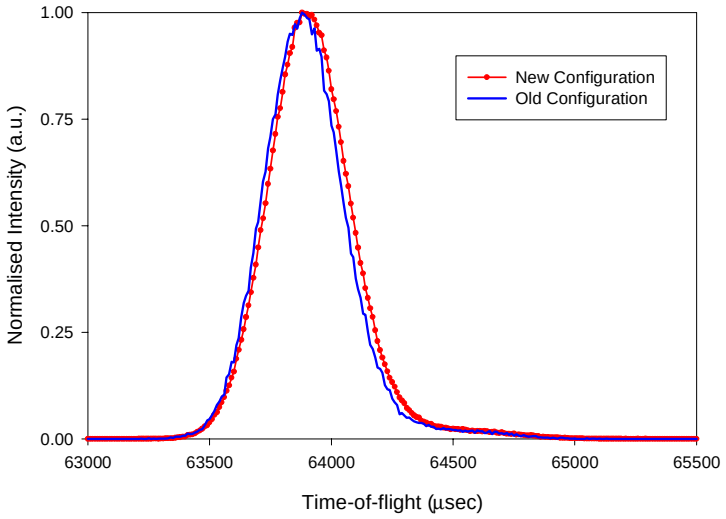

Figure 4.36: Simulations of the IRIS spectrometer with its present configuration of 6 analyser crystals (-) as compared to the proposed upgrade to 16 crystals (-).

4.15.2 Expected performance of OSIRIS

A schematic representation of the geometry of the OSIRIS spectrometer can be seen in Figure 4.37. The distance Y_{sd} will vary depending on what value is chosen for the backscattering angle (or analysing energy). A summary of possible values is given in Table 4.5. Monte Carlo simulations were performed for backscattering angles of 170° and 175° for two different vertical positions. These results are shown in Figure 4.38 and Figure 4.39. Detailed configurations for these two cases are listed in Table 4.6.

Table 4.5: Values of the vertical distance to the detector for a given backscattering angle

$2\theta_B$	Y_{sd}
170°	10.23 cm
171°	9.19 cm
172°	8.15 cm
173°	7.12 cm
174°	6.10 cm
175°	5.10 cm

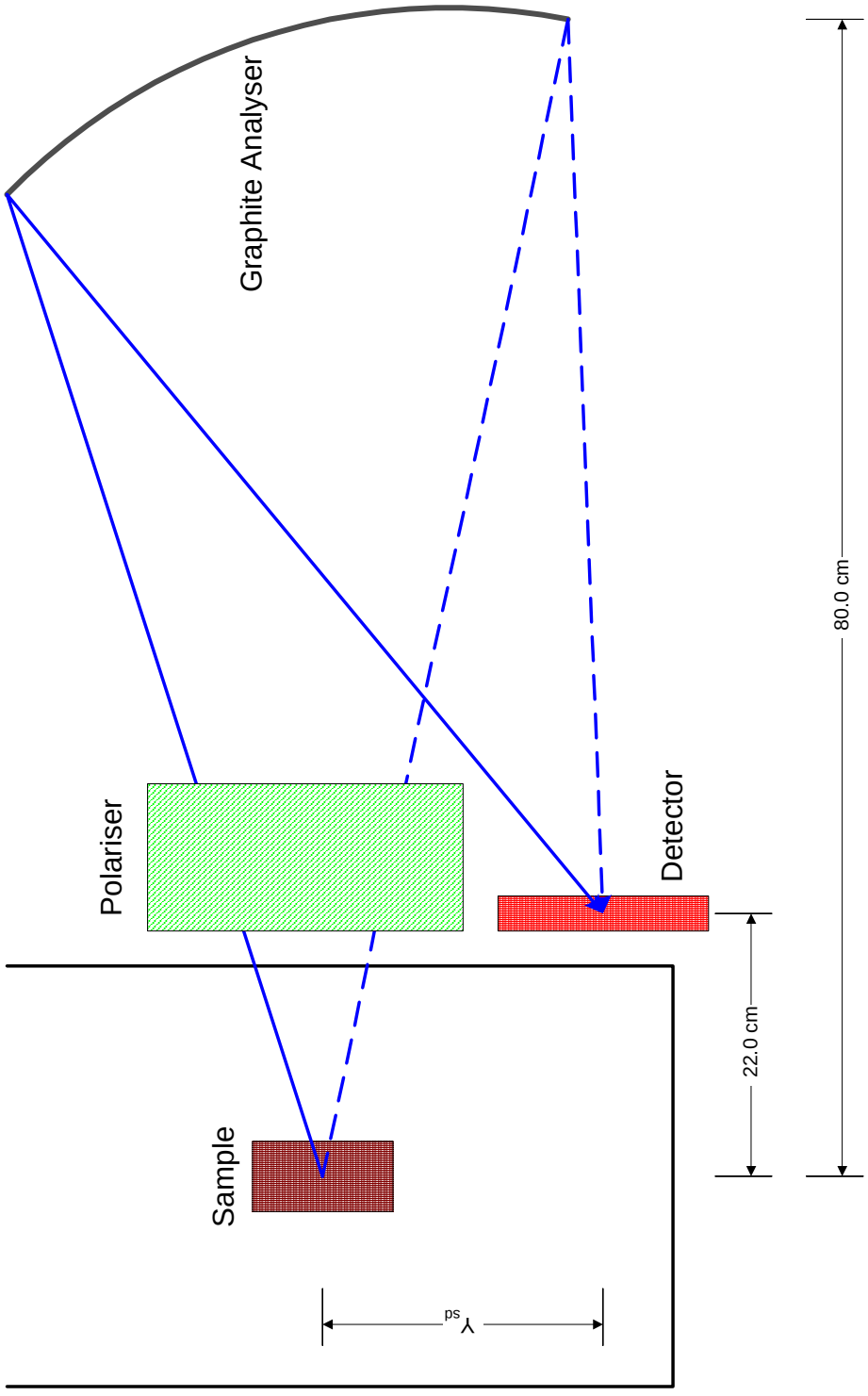

Figure 4.37: A schematic representation of the proposed geometry for the OSIRIS spectrometer.

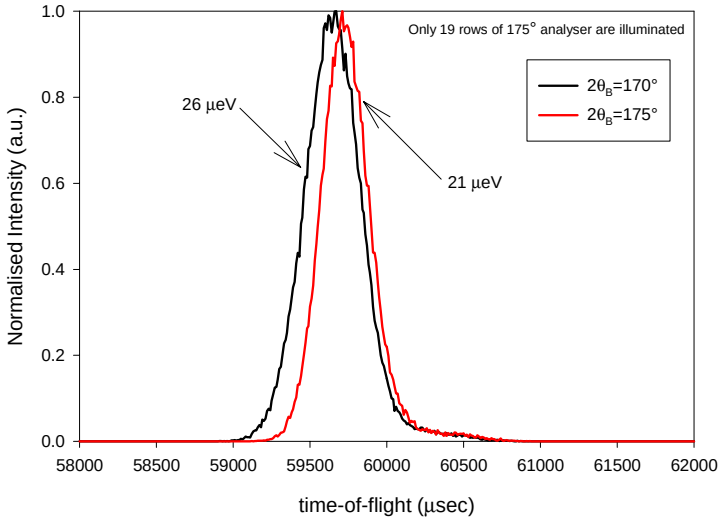

Figure 4.38: Simulated resolution profile of the OSIRIS spectrometer with a 30 cm high analyser bank positioned correctly for the 170° case.

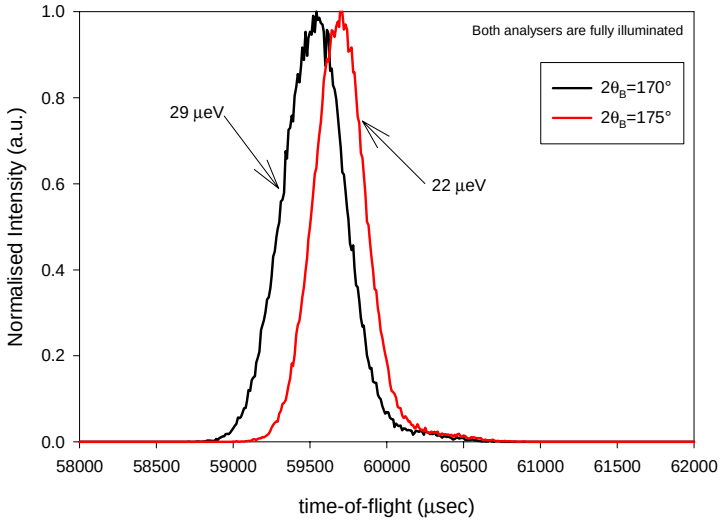

Figure 4.39: Simulated resolution profile of the OSIRIS spectrometer with a 30 cm high analyser bank positioned correctly for the 175° case.

The two vertical configurations of the analyser bank arise from the condition that the bottom of the analyser array is positioned so that it should be just visible from the sample without any part being masked by the detector (see Figure 4.37). If we satisfy this condition for $2\theta_B = 170°$, then the top of the analyser array should be positioned ~10 cm (case A) above the sample plane, and for $2\theta_B = 175°$ we obtain a displacement value of ~21 cm (case B). If we now use the vertical

Table 4.6: Positions and orientations for two possible configurations of the OSIRIS analyser bank. Also shown are the orientation angles required to focus the neutrons onto the detector.

Case A				*Case B*			
X (cm)	*Y (cm)*	*angle (°)*	*focus (°)*	*X (cm)*	*Y (cm)*	*angle (°)*	*focus (°)*
78.488	9.500	-11.901	-13.077	75.864	20.500	-17.621	-20.271
78.712	8.500	-11.163	-12.220	76.225	19.500	-16.850	-19.376
78.921	7.500	-10.429	-11.365	76.568	18.500	-16.083	-18.486
79.115	6.500	-9.697	-10.512	76.894	17.500	-15.321	-17.599
79.293	5.500	-8.968	-9.660	77.203	16.500	-14.564	-16.717
79.455	4.500	-8.242	-8.811	77.495	15.500	-13.811	-15.838
79.602	3.500	-7.518	-7.962	77.769	14.500	-13.061	-14.963
79.734	2.500	-6.796	-7.115	78.029	13.500	-12.316	-14.090
79.852	1.500	-6.076	-6.269	78.272	12.500	-11.573	-13.221
79.954	0.500	-5.358	-5.424	78.499	11.500	-10.834	-12.354
80.042	-0.500	-4.642	-4.579	78.710	10.500	-10.098	-11.490
80.114	-1.500	-3.927	-3.735	78.906	9.500	-9.365	-10.627
80.172	-2.500	-3.214	-2.892	79.086	8.500	-8.635	-9.767
80.216	-3.500	-2.502	-2.048	79.250	7.500	-7.906	-8.909
80.244	-4.500	-1.790	-1.204	79.399	6.500	-7.180	-8.053
80.258	-5.500	-1.080	-0.361	79.532	5.500	-6.456	-7.198
80.257	-6.500	-0.370	0.483	79.651	4.500	-5.734	-6.344
80.241	-7.500	0.340	1.328	79.755	3.500	-5.013	-5.491
80.210	-8.500	1.049	2.173	79.843	2.500	-4.293	-4.639
80.165	-9.500	1.758	3.020	79.917	1.500	-3.575	-3.788
80.105	-10.500	2.468	3.867	79.976	0.500	-2.858	-2.938
80.029	-11.500	3.177	4.716	80.020	-0.500	-2.142	-2.088
79.939	-12.500	3.887	5.565	80.049	-1.500	-1.426	-1.238
79.834	-13.500	4.598	6.417	80.063	-2.500	-0.712	-0.388
79.714	-14.500	5.309	7.270	80.062	-3.500	0.003	0.462
79.579	-15.500	6.022	8.126	80.047	-4.500	0.718	1.313
79.430	-16.500	6.735	8.983	80.017	-5.500	1.432	2.164
79.264	-17.500	7.450	9.843	79.971	-6.500	2.147	3.015
79.082	-18.500	8.167	10.705	79.911	-7.500	2.862	3.867
78.885	-19.500	8.885	11.570	79.836	-8.500	3.577	4.721

displacement of 10 cm, but use a 170° configuration, then we find that the bottom 11 rows of the analyser bank are obscured by the detector. If, on the other hand we use the vertical offset of 21 cm, then the analysers are fully illuminated for both values of $2\theta_B$. The penalty in terms of lost resolution in moving the analyser higher is very small when we consider the increase in flux that we will obtain. From these simulations, we can say that there are basically two possible configurations for OSIRIS. The first setup (case A) will have a scattering angle

of 170° yielding a resolution of 26 μeV with the top of the analyser at ~10 cm above the sample plane. Secondly (for case B), the backscattering angle would be set to a value of 175°, which would increase the resolution ΔE=22 μeV, but it would mean that the analyser would have to be shifted vertically in order to prevent masking by the detector.

4.16 Conclusion

A Monte Carlo code to simulate the performance of an inverted geometry crystal analyser spectrometer has been developed. It is possible to use the program to simulate the spectrometer in three ways, simulation of the (i) primary spectrometer, (ii) secondary spectrometer or (iii) both simultaneously. For case (iii), the simulation is very complex and CPU intensive, it therefore takes a long time to perform in order to obtain reasonable statistics. If we wish to optimise various components, it is often better to initially simplify the simulation by using either (i) or (ii), until we have reduced the number of possibilities.

Using these simulations (together with analytical calculations), it has been possible to propose optimum configurations for the polarising benders and inelastic analyser array for use in the OSIRIS spectrometer.

There are basically two options for the OSIRIS analyser bank; either (i) use a backscattering angle of 170°, in which we obtain a resolution of ~26 μeV or (ii) have a slightly higher value of $2\theta_B$ =175°, which would mean an improved resolution with a value of ~22 μeV. Both of these solutions has its own merits. For the case of a higher analysing angle, we gain in the most obvious way, in terms of an improved resolution. The benefits of using a slightly lower angle are not quite as obvious, but as OSIRIS is to be a full polarised analysis instrument, then spin analysers will have to be placed in the scattered beam, which requires a more open geometry, which this configuration provides. Further study is required into the spatial necessities before a decision is reached on which

analyser option is selected. One possible positioning of a spin analyser is shown in Figure 4.37.

An important use of these simulations was the ability to quickly address and quantify various problems that arose during the construction of OSIRIS.

An instrument, MITED, for measuring multireflectivity has been developed and commissioned. The device occupies the VESTA beamline as a parasitic instrument to IRIS and may be operated independently (provided the chopper phases are set as to provide neutrons in the required region). It is now possible to measure the reflectivity of any two surfaces that are positioned facing each other with a small separation in order to form a microguide. This method has been used to test the reflectivity of various sections of glass that were used in the OSIRIS neutron guide.

Chapter 5

C-15 Laves Phase Compounds

5.1 Introduction

A number of experiments have been performed on several of C-15 Laves phase intermetallic compounds. This is a family of materials whose properties can be studied in detail using the OSIRIS spectrometer and diffractometer. As the construction of this instrument will not be completed within the time scale of this thesis, a number of experiments were performed on other instruments. The samples that have been the subject of this investigation are HfV_2H_x, $ZrTi_2H_x$ and $TiCr_{1.85}H_x$.

5.2 Choice of Samples

The samples under investigation have been chosen because together they exhibit a number of unique features in comparison to other C-15 compounds. HfV_2 is a typical C-15 structure, whereas $ZrTi_2$ only becomes C-15 upon hydrogenation and then it is thought that the e-site is most readily occupied as opposed to the more usual g-site. In $TiCr_{1.85}$, we do not have the exact stiochiometric ratio of 2B atoms to every A atom, so we will have some substitution of A atoms onto B sites, which will result in a changing of the geometry in a number of the tetrahedral interstitial sites.

Typical C-15 site	*Modified site*
2A-2B (g-site)	3A-1B (g`-site)
1A-3B (e-site)	2A-2B (e`-site)
4B (b-site)	1A-3B (b`-site)

Table 5.1 : Effect on the tetrahedral interstitial sites of a C-15 Laves structure of substituting a B-type atom with an A-type atom.

We must note that for the case of an e-site (1Ti-3Cr) becoming a e` (2Ti-2Cr) site, although it has the same nearest neighbour atoms as a g-site, it will not have exactly the same site symmetry as a 'normal' g-site. The same also applies for the transition of a b-site to a b`-site which will have a different configuration to a normal e-site.

5.3 Sample Preparation

The intermetallic alloys $TiCr_{1.85}$, HfV_2 and $ZrTi_2$ were prepared by melting the relative amounts of the constituent metals in an arc furnace under an atmosphere of argon. The purity of the metals before melting was greater than 99.95%. Before performing the hydrogenation procedure the sample was annealed at the appropriate temperature (973 K, 1273 K and 873 K for the $ZrTi_2$, $TiCr_{1.85}$ and HfV_2 samples respectively) under vacuum ($<10^{-6}$ mbar) for 16 hours in the case of $ZrTi_2$ (or 15 days for $TiCr_{1.85}$ and 24 hours for HFV_2). The annealing stage is especially important for the $TiCr_{1.85}$ sample where both the C-14 and C-15 phases can be present. Hydrogen was added to the sample (hydrogen purity > 99.999%) at a given temperature $T_A(ZrTi_2)$ = 873 K, $T_A(TiCr_{1.85})$ = Room Temp and $T_A(HfV_2)$ = 650 K using a volumetric rig (see Figure 5.1). The amount of hydrogen absorbed by the sample was determined by measuring the pressure drop in a calibrated volume. X-ray and neutron diffraction measurements were performed in order to verify the correct phase of the sample and to accurately determine the lattice parameter. A summary of these results can be found in the next section.

5.4 X-ray / neutron diffraction.

In order to ensure that the samples used in each of the studies performed was in the correct phase, X-ray diffraction (XRD) measurements were performed at 295 K and the results are summarised in Table 5.2.

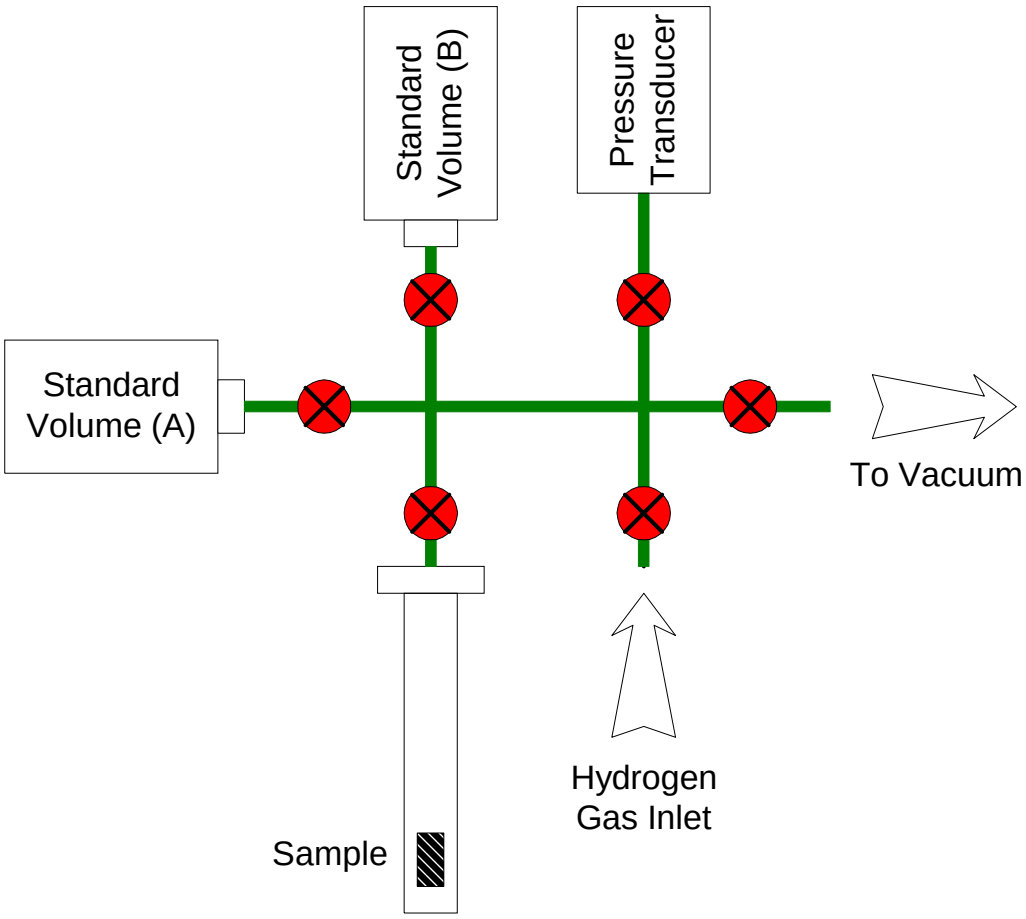

Figure 5.1: Schematic diagram of the hydrogenation rig used to prepare the samples.

Sample	*Lattice Parameter (Å)*
$TiCr_{1.85}$	6.938
$TiCr_{1.85}H_{0.43}$	6.998
HfV_2	7.389
$HfV_2H_{0.3}$	7.441
$ZrTi_2H_{5.4}$ (fct)[1]	a=4.66 c=4.45
$ZrTi_2H_{3.6}$ (C-15)	8.16

Table 5.2: Summary of the lattice parameter obtained from XRD measurements on the various samples used.

The variation of the lattice parameter of $TiCr_{1.85}$ with hydrogen concentration is shown in Figure 5.2.

[1] Space group $I4_1/a$ (lattice parameter value obtained from Fernandez 1998)

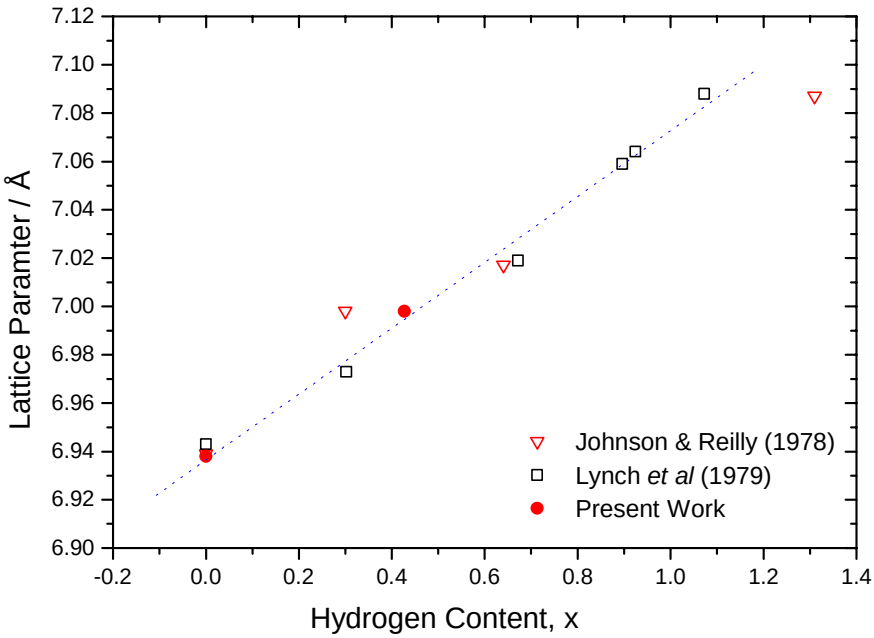

Figure 5.2: The variation of the lattice parameter of $TiCr_{1.85}H_x$ with hydrogen concentration, x. The dotted line is only shown as a guide for the eye.

Examples of the XRD patterns along with the fitted refinements are shown in Figure 5.5, Figure 5.6 and Figure 5.7. The sample was measured using an open slab geometry, therefore we do not observe any reflections arising from the sample holder.

Neutron diffraction measurements have also been made on $HfV_2H_{0.3}$ using the OSIRIS instrument at ISIS. Three different patterns were recorded at 200 K, 160 K and 50 K. Figure 5.3 shows the complete patterns for 200 K and 50 K, the peaks that originate from the cryostat are marked with arrows. These were determined by performing an empty cryostat measurement. The pattern recorded at 160 K is not shown because it is almost identical to the 200 K run. There is clear evidence that some structural phase change occurs when we decrease the temperature (see Figure 5.4a & Figure 5.4b).

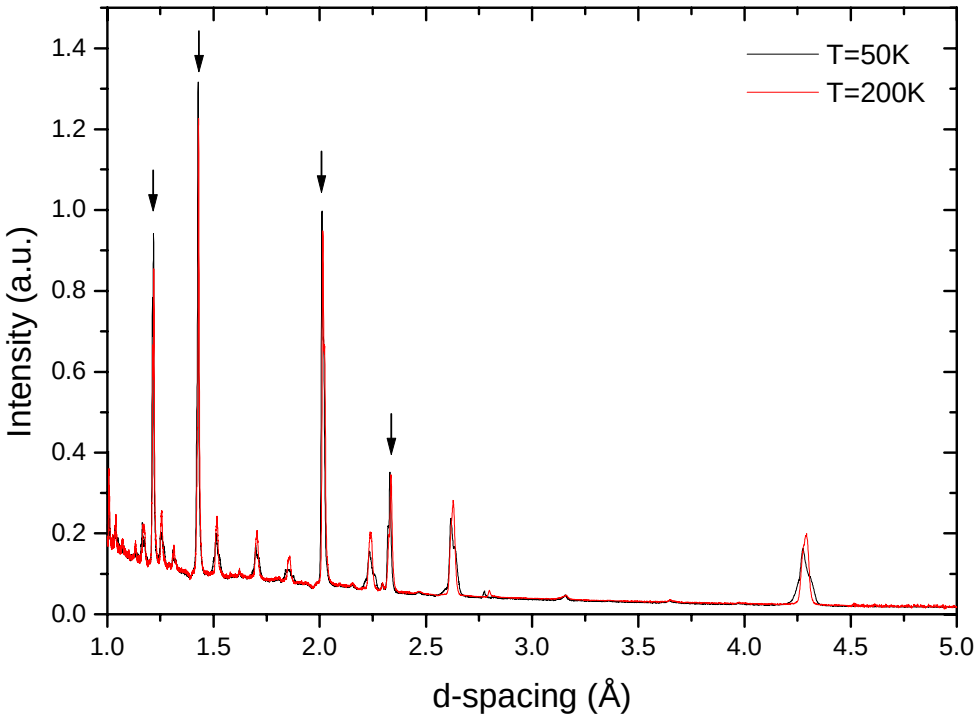

Figure 5.3: Neutron diffraction pattern of $HfV_2H_{0.3}$ at two different temperatures, T=200K (red) and T=50K (black). Arrows mark the peaks due to the sample container and cryostat.

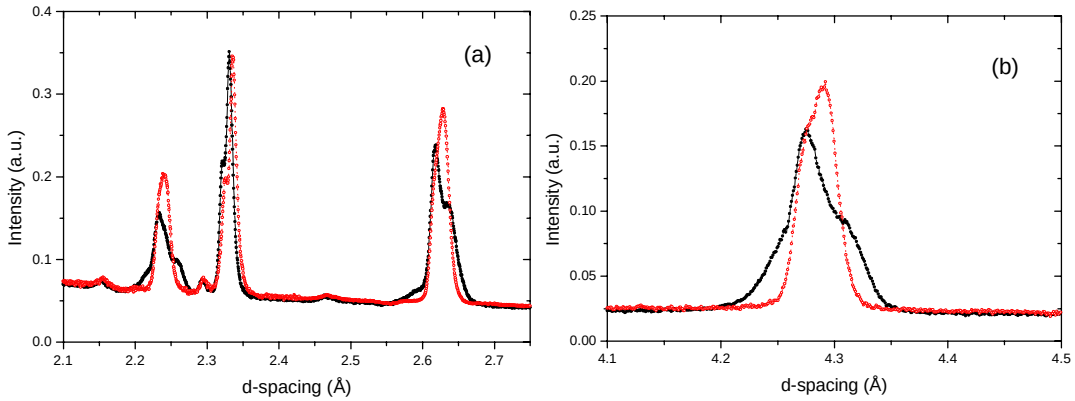

Figure 5.4: Magnification of various sections of the neutron diffraction patterns that are shown in Figure 5.3.

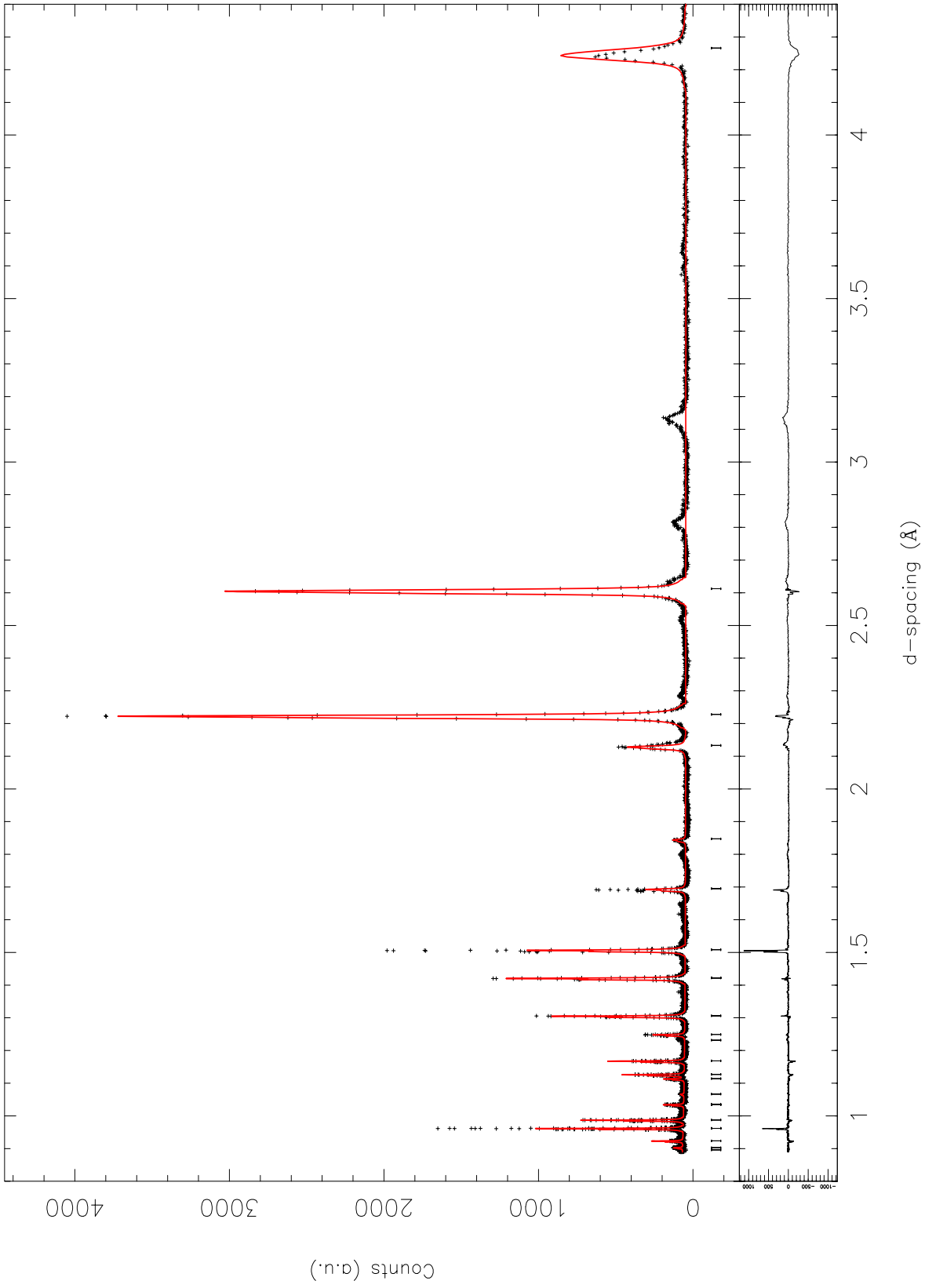

Figure 5.5: X-ray powder diffraction measurement of HFV_2.

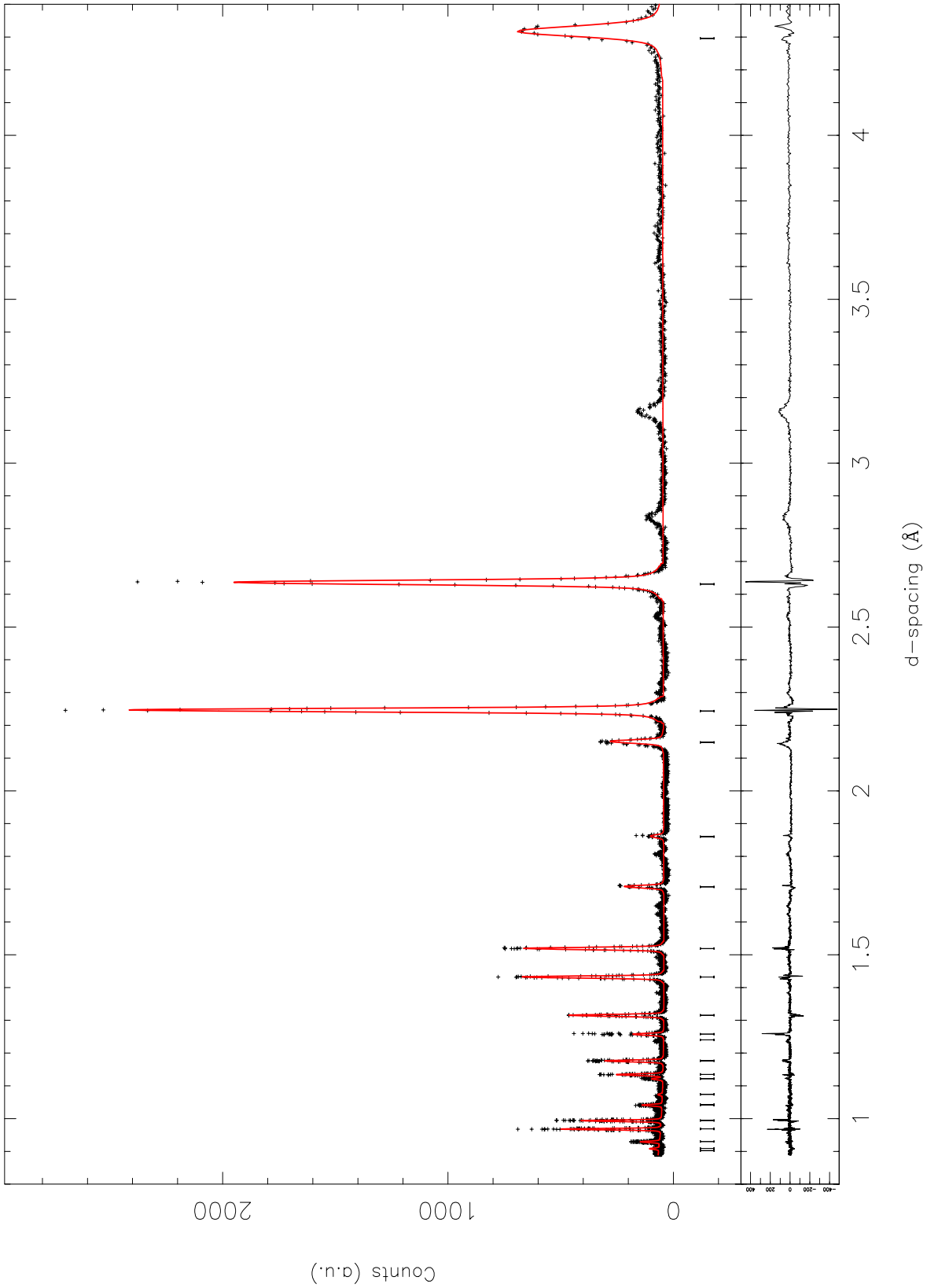

Figure 5.6: X-ray powder diffraction measurement of $HFV_2H_{0.3}$.

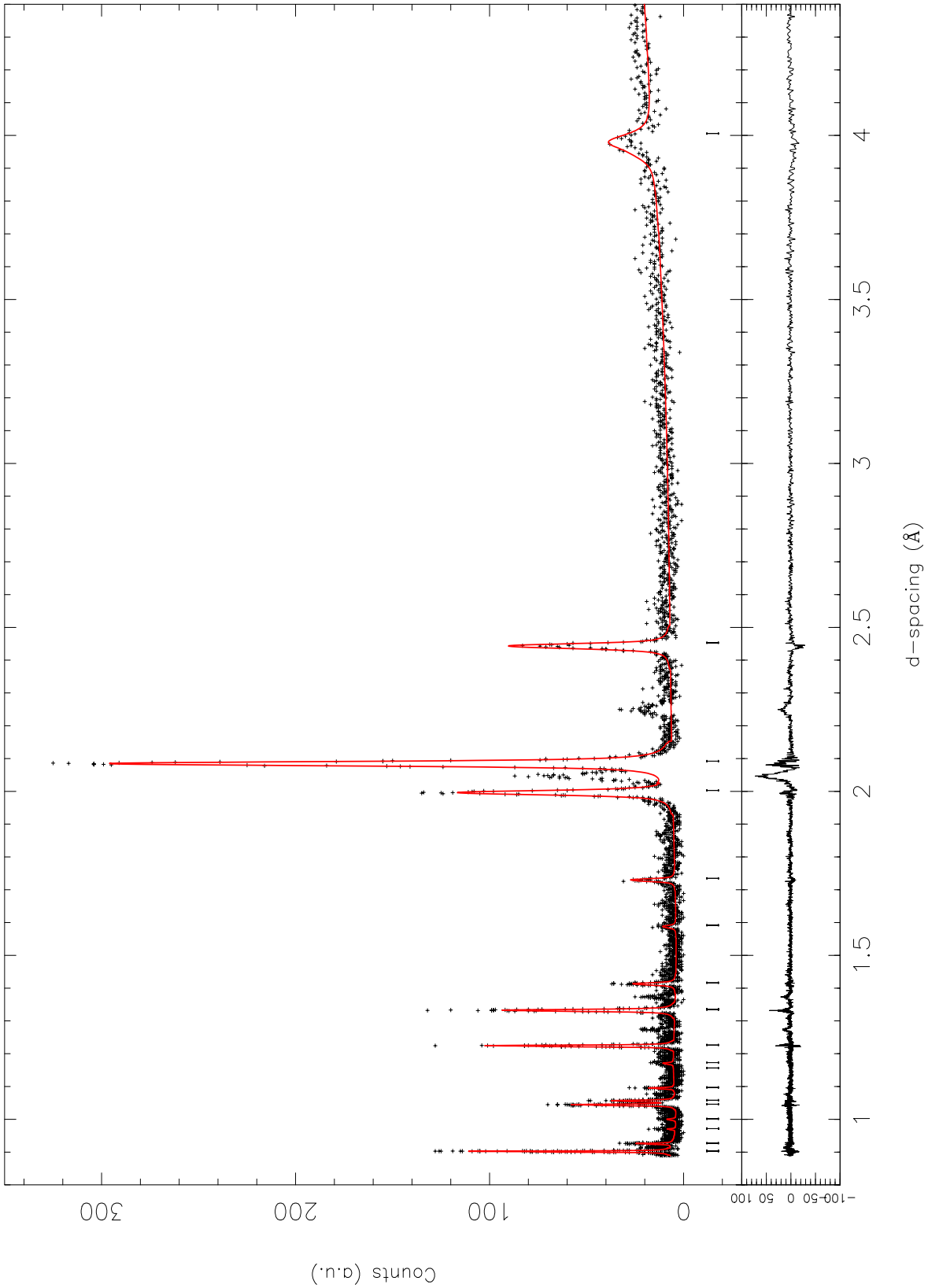

Figure 5.7: X-ray powder diffraction measurement of $TiCr_{1.85}$.

5.5 Quasi-elastic neutron scattering measurements

5.5.1 Experimental procedure

Quasi-elastic neutron scattering (c.f. section 2.4) measurements have been carried out on two different samples, $HfV_2H_{0.3}$ and $TiCr_{1.85}H_{0.45}$ using the IN10 spectrometer at the ILL (for a detailed description of this instrument, refer to Section 3.6.2). The general experimental procedure and analysis is the same for both samples.

The samples were prepared in the manner described in section 5.3. The sample can used was an aluminium flat cell (dimensions: 2.9 × 3.9 cm), and was loaded with a sample thickness of 1 mm. The thickness of sample was chosen so as to try to minimise any multiple scattering contributions yet maximise the single scatter signal. The sample can was orientated at ϕ=110° to the incident neutron beam (see Figure 5.8).

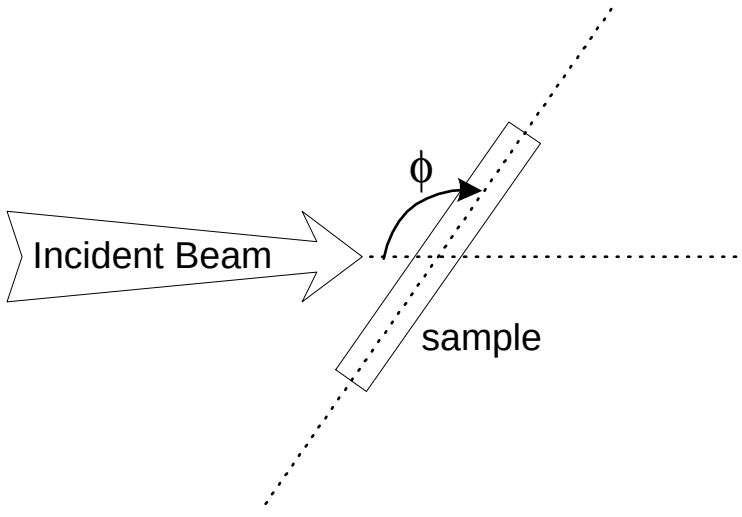

Figure 5.8: Schematic diagram of the sample orientation, ϕ, with respect to the incident beam for the quasi-elastic neutron scattering experiments performed on the IN10 spectrometer.

Measurements were made over a temperature range from 313 to 442 K for the $TiCr_{1.85}H_{0.43}$ sample and from 275 to 365 K for the $HfV_2H_{0.3}$ sample by using a cryo-furnace.

The simplest way to obtain the resolution function for the spectrometer is to perform a measurement with a standard incoherent scatterer, such as vanadium, in the beam. In addition an unloaded sample was measured to provide an estimate of the elastic contribution from the metal.

5.5.2 Analysis Procedure

The analysis of the collected data was carried out using two different methods. Firstly, the data was converted into S(Q,ω) form by using the standard instrumental data reduction routines, `SQW` (Randl, 1996). This process included corrections for various effects such as absorption and detail balance factors. The spectrometer has eight individual detectors, and these can be either used individually or added together in order to improve the statistics obtained. The resultant data were then treated in two separate manners; (i) fitted using the `PROFIT` program, which minimises χ^2 by using a least squares fitting method and (ii) fitted using the `QUASILINES` which is part of the `IDA` package (Howells, 1996) and which employs a method known as Bayesian analysis (Sivia, 1992a&b; 1993). The `QUASILINES` program makes use of the `MEMSYS3` maximum entropy algorithms of Gull and Skilling (Sivia 1996). The advantage of performing the analysis using the maximum entropy method over normal curve fitting is that it provides an estimate of the relative probability of a given fit being consistent with the data.

Both methods could describe the present data well, by fitting a single Lorentzian plus an elastic contribution, whilst folding in the resolution function of the spectrometer. The fitted parameters for both methods agreed with each other within errors.

Multiple scattering corrections were made for a single spectrum using the DISCUS program. The results showed that there was little or no noticeable multiple scattering from the sample within the experimental errors.

5.5.3 $TiCr_{1.85}H_{0.45}$ Results

The scattered spectrum was measured as a function of temperature simultaneously at eight discrete values of Q. A typical spectrum with good statistics was measured over a time of approximately 12 hours, examples of which can be seen in Figure 5.9.

One point that we must be aware of when trying to analyse and interpret quasi-elastic scattering data, is that we may have some Bragg reflections within the range of Q that is measured by the spectrometer. This would result in a drastic increase in intensity and no quasi-elastic broadening and therefore the analysis would give misleading results. It is very difficult to correct the data for this kind of effect, so it is best to either arrange the analyser/detector system to avoid any Bragg reflections or just to ignore any data collected in these regions. In the present experiment, the former solution was employed based on measured diffraction data. We therefore can be reassured about the validity of the observed data.

By looking closely at the data, it is possible to see a small peak on the energy gain side of the spectrum. This was found to be an artefact of the cryofurnace that was used and was taken into account during the fitting process.

If we plot the broadening as a function of Q^2 in the low-Q region, then the gradient of this curve is equal to $\hbar D_t$ (see section 2.4.1). The plot of this low-Q region is shown in Figure 5.10 and the values of D_t that were obtained in Table 5.3.

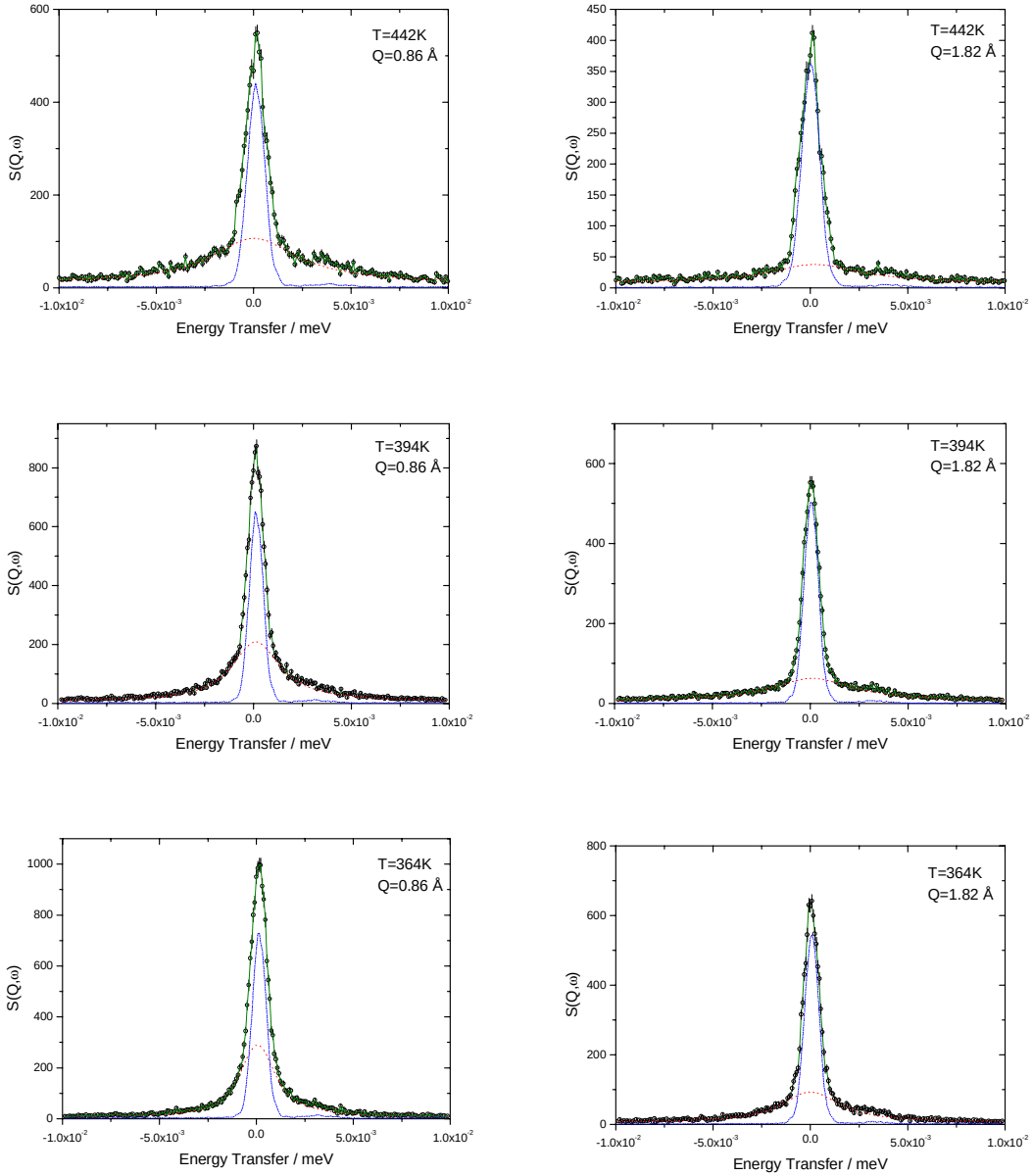

Figure 5.9: Measured spectra for $TiCr_{1.85}H_{0.43}$ at two different values of the momentum transfer, Q, as a function of three different temperatures.

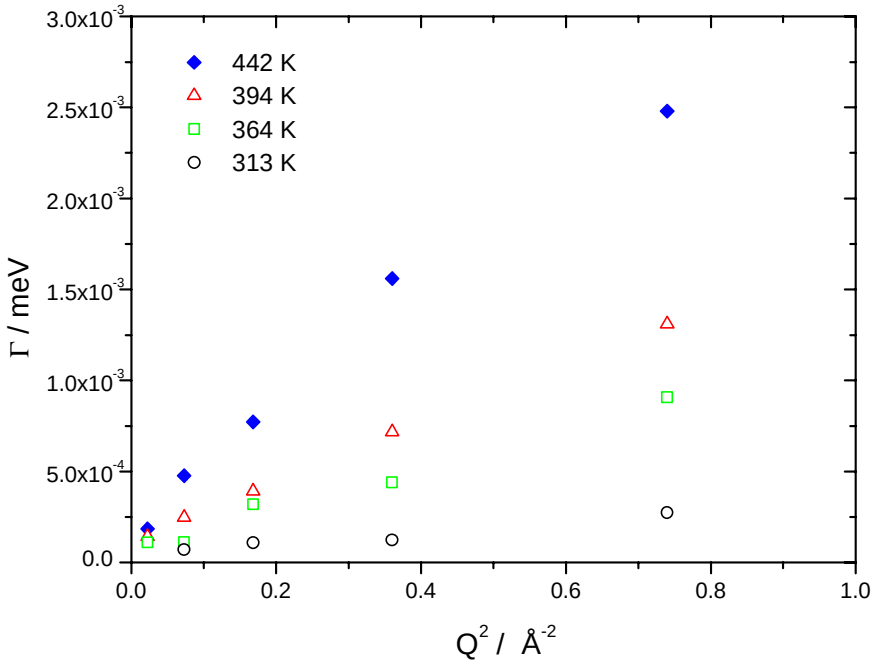

Figure 5.10: Broadening as a function of Q^2 for low-Q values for $TiCr_{1.85}H_{0.45}$.

Temperature (K)	D_t (m^2s^{-1})
313	4.509×10^{-12}
364	1.592×10^{-11}
394	2.551×10^{-11}
442	6.032×10^{-11}

Table 5.3: Values for D_t obtained from a linear fit to the low-Q region of the HWHM against Q^2 curve for $TiCr_{1.85}H_x$.

It is reasonable to assume that the hydrogen diffusion within the lattice can be described by the Arrhenius equation;

$$D(T) = D_0 \exp\left(-\frac{E_a}{k_B T}\right) \qquad (5.1)$$

where E_a is the jump activation energy. From the equation (5.1) we can see that there is a linear relationship between the natural logarithm of the mean jump time

and inverse temperature. Thus plotting such a graph for the data in Table 5.3, we obtained a linear relationship shown in Figure 5.11 (similar curves for individual detectors are shown in Figure 5.14). The gradient of the curve yields an activation energy of 0.237 ± 0.008 eV, which is in general agreement with an activation energy of 0.19 ± 0.02 eV that was obtained by NMR (*Bowman et al.*, 1983) in the temperature range of 190-280 K

.

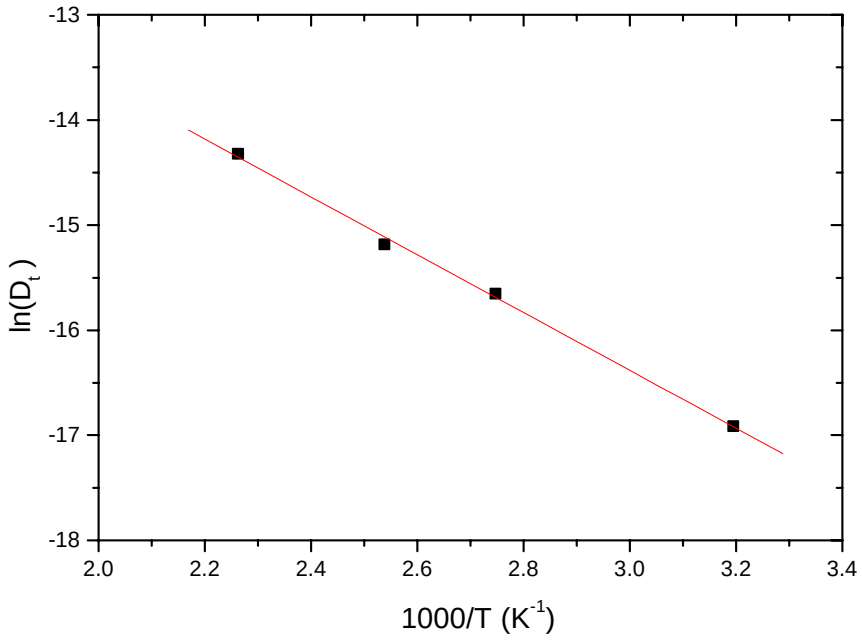

Figure 5.11: Graph of ln(D_t) versus reciprocal temperature.

Let us now consider the behaviour of the broadening over the entire range of measured Q values. If the diffusion paths involve two types of site, and diffusion is by a series of uncorrelated jumps, the quasi-elastic scattering will give rise to one Lorentzian at low Q with a broadening of D_tQ^2. At higher Q, however, it will break into two superimposed Lorentzians with widths that asymptotically approach broadenings of $\hbar/\tau$ for each site. In the present cases (i.e. $TiCr_{1.85}H_x$ and HfV_2H_x), if we accept that only the g-site is occupied i.e. the diffusing atom only stops momentarily on the e-site, the broadening observed will be determined by the residence time on the g-site.

The observed variation of Γ as a function of Q is shown in Figure 5.12. This type of shape is typical of jump diffusion. In order to obtain parameters from this data, we have fitted the polycrystalline averaged Chudley-Elliott model;

$$\Gamma = \frac{6\hbar D_t}{\ell^2}\left(1 - \frac{\sin(Q\ell)}{Q\ell}\right) \tag{5.2}$$

where D_t is the tracer diffusion coefficient and ℓ is the average jump length. The characteristic time, τ, is related to these quantities by the expression;

$$\tau = \frac{\ell^2}{6D_t} \tag{5.3}$$

Initially, a fit using a single value of ℓ for all temperatures was performed, the results of these fits can be seen as the solid lines in Figure 5.12. Next, a simultaneous fit of the data to equation (5.2) was performed, but this time, allowing both D_t and ℓ to vary, (see Table 5.4) these are the red dotted lines in Figure 5.12. The goodness of the fit was measured against all the spectra simultaneously.

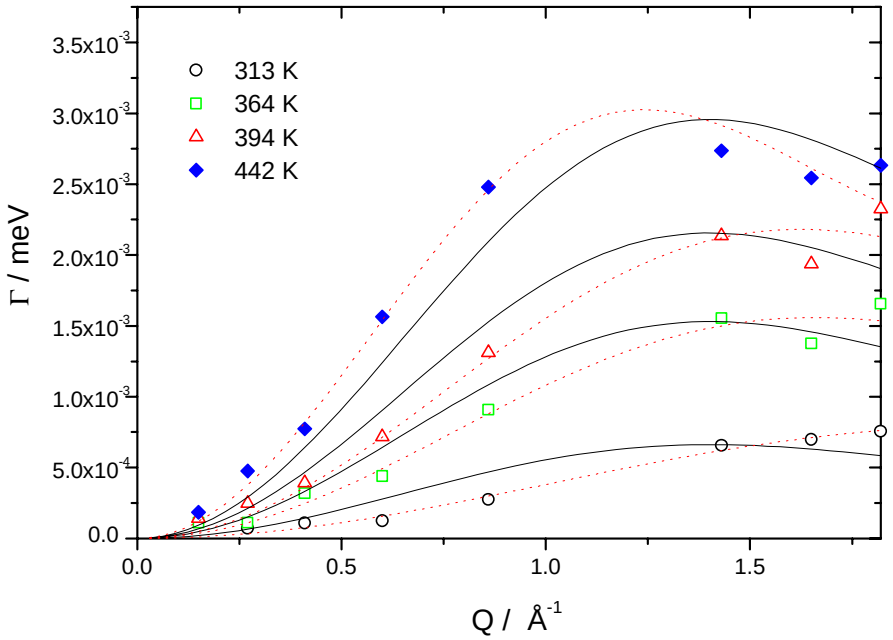

Figure 5.12: Quasi-elastic broadening of $TiCr_{1.85}H_{0.43}$ as a function of momentum transfer, Q at four different temperatures. The lines are fits to the polycrystalline version of the Chudley-Elliott model using an average jump length (solid) and varying jump lengths (dotted).

Temperature (K)	*ℓ (Å)*	*τ (×10^{-12} sec)*
313	3.20 ± 0.10	1.21 ± 0.19
364	fixed @ 3.20	0.52 ± 0.04
394	fixed @ 3.20	0.37 ± 0.02
442	fixed @ 3.20	0.27 ± 0.01
313	2.60 ± 0.24	1.15 ± 0.07
364	2.71 ± 0.18	0.51 ± 0.02
394	2.76 ± 0.13	0.37 ± 0.01
442	3.62 ± 0.08	0.26 ± 0.01

Table 5.4: Parameters obtained from simultaneous fits to the polycrystalline C-E model for a fixed average jump length and a varying one.

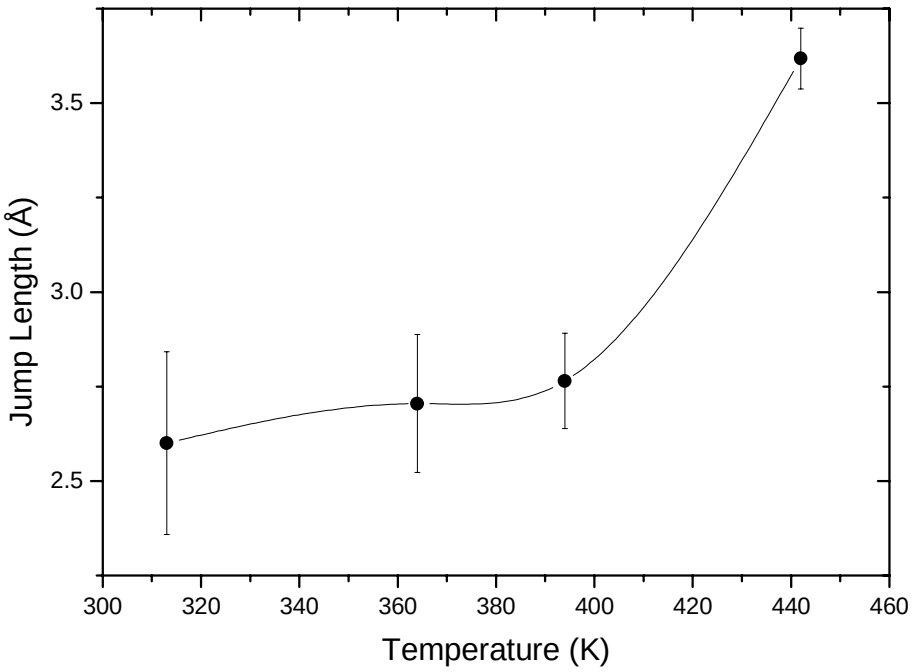

Figure 5.13: Variation of the fitted jump length with temperature. The solid line is intended only as a guide for the eye.

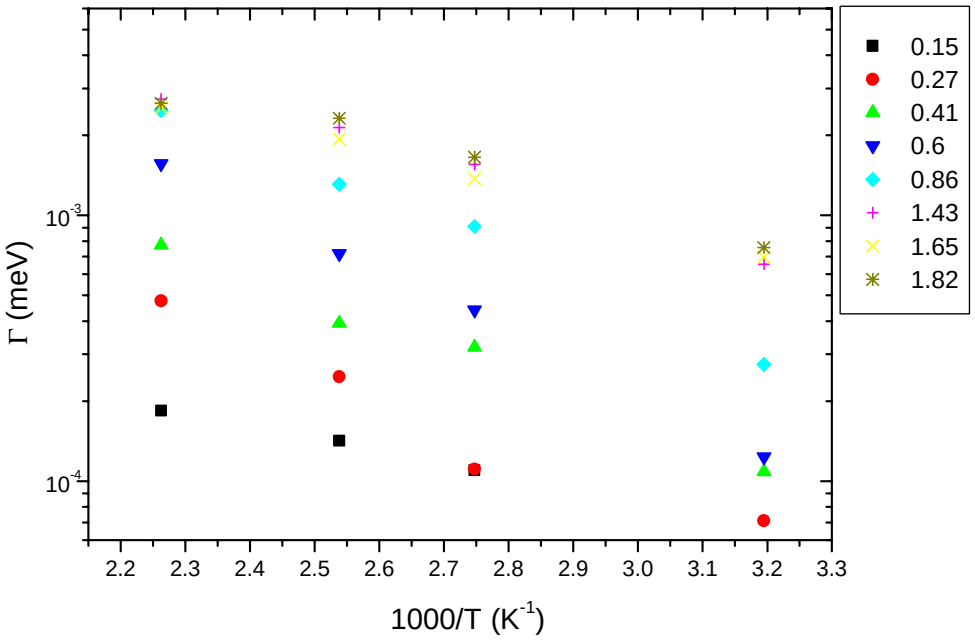

Figure 5.14: The quasi-elastic line width, Γ, as a function of reciprocal temperature for each of the eight detectors.

5.5.4 $HfV_2H_{0.3}$ Results

During this experiment, we experienced instrumental problems with the Doppler drive unit on the monochromator, the frequency of which was varying with time. This resulted in a loss in the available measuring time, and therefore we were not able to measure as many spectra (with good statistics) as we originally planned.

It was only possible to measure data with good statistics at two temperatures, 273 and 295 K. The half-width at half maximum, Γ, as a function of the momentum transfer, Q, is shown in Figure 5.15. The rest of the experimental time was filled with measurements at a number of different temperatures in the range 250 to 380 K, but these proved to have insufficient statistics to give any information on the Q-dependence of the broadening.

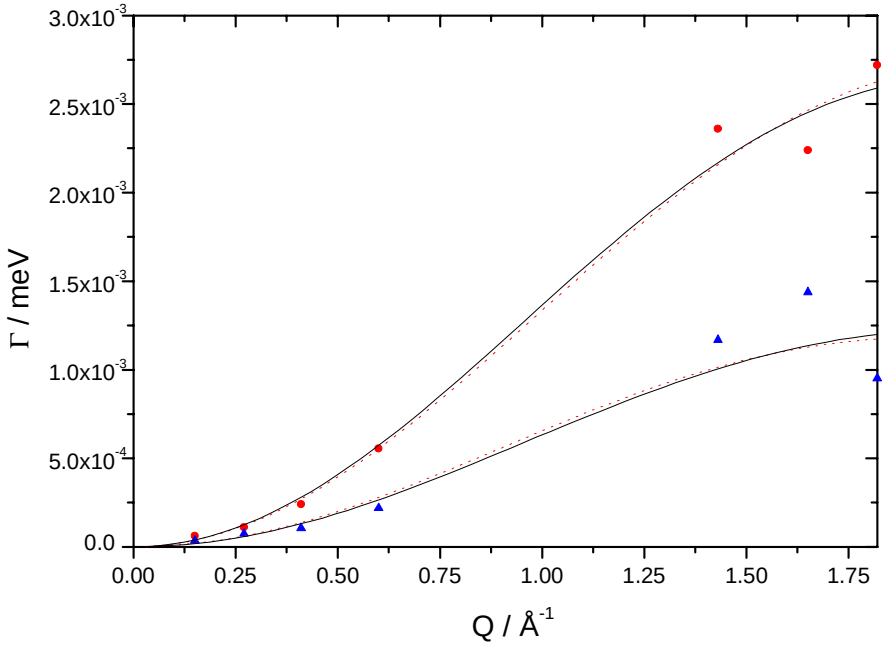

Figure 5.15: Q-dependence of the broadening for $HfV_2H_{0.3}$ at temperatures of (σ) *273 K and* (λ) *295 K.*

As for the $TiCr_{1.85}$ data, we fitted the broadening to the polycrystalline version of the Chudley-Elliott model (equation 5.2). The data at both temperatures can be well described by using a single average jump length of 2.49 ± 0.23 Å or 2.18 ± 0.20 Å if we exclude detector #5 which was found to be noisy. This value agrees completely with that found by Havill *et al* (1989) using neutron measurements, who concluded that the value of the jump length lay somewhere between 2 and 2.5 Å. If we again plot (Figure 5.16) the broadening as a function of Q^2, then we see a straight line dependence, the numerical values obtained are shown in Table 5.5.

Temperature (K)	D_t (m^2s^{-1})
273	22.63×10^{-12}
295	8.02×10^{-12}

Table 5.5: Values obtained for D_t *from fitting the low-Q data.*

The runs that were measured having poorer statistics have been used to estimate an overall average activation energy (Campbell *et al*; 1997). It was necessary to group several detectors together in order to obtain better statistics. If we plot the results on

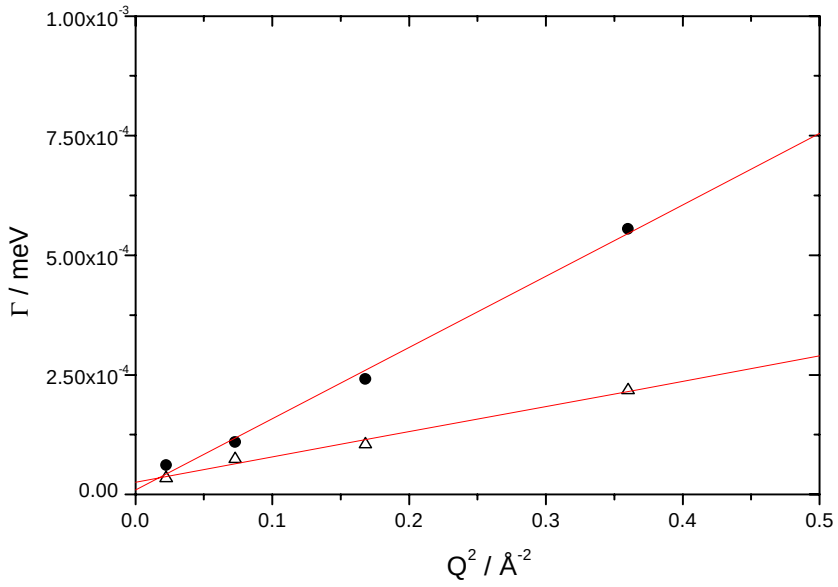

Figure 5.16: Broadening as a function of Q^2 for low-Q values for $HfV_2H_{0.3}$.

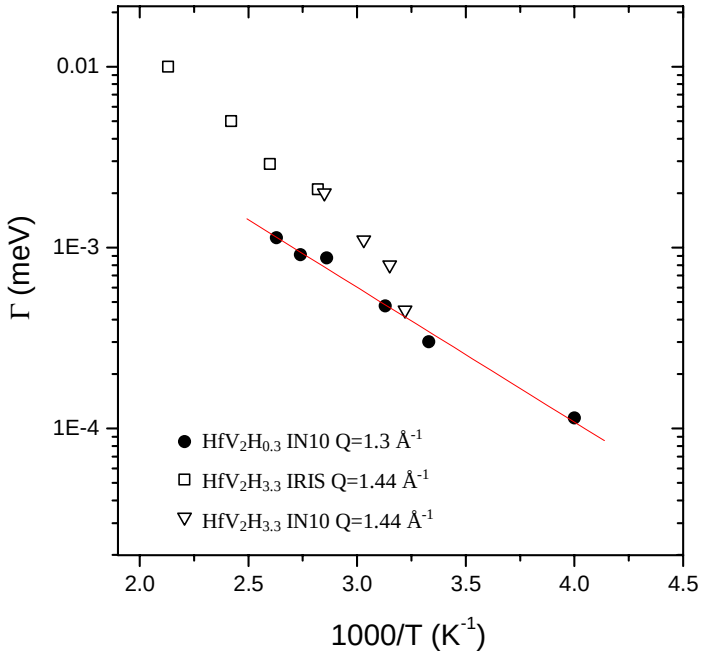

Figure 5.17: Comparison of the quasi-elastic broadening, Γ, observed as a function of reciprocal temperature for the present measurements (•), *to those made by Havill* et al *(1989).*

graph of *ln*(Γ) versus reciprocal temperature, then we see a straight line Arrhenius dependence (Figure 5.17). This provides us with an activation energy of 0.15 ± 0.01 eV, which is in general agreement with measurements made on this hydride at higher concentrations, E_a = 0.22 eV.

5.5.5 Discussion

Firstly, let us start by looking at the results obtained for the $TiCr_{1.85}$ sample. The method used in fitting the Q-dependence of the data leaves us with two ways of looking at the data; (i) firstly we can assume that we are seeing just an average jump length process over the entire temperature range, or alternatively, (ii) the average jump length seems to vary as a function of temperature (Figure 5.13). By looking at the two fits, it can be argued that the second option gives a much better description of the data, but we must be careful that we are not over interpreting the data.

Let us consider what possible processes could cause such a change. Skripov *et al* (1996, 1998) have proposed that at low temperatures (lower than used here) the hydrogen motion is localised within the hexagon formed by g-sites and only at higher temperatures does jump diffusion set in.

The diffusion path followed by the hydrogen atoms is going to be, by the nature of the network of available sites, complex. The network of e-sites and g-sites is shown in Figure 5.18.

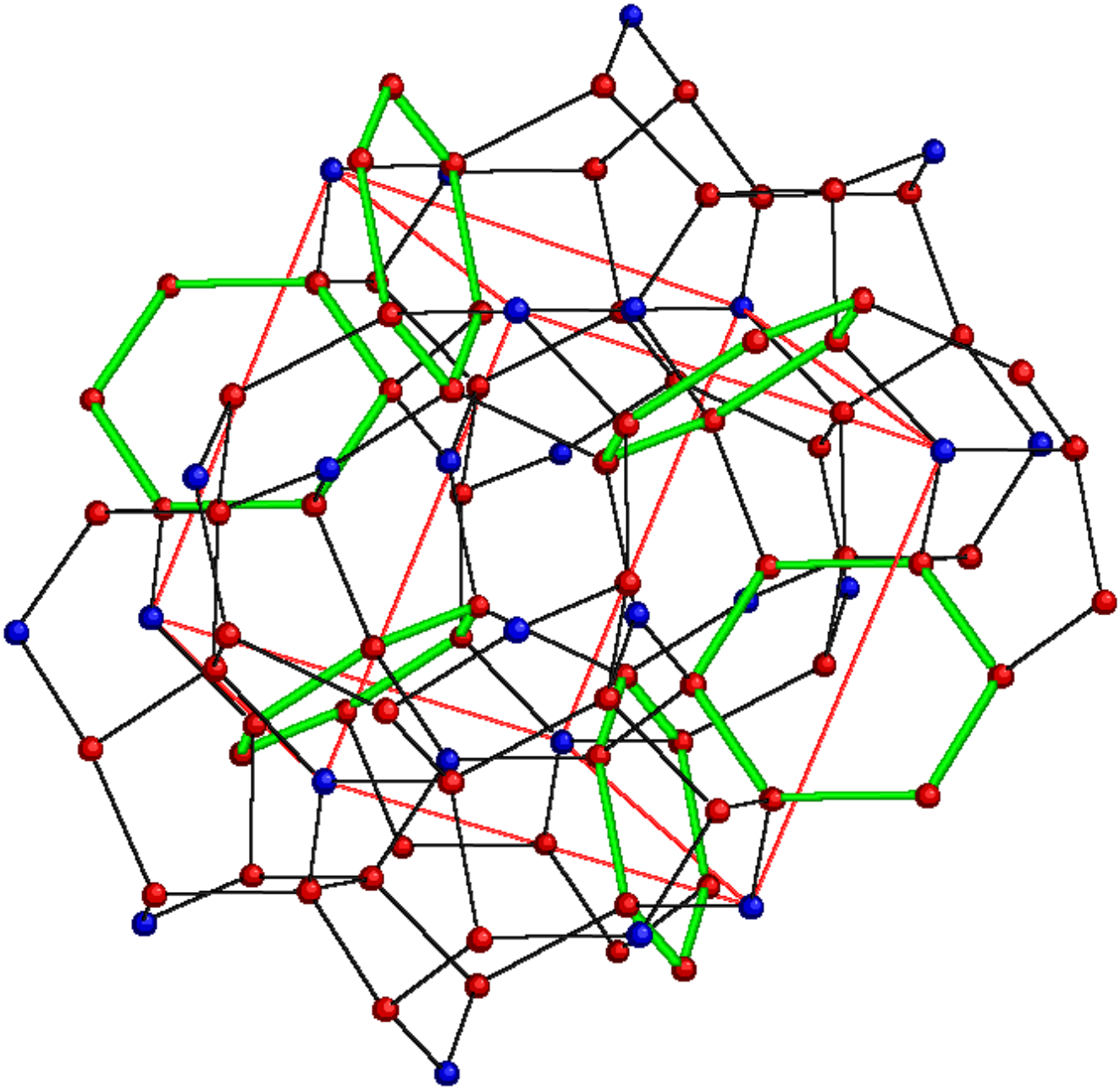

Figure 5.18: Network of e-sites (blue spheres) and g-sites (red spheres) for an ideal $MgCu_2$ (C-15) crystal structure. The hexagons of g-sites are shown in green. The fcc sublattice of e-sites is shown by a red square.

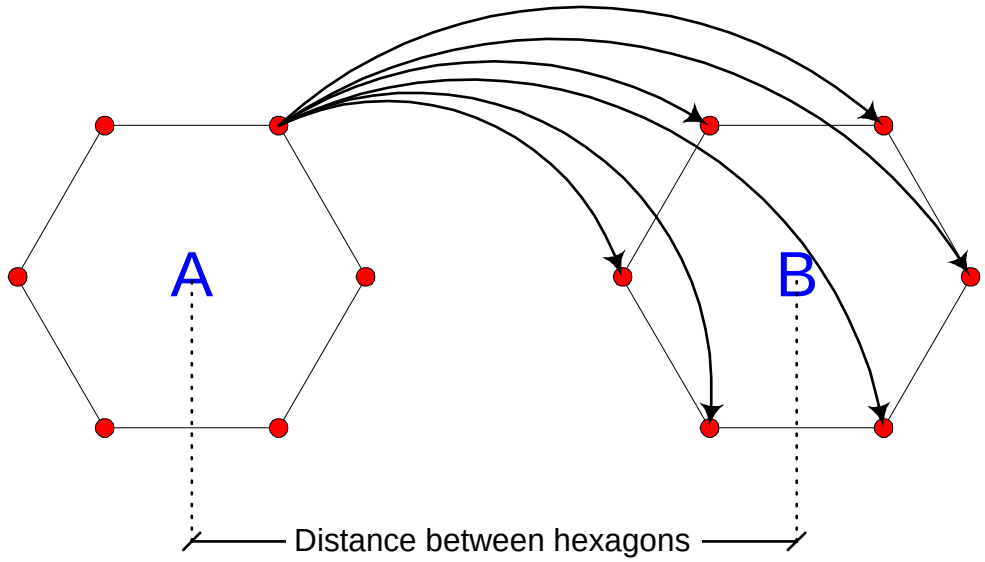

Figure 5.19: Schematic diagram showing the jump paths from one hexagon to another.

Let us first take a naïve look at the distances between sites. We first examine the assumption that the jump diffusion that is taking place is related to jumps between hexagons. It has been stated by Skripov & Hempelmann (1997) that for $ZrCr_2H_{0.5}$ the effective jump length obtained is 2.4 ± 0.2 Å, which they attribute to the H performing many jumps within a g-site hexagon before it, jumps to another hexagon.

If we now suggest a rather simplistic method of calculating the distance between g-site hexagons. The method used for calculating the average distance between adjacent hexagons is as follows. If we first consider a single site, *i*, on the hexagon A, and calculate the distance from this site to every site, *j*, on hexagon B (see Figure 5.19).

Therefore the average distance between hexagons is given by

$$\ell = \frac{1}{6}\sum_{i=1}^{6}\frac{1}{6}\sum_{j=1}^{6} r_{ij} \qquad (5.4)$$

This also may be used to calculate the distance between next nearest hexagons. The results of these basic calculations indicate that (for an ideal C-15 structure) the

average distance between nearest neighbour hexagons is $0.4044a_0$ and for next nearest neighbour hexagons, this increases to $0.636a_0$.

The question now is; "how does this relate to our experimental results ?" Well, if we take a_0 = 6.998 Å (for $TiCr_{1.85}H_x$) then the distance between hexagons is 2.83 Å which is in close agreement with our experimental values (see Table 5.4), but the values for the next nearest hexagons does not tie in with the observed change in the jump length.

If we surmise that the experimentally observed value is an average of two simultaneous processes, namely jumps between adjacent and next nearest hexagons then we arrive at a value of $0.5202a_0$ (=3.64 Å for $TiCr_{1.85}H_x$), which is close to the observed value of 3.62 ± 0.08 Å.

In the above argument, we have totally ignored the fact that we do not have an exact stoichometry of 1:2 of Ti to Cr.

Looking at the results obtained by Skripov and Hempelmann, assuming the lattice parameter of $ZrCr_2H_{0.5}$ to be ~7.23 Å, then using the above method we arrive at a jump length of 2.92 Å, which is rather higher than the experimentally observed value.

It was unfortunate that we were prevented from obtaining sufficient data for HfV_2H_x. The present results do, however, pose some interesting questions. The concentration used for the present experiment, x=0.3, was significantly lower than that used by Havill *et al* (1989), x=3.3. It has been suggested that at low concentrations the g-sites are occupied and it is only at higher concentrations (x>2.5) that the e-sites are also occupied. In the present experiment, we have a sufficiently low concentration to assume that it is only the g-sites that are occupied, but this would not be the case for measurements made with x=3.3. It is difficult to comment on why these two sets of measurements result in jumps lengths which are very similar. It is worth noting that the activation energies for the two experiments differ slightly from 0.15 eV (x=0.3) to 0.22 eV for x=3.3.

At present, a simulation method is being developed to provide an insight into the geometry of the diffusion in C-15 compounds (Bull *et al.*, 1998).

5.6 Muon Spectroscopy

Zero field muon spin relaxation measurements have been carried at the MuSR spectrometer at the ISIS facility for the samples, $HfV_2H_{0.15}$ and $ZrTi_2H_x$ (where x=3.6, 5.4) in order to determine the mean residence times of the muon at particular interstitial sites. For the $ZrTi_2H_x$ sample, measurements were performed on three different phases, namely face-centred tetragonal, C-15 and amorphous.

	Positive Muon μ^+	*Proton p*
Rest Mass *m*	$0.012610\ m_p$	1.6726×10^{-27} kg
Spin *I*	½	½
Magnetic Moment μ	$3.18334\ \mu_p$ 4.4905×10^{-26} JT^{-1}	1.41062×10^{-26} JT^{-1}
Gyromagnetic Ratio γ [rad s^{-1} T^{-1}]	8.5161×10^8	2.6752×10^8
Lifetime τ	2.197×10^{-6} s	stable

Table 5.6: Properties of the proton and positive muon.

5.6.1 Muon Production

The muon decays with a lifetime of $\tau_\mu = 2.2\ \mu s$, during this time the muon may be static or dynamic and its spin will be influenced by the spins of its environment. At the instant of its decay through the process;

$$\mu^+ \rightarrow e^+ + \bar{\nu}_e + \nu_\mu \qquad (5.5)$$

a positron is emitted preferentially in the direction of the muon's spin. The polarisation of the muon can be measured with time, since the polarisation at the instant of decay can be observed due to the anisotropy of the positron emission (Figure 5.20).

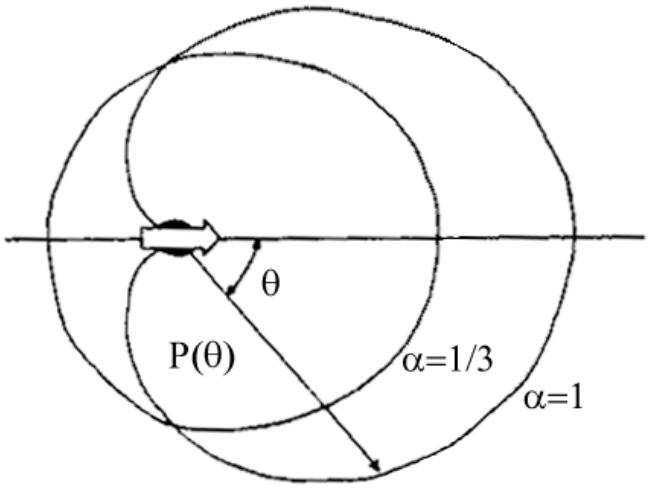

Figure 5.20: The angular distribution $P(\theta) = 1+a\cos\theta$ of the positron intensity. Averaged over all positron energies, a *= 1/3.*

5.6.2 Experimental Procedure and Analysis

These measurements were performed at the MuSR pulsed muon facility situated at the Rutherford Appleton Laboratory, UK. The samples were mounted onto a flat holder with a recess of 3 mm in depth to accommodate the sample and held in place with a thin sheet of milar. The temperature was varied from 9 to 365 K by means of a closed-cycle refrigerator (CCR) with built-in heater elements. The magnetic field at the sample position was adjusted so as to give a net field of zero. For each sample it is necessary to perform a calibration measurement in order to determine the asymmetry, α. This is accomplished by applying a transverse field of 20 Gauss to the sample and by fitting the measured spectra to the equation;

$$a_0 P(t) = \frac{N_F - \alpha N_B}{N_F + \alpha N_B} \qquad (5.6)$$

where a_0 is the instrumental asymmetry and N_F and N_B are the forward and backward count rates. We must be aware of the possibility of systematic errors that may occur due to uncertainty in determining the background. From these

measurements we obtained a number of values for the magnitude of α (see Table 5.7).

Sample	α
$HfV_2H_{0.15}$	1.67
$ZrTi_2H_{5.4}$ (face centred cubic)	1.20
$ZrTi_2H_{3.6}$ (C15 Laves phase)	1.21
$ZrTi_2H_{3.6}$ (Amorphous)	1.15
$ZrTi_2H_{3.6}$ (C15 Laves phase)	1.20

Table 5.7: Values for the instrumental asymmetry, α.

The value of α for the $HFV_2H_{0.15}$ sample seems unusually high. The instrumental alignment was therefore re-checked by performing a run with a silver sample. This gave a value of ~1.0 for α. The high value therefore arises as a feature of the sample or its geometry. Such a high value must be kept in mind when performing the analysis and may provide an explanation of strange results.

Initially, a Gaussian function was fitted to the first few microseconds of the data. From this it is possible to get an overall picture of the temperature dependence of Δ.

$$G(t) = \exp\left(-\Delta^2 t^2\right) \qquad (5.7)$$

Further analysis was performed using two methods, firstly the data were fitted using the UDA analysis package at ISIS, by fitting a dynamic Kubo-Toyabe function to the data. This was doubled-checked by fitting the strong collision version of the Kubo-Toyabe function (Hayano *et al.*, 1979; Kubo & Toyabe, 1967), the static form of which is;

$$G_z(t) = \frac{1}{3}\left[1 + 2\left(1 - \Delta^2 t^2\right)\exp\left(-\Delta^2 t^2/2\right)\right] \qquad (5.8)$$

In this expression, the polarisation falls from its initial value to a minimum at $\Delta t = \sqrt{3}$ and then returns to 1/3 of its initial value. In the strong collision version of the Kubo-Toyabe model (Hayano *et al.*, 1979), it is assumed that the correlation of the local field is lost when the muon jumps and that the characteristic time, τ, associated with the correlation decay is usually identified as the mean residence time of the muon at a given site having fixed surroundings.

5.6.3 $ZrTi_2H_x$ (x=3.6,5.4) Results and discussion.

The width, Δ, of the fitted Gaussian, as described by equation (5.7), is shown in , for each of the different samples of $ZrTi_2H_x$ in Figure 5.21 -Figure 5.23.

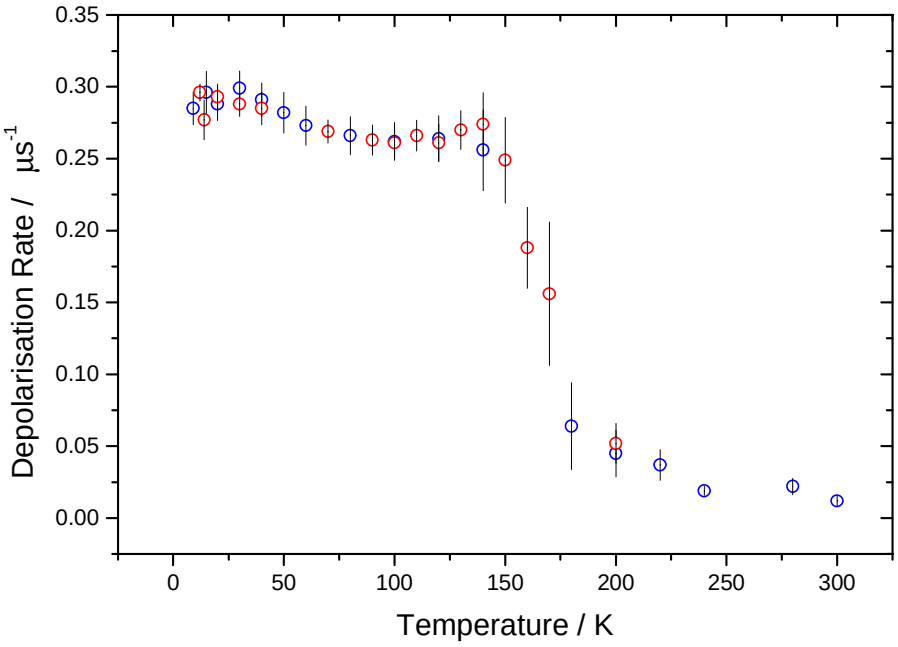

Figure 5.21: Zero Field Gaussian depolarisation rates for $ZrTi_2H_{3.6}$ with C-15 laves phase structure. The red and blue markers are to represent separate measurements on the two C-15 $ZrTi_2H_{3.6}$ samples.

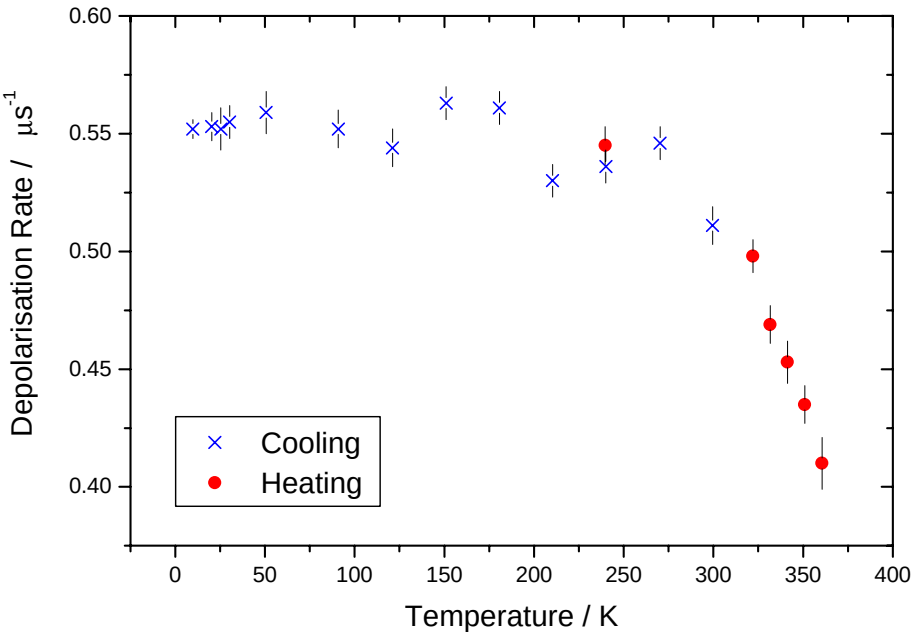

Figure 5.22: Fitted initial depolarisation of the face centred cubic (tetragonal) form of $ZrTi_2$ with a simple Gaussian.

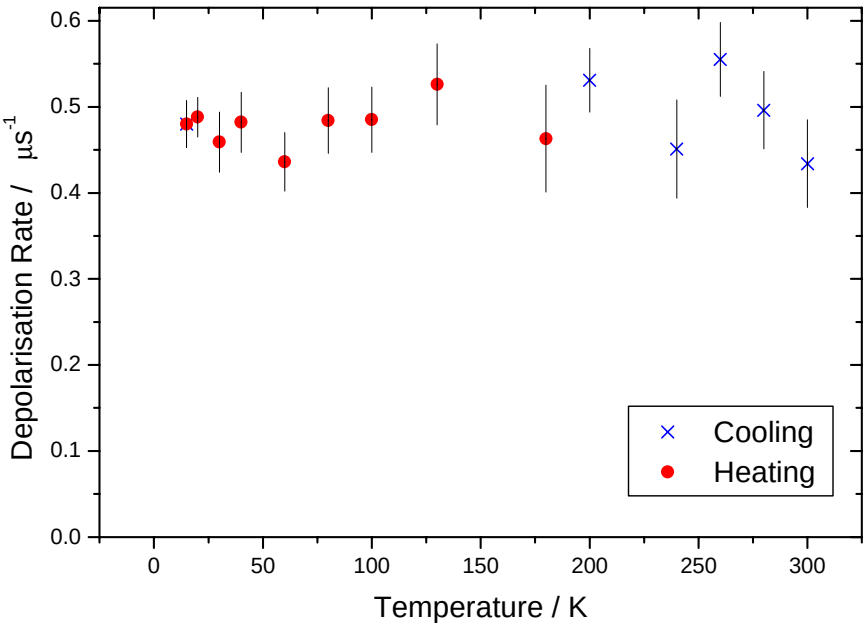

Figure 5.23: Fitted initial depolarisation of amorphous form of $ZrTi_2$ with a simple Gaussian.

In the case of the C-15 sample (Figure 5.21) we can see that up to a temperature of ~40 K the muon is static, showing an average depolarisation rate of 0.3 μs^{-1} and motional narrowing only sets in at temperatures greater than ~150 K. Similarly for the f.c.c. case (Figure 5.22) we see that the muons are essentially static up to a temperature of ~275 K, above which long-range diffusion sets in. The amorphous sample did not exhibit any (or very little) depolarisation over the temperature range measured (see Figure 5.23). This was mainly due to the limited experimental points available, resulting in poor statistics for a limited temperature range.

In order to extract quantitative information on the diffusion it is necessary to fit the data to the correct form of the Kubo-Toyabe function as described in the previous section. A fit of the C-15 $ZrTi_2H_{3.6}$ data obtained at three different temperatures to the dynamic Kubo-Toyabe function can be seen in Figure 5.25.

For each sample a simultaneous fit was performed for the low temperature data, from this values of Δ and τ_c were obtained. In Figure 5.24 the fitted values for the correlation time τ_c are shown for the fcc sample as a function of inverse temperature. An activation is extracted from the high temperature region and is indicated by the solid line.

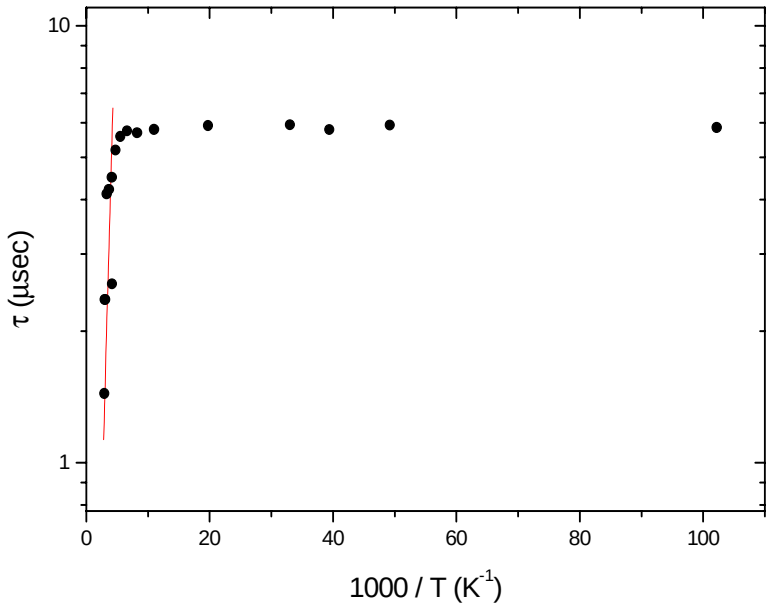

Figure 5.24: Fitted correlation times τ_c of muon diffusion in face-centred phase of $ZrTi_2H_{5.4}$.

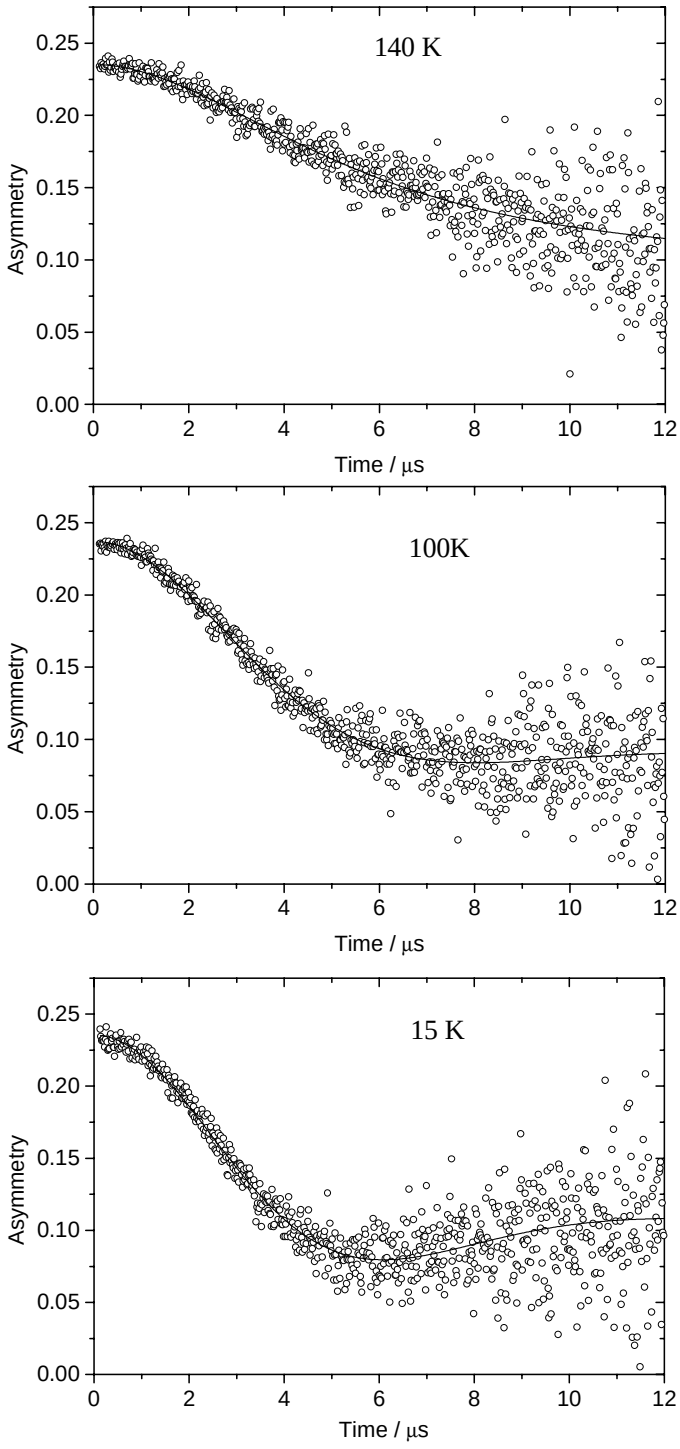

Figure 5.25: Fits to the C-15 $ZrTi_2H_{3.6}$ data using the dynamic Kubo-Toyabe function at three different temperatures.

A comparison of the correlation times obtained from this muon study with quasi-elastic neutron scattering (Fernandez *et al.*, 1997) and NMR (Skripov *et al.*, 19) measurements is shown in Figure 5.26 for the C-15 sample.

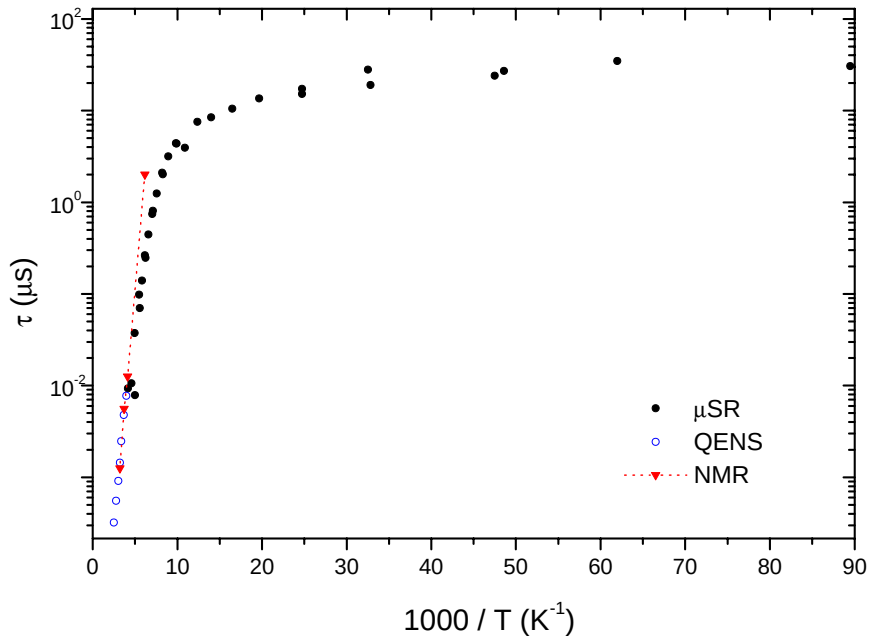

Figure 5.26: A comparison of correlation times, τ_c, of μ^+ diffusion (λ) and H diffusion as determined by QENS (O) and NMR (τ) for C-15 $ZrTi_2H_{3.6}$.

Table 5.8: Activation energies obtained from high temperature region of Figure 5.24 and Figure 5.26.

Sample	*Activation Energy (eV)*
C-15	0.159 ± 0.024
face-centred	0.102 ± 0.009

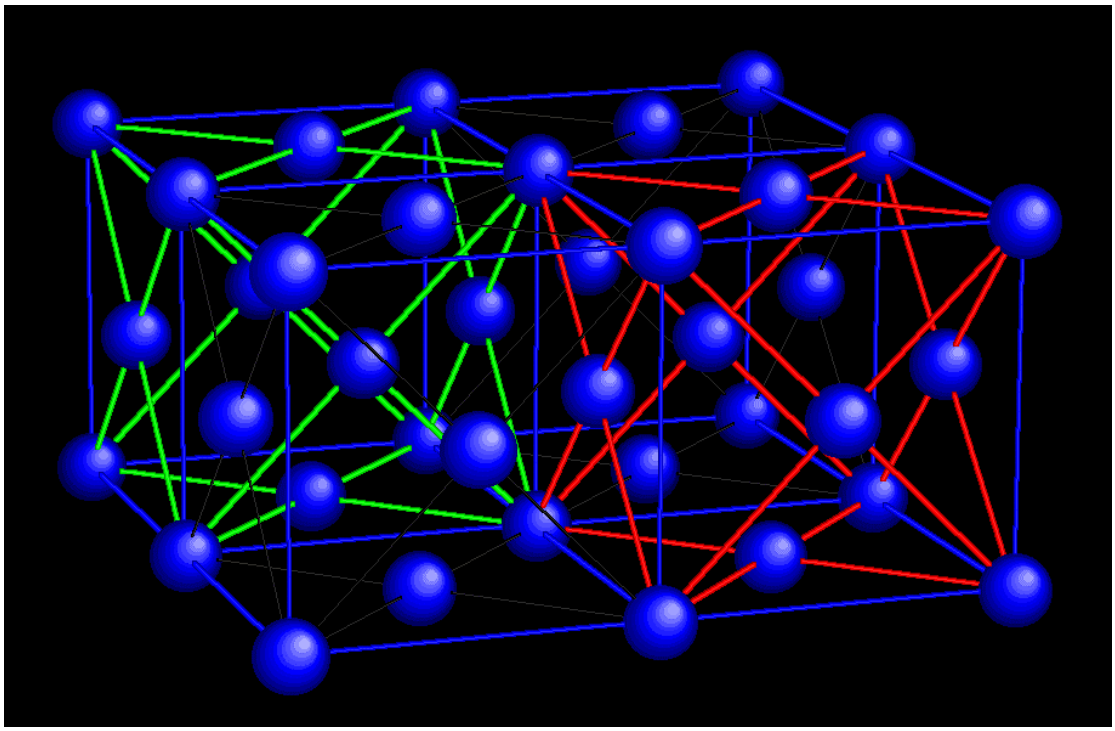

Figure 5.27: The fcc arrangement of e-sites (1A-3B) in a C-15 Laves Phase compound.

The value obtained for the second moment at low temperatures may be used to estimate the distance between occupied sites.

The zero field second moment is related to the so called Van Vleck value by the expression (Abragam 1970);

$$\Delta_{ZF}^2 = \frac{5}{2}\sigma_{VV}^2 \qquad (5.9)$$

For the case of unlike spins the so-called Van Vleck expression is

$$\sigma_{IS}^2 = \frac{1}{2}\gamma_I^2\gamma_S^2\hbar^2 S(S+1)\sum_k \frac{\left(1-3\cos^2\theta_{jk}\right)^2}{r_{jk}^6} \qquad (5.10)$$

where θ is the angle between hydrogen sites and a given arbitrary direction, r_{jk} is the distance between hydrogen sites. The second nearest neighbours are not included as they are so small as to be negligible.

Considering the C-15 sample, low temperature measurements give a value for Δ_{EXPT} = 0.293 μs^{-1}. If we take the lattice parameter to be 8.16 Å, then this gives us a nearest neighbour distance of 2.88 Å. This is assuming that the e-sites sit on a fcc sublattice (as in Figure 5.27), which also means that the $\left(1-3\cos^2\theta_{jk}\right)^2$ term in (5.10) has a value of 10.5. By using this information we can calculate a theoretical value for the second moment based, which turns out to be Δ_{CALC} = 0.253 μs^{-1}. Similarly, if we use the experimental value of Δ_{EXPT} then we can work backwards to arrive at an average muon-hydrogen separation of $r_{\mu\text{-}H}$ = 2.758 Å which compares well with the ideal value of 2.88 Å. From this it is reasonable to say that it is indeed the e-site that is occupied for $ZrTi_2H_{3.6}$.

5.6.4 $HfV_2H_{0.15}$ Results and Discussion

The results obtained from fitting the initial depolarisation to a Gaussian function as before can be seen in Figure 5.28. These results indicate that there may be some hysteresis present, which agrees with previous measurements on the same

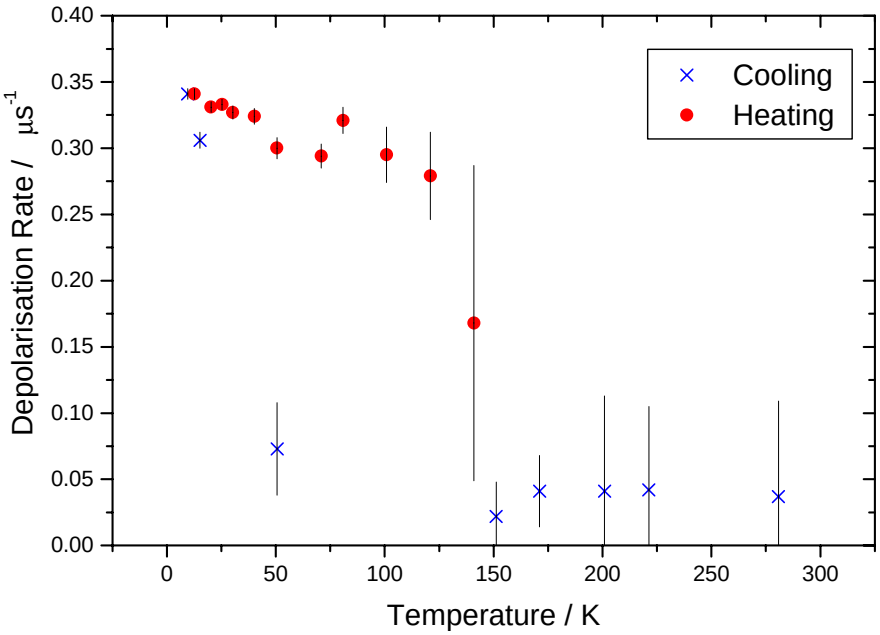

Figure 5.28: Fitted initial depolarisation of $HfV_2H_{0.15}$ with a simple Gaussian function

compound (Kemali *et al.*, 1995). The spectra were measured for the same temperature, but one was measured during cooling and the other during heating. These can be seen in Figure 5.29.

The data were subsequently fitted using the strong collision version of the Kubo-Toyabe function in a similar manner to the fitting of the $ZrTi_2H_x$ data that was described previously. In a similar method to that described in the previous section, a value for the muon-hydrogen separation was extracted from the low temperature measurement of the second moment. The value for $r_{\mu\text{-}H}$ = 1.633 Å was obtained, this compares well with nearest neighbour distances between g-sites of either 1.14 Å or 1.3 Å. The correlation times that were obtained compare well with the values extracted for H diffusion from the quasi-elastic neutron scattering measurement described earlier (see Figure 5.30). One thing that may be surmised from the μSR is that the measurements performed did not cover a high enough temperature range in order to extract a value for the activation energy, but this was due to the fact that the μ^+ is moving too rapidly to measure its depolarisation.

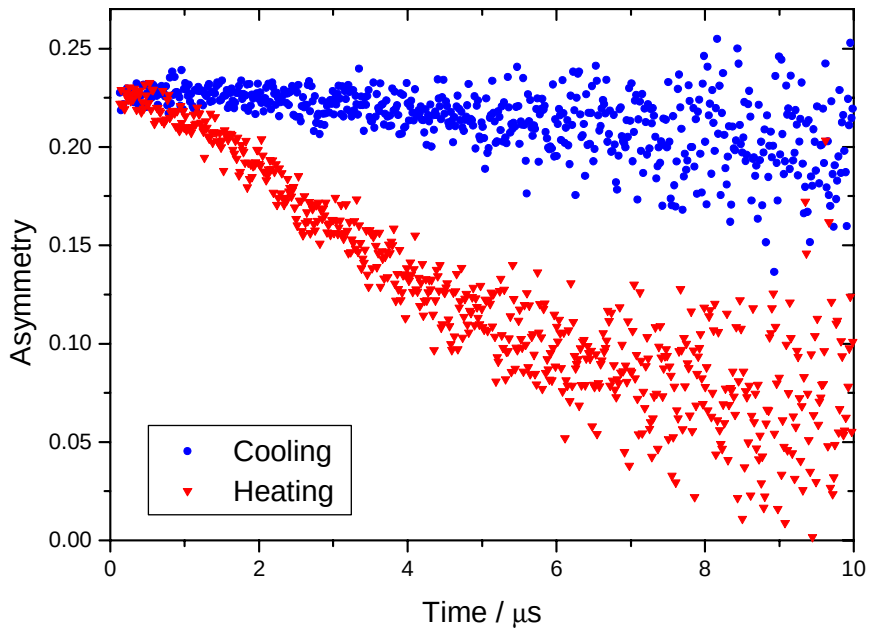

Figure 5.29: Data measured at a temperature of 50K for $HfV_2H_{0.15}$ during both cooling (λ) and heating (τ).

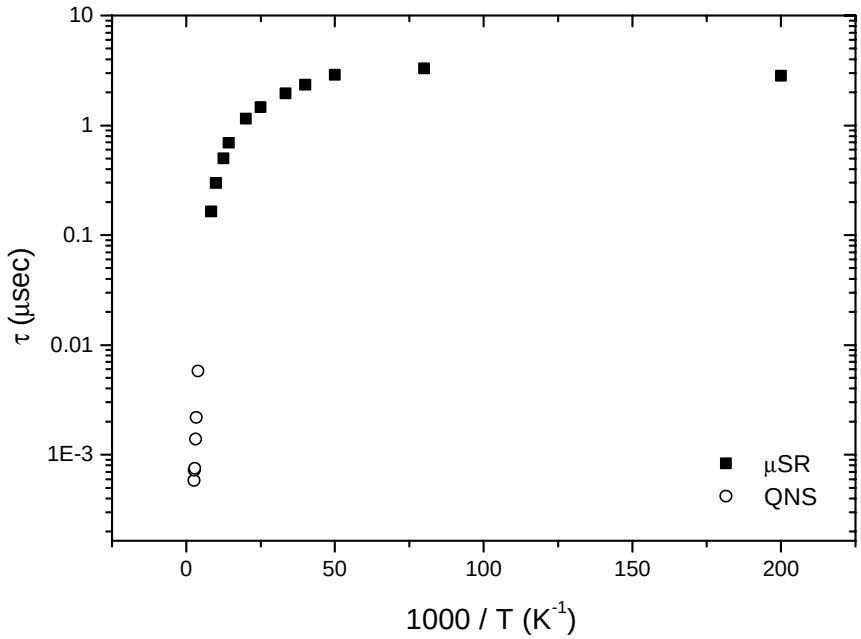

Figure 5.30: A comparison of correlation times, τ_c, of μ^+ diffusion (v) and H diffusion as determined by QENS (O) for HfV_2H_x.

5.7 Inelastic neutron scattering measurements of $TiCr_{1.85}H_{0.45}$.

Using the TFXA spectrometer at ISIS (c.f. § 4.X) an inelastic neutron spectra was recorded for a single concentration, $TiCr_{1.85}H_{0.45}$ at low temperature (T<15 K). This data can be seen in Figure 5.31. The data was collected over a period of twelve hours in order to obtain good statistics. The measurement was made at low temperature in order to reduce the effect of the Debye-Waller factor. The raw data were converted from time-of-flight into S(Q,ω) for use in the data analysis, by using the standard instrument routines. The spectrum was fitted with a number of Gaussian peaks using a standard package. In addition to the inelastic spectrum, TFXA also gives a diffraction pattern of the sample under investigation. This showed that the sample was in the C-15 phase with a lattice parameter of 6.998 Å. A very simple analysis of the data has been performed (Figure 5.32). The widths of the peaks were determined by the instrumental resolution, and a sensible number of Gaussian peaks were used to describe the data well. It should be noted that this data

has been used by another author to determine the parameters for a Born-Mayer interatomic potential for this system (Fernandez *et al.*, 1998).

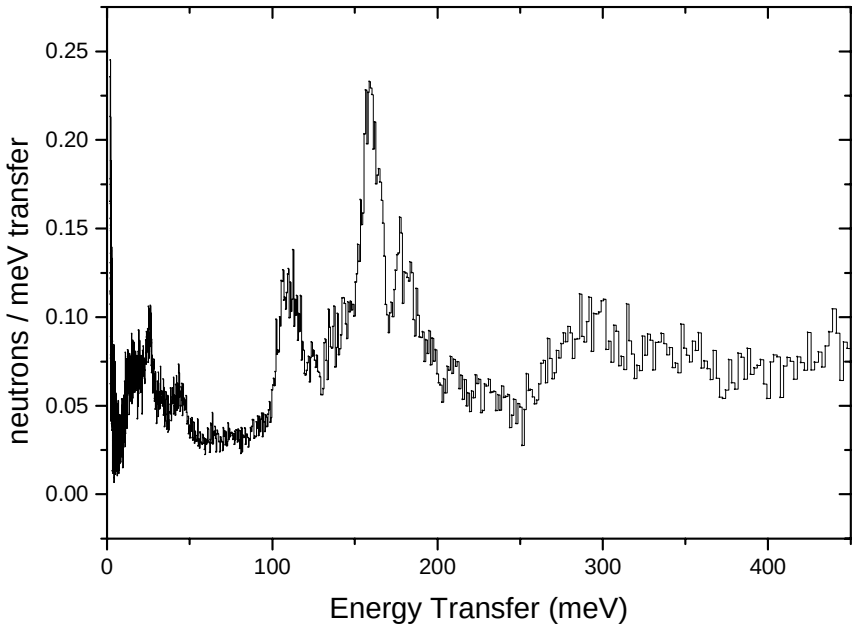

Figure 5.31: Full spectra of $TiCr_{1.85}H_{0.45}$ measured on TFXA.

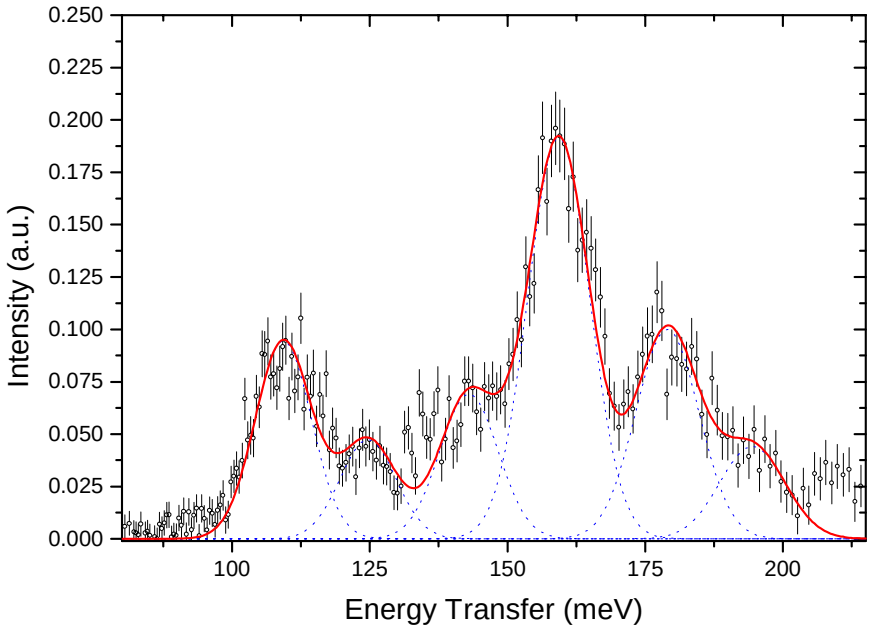

Figure 5.32: Inelastic spectrum of $TiCr_{1.85}H_{0.43}$ measured on TFXA. A fit to the data using six Gaussian peaks is also shown. The extra peak on the right hand side of the spectrum (~220 meV) is assumed to be the second harmonic of the leftmost peak.

Table 5.9: Basic description of peak centres and areas for each of the Gaussian fits shown in Figure 5.32.

Peak Centre (meV)	*Area % Total*
109.3	16.1 %
124.8	8.1 %
142.9	12.2 %
159.2	35.8 %
179.1	19.1 %
194.3	8.7 %

5.8 Overall Conclusion and Further Work

Quasi-elastic and inelastic neutron scattering measurements have been performed for the C-15 Laves compound, $TiCr_{1.85}H_{0.43}$. The activation energy of 0.237 eV that was obtained compares well with a value obtained by NMR (Bowman *et al.* 1983) of 0.19 eV. We have shown how the experimentally obtained jump length can be attributed to a physical distance within the C-15 structure. It would be useful to measure the lattice parameter as a function of temperature (especially over the range covered by the QENS experiment) to gain an insight into the origin of the observed change in jump length. As a follow up study, it would be interesting to measure the quasi-elastic scattering as a function of hydrogen concentration. The temperature to make measurements over should extend below those used here, so that we can investigate the transition (if present) from jump diffusion between hexagons to localised motion around the ring. It is impossible to confidently determine which peaks in the inelastic spectrum arise from particular sites.

MuSR measurements on $ZrTi_2H_x$ have been made on three different forms of this compound. For the C-15 form, the calculated values of the second moment and the muon-hydrogen separation compare very well with experimental values. Therefore it reasonable to conclude that it is indeed the e-site that is preferentially occupied for this phase. The measurements made on the amorphous sample are not comprehensive enough for any definite conclusion to be drawn.

The activation energy and jump length obtained from quasi-elastic neutron scattering measurements for $HfV_2H_{0.3}$ show a good agreement with those previously measured at higher hydrogen concentrations. Zero field muon spectroscopy measurements indicate that there is some hysteresis effects present. This is likely due to a structural phase change of the sample which is corroborated by neutron diffraction measurements that indicate that there is a change of phase in the relevant temperature range.

Incoherent inelastic neutron scattering measurement of $TiCr_{1.85}H_{0.43}$ was performed for a single low temperature. It is difficult to extract any information on the site occupancies from this spectrum. As a further study, measurements should be made as a function of hydrogen concentration, so that the evolution of each peak can be observed.

Chapter 6

Conclusions & Final Remarks

6.1 Summary of Osiris

A Monte Carlo program has been developed to simulate an entire inverted geometry spectrometer. The use of Monte Carlo in instrumental design is being more widely used as design projects for the next generation of neutron sources and instrumentation are progressing all over the world. It is much more sensible to make mistakes 'inside' a computer rather than finding them once the spectrometer has been built, therefore saving a lot of expense. A number of aspects and experiences that have been obtained during the course of the instrumental design and simulation are now being inputted into an international collaboration into a co-operative effort to produce a "standardised" Monte Carlo code for instrumental design (for an overview see Crawford; 1997).

The incident beam polarising benders have been optimised to the given geometry of the neutron guide. Various problems that arose during the construction and commissioning could be evaluated and a solution arrived at with the aid of Monte Carlo simulations.

A study of the factors that contribute to the final resolution of an inverted geometry time-of-flight spectrometer was also performed. This revealed a number of key points. Firstly, the main contributions to the resolution are the uncertainties in the time from the moderator and in the d-spacing of the analyser. It was also found that the sample size (height) has very little effect on the final result. One surprising fact that emerged was that the height of the crystal analyser bank was not a significant contribution to the degradation of the resolution.

The design of the neutron spin analysers for the scattered beam will need careful consideration. A decision will have to be made whether to use supermirror benders (as in the incident beam polarisers) or to opt for something like a He^3 filter. The benefit of the filter would be that the whole beam area could be polarised with a single cell, whereas for the case of an optical polariser, there are technological difficulties in filling the required volume adequately.

Once the proposed inelastic analyser has been installed together with its full polarisation analysis components, there will still be half the sample tank vacant, leaving room for future developments. It may provide an opportunity to explore the possibilities of building a pulsed source spin echo machine. Although, it must be pointed out that there are problems in achieving the guide fields that would be necessary.

In polarisation analysis experiments the corrections for multiple scattering become more critical. It must be stressed that in order to extract the correct and relevant results a suitable computer program needs to be developed, most likely employing Monte Carlo techniques to provide an estimation of the contribution due to multiple scattering.

As a result of the work described here, there now exists a machine for measuring the reflectivity of large samples by employing the technique of measuring the multireflectivity. This instrument MITED has mainly be used to measure the reflectivity of a number of guide sections that have been used in the construction of the OSIRIS neutron guide. It can be moved into position quite quickly and easily and occupies a parasitic position on the IRIS beamline and may be operated independently of IRIS.

6.2 C-15 Laves Phase Compounds

Quasi-elastic neutron scattering measurements (QENS) have been made on $TiCr_{1.85}H_{0.43}$ and a value for the activation energy and effective jump length have been extracted from the measured broadenings. The value of the activation energy was

found to be in general agreement with previous NMR measurements. The jump length has been described in terms of the distances between g-site hexagons and it appears that at higher temperatures we start to see a jumping motion between next nearest neighbour hexagons. Additional measurements would be useful to look more closely at how the diffusive motion varies with temperature and hydrogen content. From the INS measurement performed it is difficult to elucidate from which sites the observed peaks originate. Another experiment needs to be performed to measure the inelastic spectrum as a function of hydrogen content. This experiment has already been proposed and accepted using the TOSCA spectrometer at ISIS.

Measurement of the muon diffusion has been conducted for three different phases of $ZrTi_2H_x$ (x=3.6,5.4), C-15, face-centred tetragonal and amorphous. Instrumental problems cut short the amorphous sample measurements so little useful information can be deduced. For the fcc sample a value for the muon-hydrogen separation was obtained, but further structural work is required before a definite conclusion about the site occupancy can be made. The data collected for the C-15 sample yielded the most conclusive results. The agreement between the measured and calculated value for the 'second moment' was good. The muon-hydrogen separation extracted from the data gave a value close to that of nearest neighbour e-sites. It is relatively clear that it is indeed the e-sites that are preferentially occupied in this system.

For the HfV_2H_x (x=0.15, 0.3) sample QENS, MuSR and neutron diffraction measurement techniques have been used. Due to experimental problems the data collected is not complete. From the quasi-elastic data we have again extracted values for the activation energy and jump length which are in good agreement with values obtained at higher concentrations. It is unclear why we get such good agreement when at the higher concentration we have an extra site that is occupied (Westlake, 1983).

The experiments performed in this thesis are part of an ongoing project to characterise the behaviour of the C-15 Laves Phase family of compounds (e.g. Stonadge, 1992). Several experiments have been proposed and accepted to continue the work presented here on these materials.

Publications

Proc. Int. Symposium on Neutron Optics and Related Research Facilities, Kumatori, 1996
J. Phys. Soc. Jpn. 65 (1996) Suppl. A pp. 245–248

The Osiris Polarisation Analysis Spectrometer and Diffractometer

D. Martín, *S. Campbell and C. J. Carlile

ISIS Pulsed Source, Rutherford Appleton Laboratory, Chilton, Didcot, UK
**Department of Pure and Applied Physics, University of Salford, Salford, UK*

(Received 6 March 1996; accepted 21 March 1996)

The Osiris Project will explore the possibilities for cold neutrons on pulsed sources using a versatile approach that will allow structural and dynamical studies of condensed matter by several methods ranging from unpolarised neutron scattering to full polarisation analysis. The instrument is situated at the end of a supermirror guide with a final converging section. The first options to be implemented are a large powder diffraction detector in near backscattering geometry and a multiple crystal analyser with its corresponding detectors in inverted geometry. Monte Carlo simulations of the neutron guide will be presented.

KEYWORDS: Neutron Instrumentation, Computer Simulations, Polarised Neutrons.

ELSEVIER

Physica B 241–243 (1998) 326–328

PHYSICA B

A quasi-elastic neutron-scattering study of hydrogen diffusion in C15 Laves-phase compounds $HfV_2H_{0.1}$

S.I. Campbell*, M. Kemali, D.K. Ross

Joule Laboratory, Department of Physics, University of Salford, Salford, M5 4WT, UK

Abstract

Recently, the AB_2 C15 Laves-phase compounds have been of interest for metal hydride batteries due to their ability to absorb large amounts of hydrogen. Quasi-elastic neutron-scattering measurements were performed on the C15 Laves-phase compounds $HfV_2H_{0.1}$ using the IN10 spectrometer at the ILL, Grenoble, France. Quasi-elastic broadening was measured for momentum transfers between 0.27 and 1.96 $Å^{-1}$ in the temperature range 250–380 K. The activation energy obtained from this data is discussed and compared to previous QENS measurements on the same compound for high hydrogen concentration. © 1998 Elsevier Science B.V. All rights reserved.

Keywords: Laves-phase compounds; Quasi-elastic neutron scattering; Hydrogen; Diffusion

ELSEVIER

Physica B 234–236 (1997) 925–927

PHYSICA B

A study of the tetragonal to ortho 1 phase transition in $YBa_2Cu_3O_x$

M. Mercer[a,*], S.I. Campbell[a], S.M. Bennington[b], J.W. Dreyer[b], M. Kemali[a], P.D. Shepherd[a], D.K. Ross[a]

[a] *Department of Physics, Joule Laboratory, University of Salford, Salford, M5 4WT, UK*
[b] *ISIS Facility, Rutherford Appelton Laboratory, Chilton, Didcot, Oxon, OX11 0QX, UK*

Abstract

In situ measurements were performed on a high purity sample on the high-resolution powder diffractometer (HRPD) at ISIS, UK, allowing the oxygen partial pressure and temperature to be controlled. The tetragonal to orthorhombic phase transition was observed. The results are discussed and compared with parallel isothermal thermogravimetric measurements of the phase diagram.

Keywords: Powder diffraction; High-T_c superconductors; Phase transition

ELSEVIER

Physica B 234–236 (1997) 914–916

PHYSICA B

Water dynamics in Na zeolite P by QENS

P.D. Shepherd[a,*], W.W. Kagunya[b], S.I. Campbell[a], A.P. Chapple[c], J.W. Dreyer[b], R.J. Humphreys[b], M. Kemali[a], M. Mercer[a], D.K. Ross[a]

[a] *Department of Physics, Joule Laboratory, University of Salford, M5 4WT, UK*
[b] *ISIS Facility, Rutherford Appleton Laboratory, Didcot, OXON, OX11 0QX, UK*
[c] *Unilever Research, Port Sunlight Laboratories, Cheshire L63 3JW, UK*

Abstract

Quasi-elastic neutron-scattering (QENS) measurements have been made using the IRIS spectrometer (ISIS, UK) on water in synthetic Na zeolite P. The quasi-elastic broadening observed is assigned to a rotation of the water molecules.

Keywords: Quasi-elastic scattering; Water; Zeolites

ELSEVIER

Physica B 248 (1998) 152–156

PHYSICA B

X-Ray and neutron reflectivity investigations of Co/Cu multilayers

D.E. Joyce*, S.I. Campbell, P.R.T. Pugh, P.J. Grundy

Joule Laboratory, Department of Physics, University of Salford, Salford M5 4WT, UK

Abstract

We have studied the effect of low-energy ion beam etching of silicon (1 0 0) substrates on the magneto-transport and structural properties of sputter deposited cobalt/copper multilayers. The films had a nominal structure of 16*{1 nm Co/2.1 nm Cu} + 1 nm Pt placing them on the second peak of the oscillatory coupling curve. We show that, as the etching energy is increased from 0 to 1500 eV, the giant magnetoresistance (GMR) decreases from about 19% to about 1%. This is attributed to subtle changes in the film microstructure causing the destruction of antiferromagnetic coupling between the magnetic layers. We present reflectivity and X-ray diffraction data which suggest that Fermi surface effects in the bulk drive the changes in GMR. However, we conclude that spin-dependent scattering at the interfaces may yet be a significant factor and suggest that the interfacial structure be examined more closely using diffuse reflectivity techniques. © 1998 Elsevier Science B.V. All rights reserved.

Keywords: GMR; Multilayers; Reflectivity

Appendix I

Description of Surfaces within Monte Carlo Simulations.

Each individual surface of the neutron guide has to have its area defined by an equation of the form

$$Ax^2 + Bx + Cy^2 + Dy + Ez^2 + Fz + G + Pxy + Qyz + Rxz = 0$$

where A, B, C, D, E, F, G, P, Q and R are constants for each individual surface.

If the left hand side of the above equation is positive for a point lying in the n^{th} region a parameter is set equal to +1, whereas if the LHS is negative then this parameter is set equal to -1, from this we can tell by looking at these parameter values which side of the surface is the interior of the guide and which is the exterior. This is important if we wish to know if a particular neutron lies within a given section of guide (Johnson, 1980).

Appendix II

Photographs of OSIRIS

In this section a number of photographs that were taken during the construction of the OSIRIS spectrometer are shown.

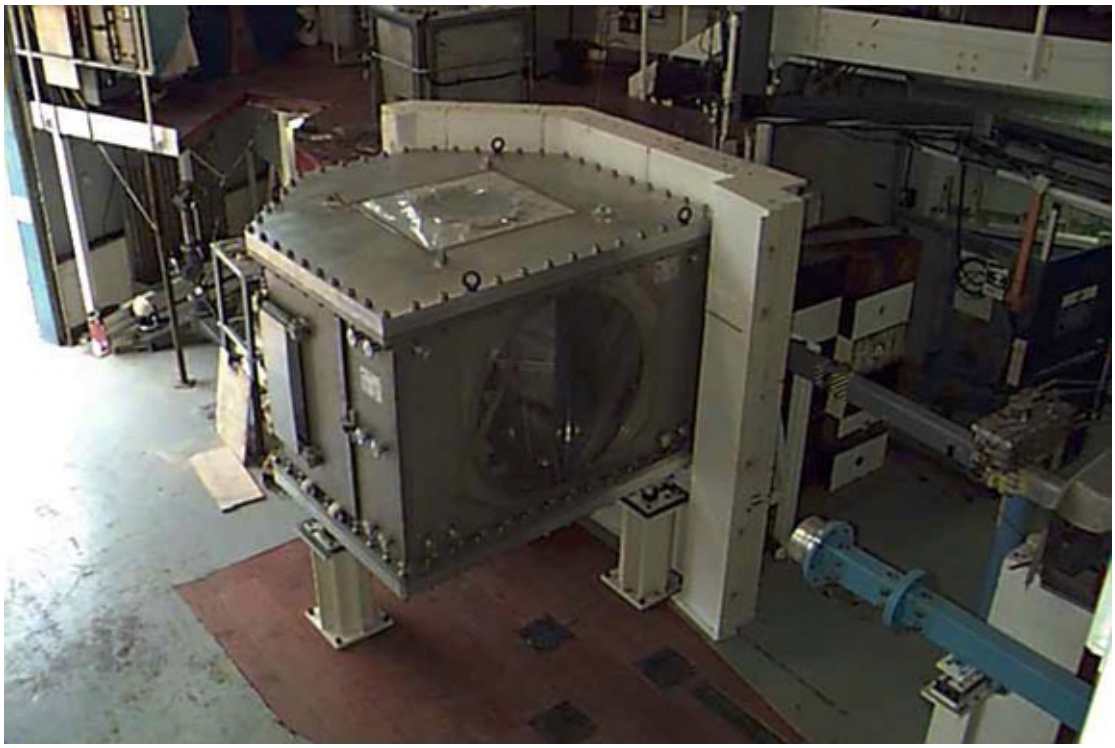

Figure 1: Sample tank in position, with blockhouse under construction. To the bottom right we can see both the OSIRIS and IRIS neutron guides.

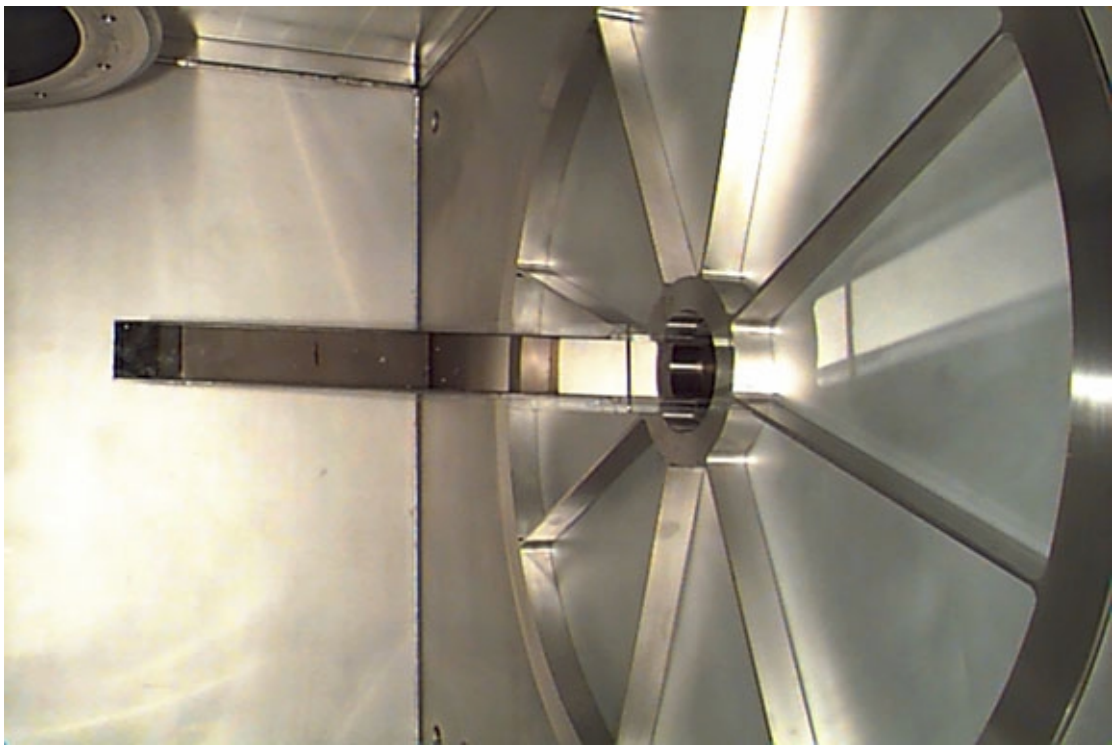

Figure 2: View of the converging guide section from inside the sample tank. The eight windows behind which sit the diffraction detector modules.

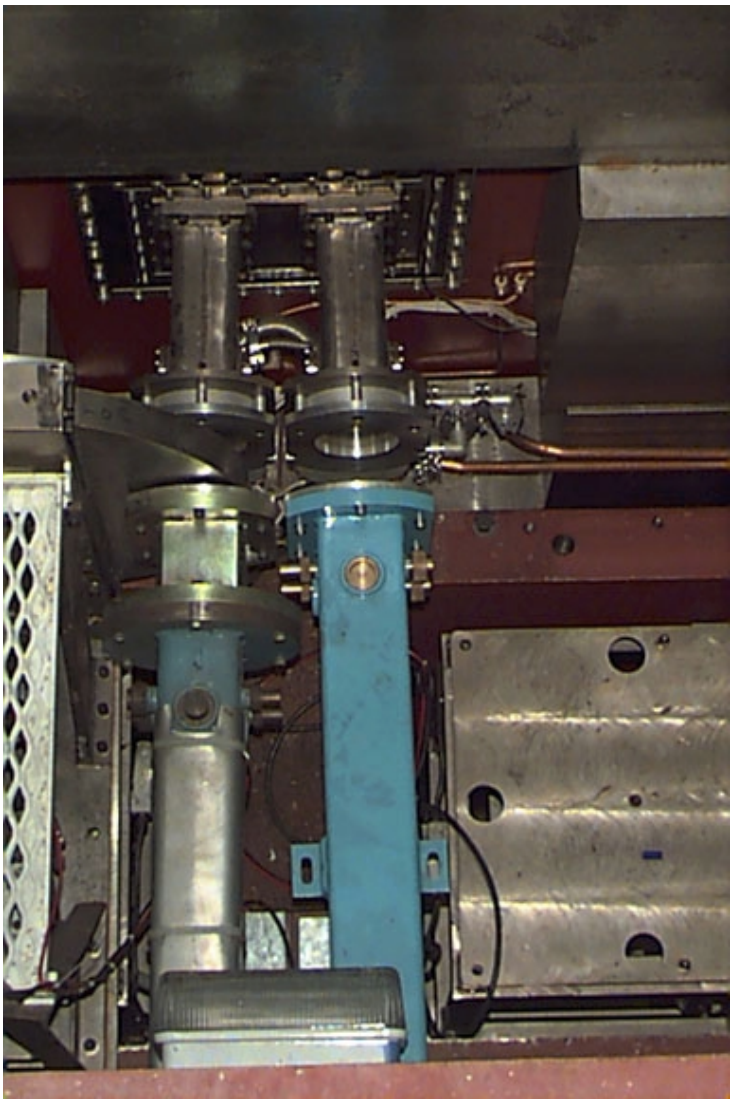

Figure 3: A view of the two neutron guides emerging from the target station, the OSIRIS guide is the one on the right hand side. The IRIS guide is shown complete with its disc chopper.

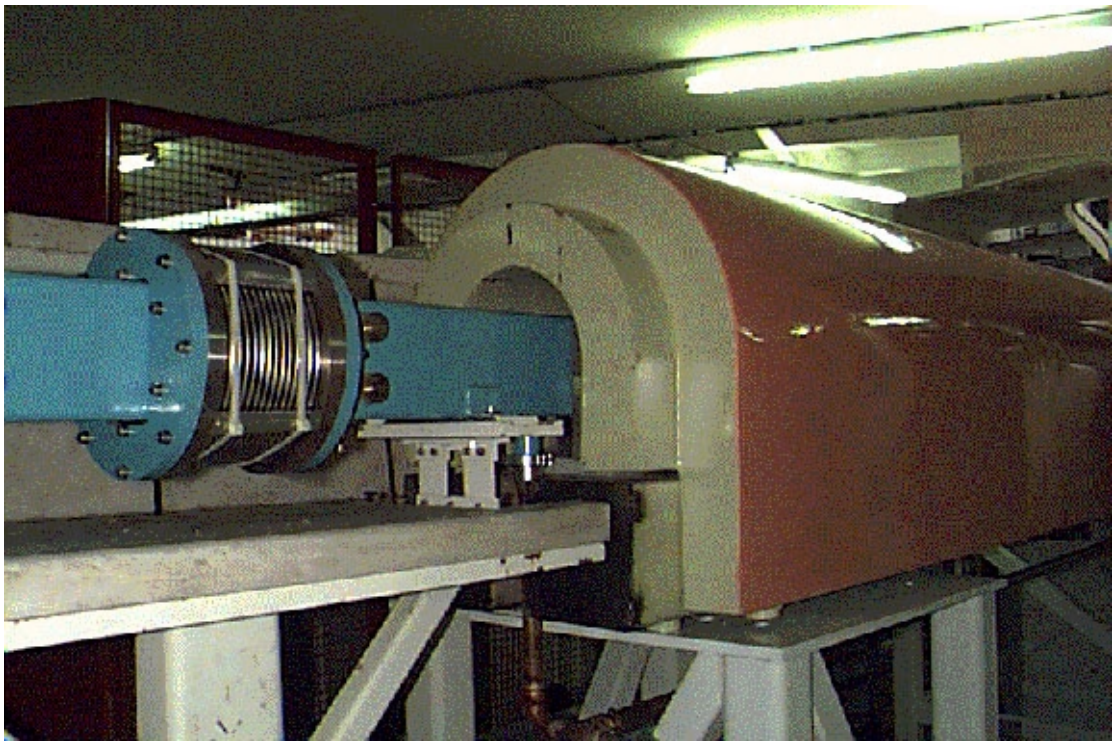

Figure 4: The OSIRIS neutron guide complete with shielding. Also shown are the bellows that are inserted between guide sections (blue), these give flexibility to the vacuum vessel during alignment.

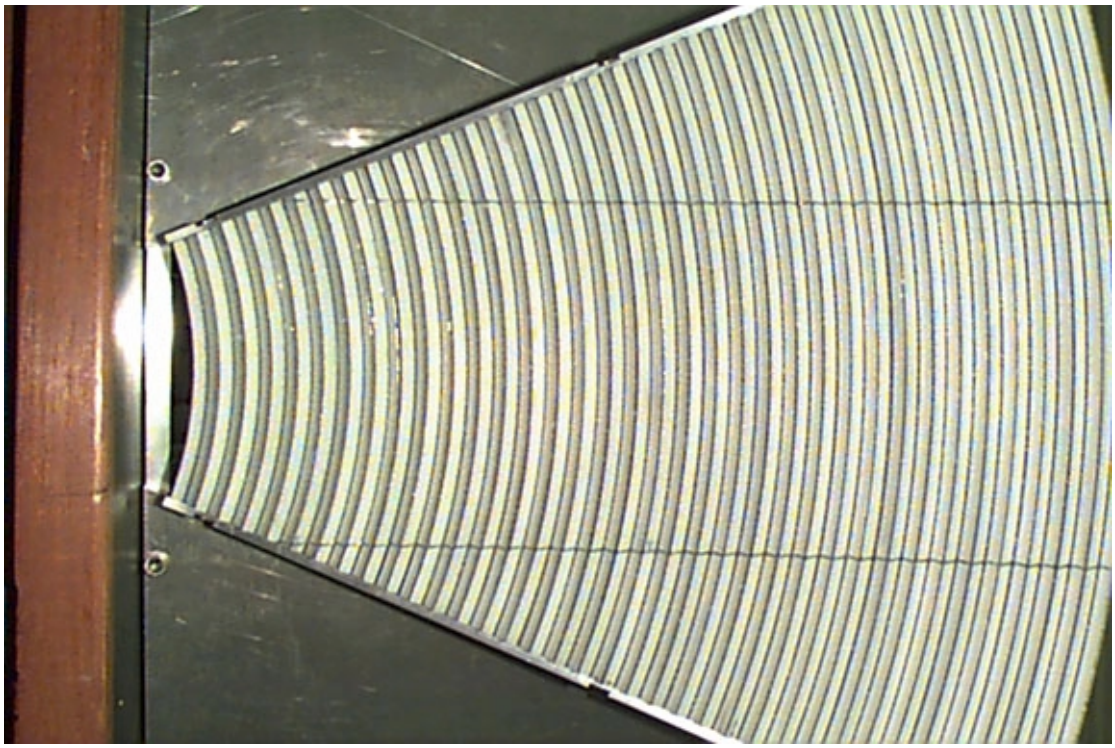

Figure 5: The active area of the first installed diffraction module as seen from the sample position.

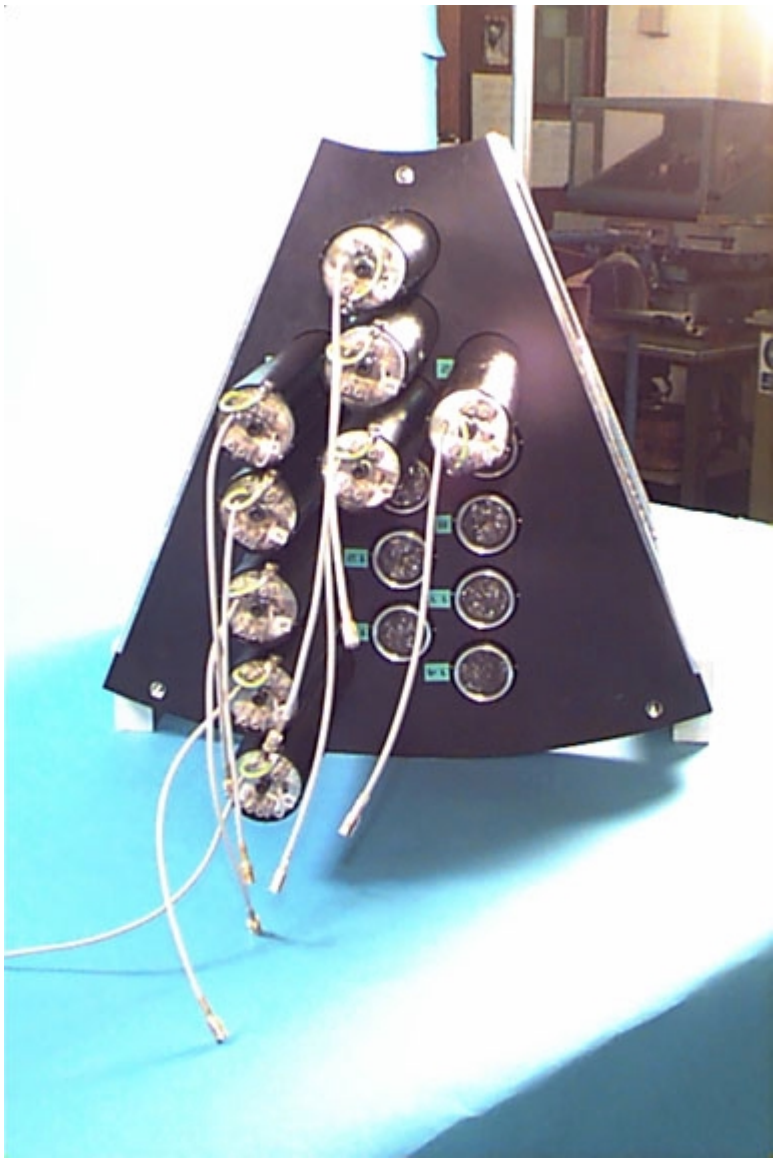

Figure 6: A view of the photomultiplier tubes on the back of a module for the diffraction detector.

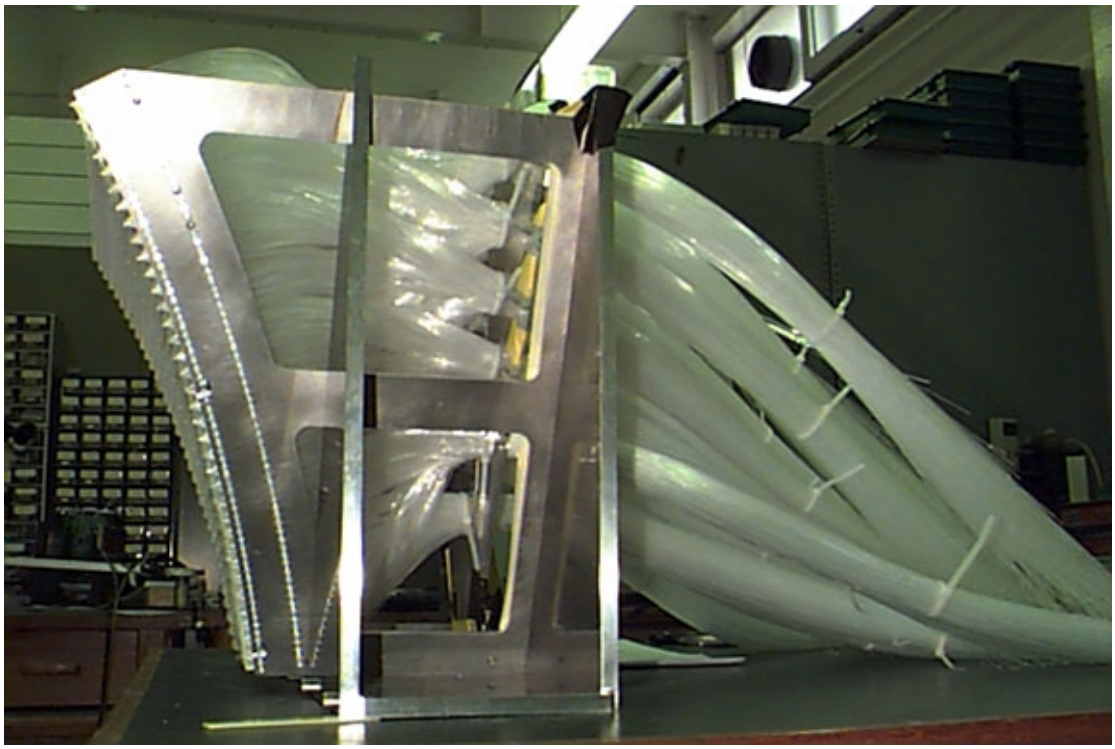

Figure 7: A diffraction module complete with its fibre optic cables.

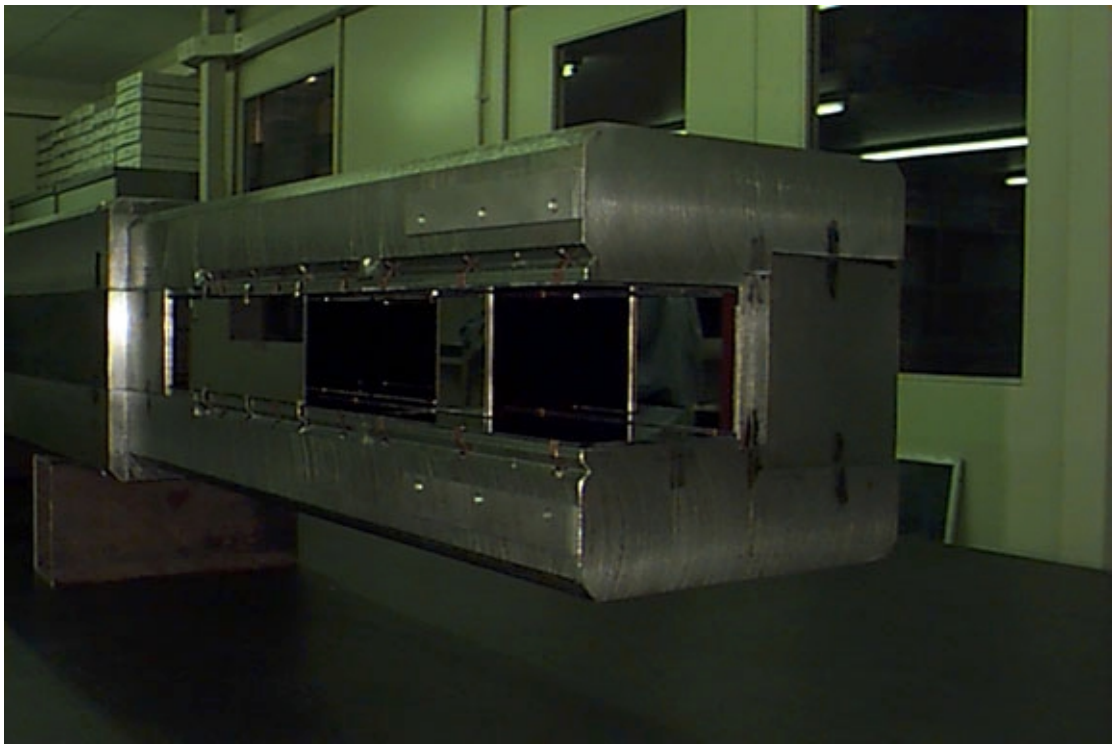

Figure 8: The shutter guide section. It consists of a steel outer case with thin supermirror coated glass sections inserted along the interior surfaces.

Appendix III

Serial Numbers for Glass Sections Measured in Section 4.8.2

Glass Section Number	*Serial Number*
1	R2473
2	R2469
3	R2307 (15b)
4	R2307 (15a)
5	R2463 (9-1)
6	R2463 (10-1)
7	R2463 (10-2)
8	R2463 (8-1)
9	R2462 (2-2)
10	R2462 (14-1)
11	R2466 (B3)
12	R2475 (B4)

References

Abragam, A. (1970), *The Principles of Nuclear Magnetism*, Clarendon Press, Oxford.

Andersen, K. H. (1996), *Nucl. Instr. & Meth. in Phys. Res. A*, 371 472-479.

Anderson, I. S., Bonnet, J. E., Heidemann, A., Ross, D. K., Wilson, S. K. P. (1984), *J. Less-Comm. Met.*, 101 405.

Anderson, I. S. (1992), *SPIE*, 1738 pp. 118-129.

Bacon, G. E. (1962), *Neutron Diffraction*, Clarendon Press, Oxford.

Balchin, J. J. P. (1996), *Rutherford Appleton Laboratory Technical Report*, RAL-TR-96-030.

Ballot, B., Menelle, A., Al Usta, K., Farnoux B. & Samuel, F. (1993), *Journal de Physique IV*, Colloque C8, 3 471-474

Ballot, B., Menelle, A., Samuel, F., Al Usta, K. & Farnoux, B. (1994a), *Physica B*, 198 213-216

Ballot, B., Samuel, F. and Farnoux, B. (1994b), *Physica B*, 198 220-223.

Bée, M. (1988), *Quasielastic Neutron Scattering*, Adam Hilger, Bristol.

Blaesser, G. and Peretti J. (1968), *Proc. Int. Conf. Vacancies and Interstitials in Metals* (KFA, Julich), EDITOR: Seeger, A. *et al*, 2 836.

Blank, H. and Maier, B. (EDITORS) (1988), *"Guide to Neutron Research Facilities at the ILL"*.

Boland, B. and Whapham, S. (EDITORS) (1992), *The ISIS User Guide.*

Böni, P. (1997), *Physica B*, 234-236 1038-1043.

Böni, P., Clemens, D., Grimmer, H. and Van Swygenhoven, H. (1995), ICANS-XIII.

Bowman Jr., R. C., Craft, B. D., Attalla, A., Johnson, J. R. (1983), *Int. J. Hydrogen Energy* 8 801.

Bull, D. J. (1998), *Private Communication.*

Campbell, S. I. (1998), *RAL Report (in preparation).*

Campbell, S. I., Kemali, M., Ross, D. K. (1998), *Physica B*, 241-243 326-328.

Carlile, C. J., Hey, P. D. and Mack, B. (1976), ILL Report, ILL-76-179.

Carlile, C. J., Johnson, M. W. and Williams, W. G. (1979*), Neutron Guides on*

Pulsed Sources, RL-79-084.

Carlile, C. J. and Adams, M. A. (1992), *Physica B*, 182 431-440.

Carlile, C. J., Adams, M.A., Krishna, P. S. R., Prager, M., Shibata, K. and Westerhuijs, P. (1994), *Nucl. Instr. & Meth. in Phys. Res. A*, 338 78-82.

Carlile, C. J. (1996), *Private Communication*.

Chudley, C. T. and Elliot, R. J. (1961), *Proc. Phys. Soc.*, 77 353.

Cook, J. C. (1990), *Ph.D. Thesis*, Birmingham University.

Cook, J. C. (1993), *ILL Report*, 93CO01G.

Cooper, M. J. and Nathans, R. (1966), *Acta Cryst.*, 23 357.

Copley, J. R. D. (1993), *J. of Neutron Research*, 1 (2) 21-36

Crawford, R. K. (1997), *Workshop on Monte Carlo Simulation of Neutron Scattering Instruments*, 13-14 November, Argonne National Laboratory, USA. Technical Note ANL/SNS/97-2

Crevecoeur, R., de Schepper, I., de Graaf, L., Montfrooij, W., Svensson, E. and Carlile, C. (1995) *Nucl. Instrum. Meth A*, 356 415-421.

Daemen, L. L., (1997), *Private Communication*.

Darwin, C. G. (1914a), *Phil. Mag.*, 27 315.

Darwin, C. G. (1914b), *Phil. Mag*., 27 675.

Doubble, R. (1997), *Private Communication*.

D. Dubbers, D. (1994), *Nucl. Instr. & Meth.* A354 N^{o} 2-3, pp. 598.

Elsenhans, O., Böni, P., Friedli, H. P., Grimmer, H., Buffat, P., Leifer, K., Söchtig, J. and Anderson, I. S. (1994), *Thin Solid Films*, 246 110-119.

Endoh, Y., Ikeda, S., Mitsuda, S. and Fujimoto, H. (1985), *Nucl. Instr. & Meth. in Phys. Res. A*, 240 115-121.

Faux, D. A. and Ross, D. K. (1987), *J. Phys. C*, 20 1441.

Fernandez, J. F. (1998), *Private Communication.*

Fernandez, J. F., Kemali, M., Johnson, M. R. and Ross, D. K. (1997a), *Physica B*, 234-236 903-905.

Fernandez, J. F., Kemali, M., Ross, D. K. (1997b), *J. Alloys and Compounds*, 253-254 248-251.

Fernandez, J. F., Kemali, M., Sanchez, C. and Ross, D. K. (1998), *to be published.*

Hahn, W. and Schweika W. (1997), *Physica B*, 234-236 1165-1167.

Hahn, W. (1997), *Private Communication*.

Havill, R. L., Titman, J. M., Wright, M. S. and Crouch, M. A. (1989), *Z. Phys. Chem. N.F.*, 164 1083-1088.

Hayano, R. S., Uemura, Y. J., Imazato, J., Nishida, N., Yamazaki, T. and Kubo, T. (1979), *Phys. Rev. B*, 20 (3) 850.

Hayter, J. B., Penfold, J. and Williams, W. G. (1978), *J. Phys. E: Sci. Instrum.*, 11 454-458.

Hayter, J. and Mook, H. (1989), *J. Appl. Cryst*., 22 35

Heidemann, A. and Anderson, I. (1983), *Workshop on Beam Definition Devices*, Jülich, June 9th & 10th.

Hempelmann, R., Richter, D., Hartmann, O., Karlsson, E., Wäppling, R. (1989), *J. Chem. Phys.*, 90 (3) 1935-1949.

Hjelm, R. P. ED (1996), *Proc. of a Workshop on Methods for Neutron Scattering Instrumentation Design*, Berkeley National Lab. Report N°. 9609353.

Howells, W. S. (1996), *Rutherford Appleton Laboratory Technical Report*, RAL-TR-96-006.

Ikeda, S. and Carpenter, J. M. (1985), *Nucl. Instr. & Meth. in Phys. Res. A*, 239, 536-544.

Inoue, K., Kanaya, T., Kiyanagi, Y., Shibata, K., Kaji, K., Ikeda, S., Iwasa, H. and Izumi, Y. (1993), *Nucl. Instr. & Meth. in Phys. Res. A*, 327 433-440.

Irodova, A. V., Glazkov, V. P., Somenkov, V. A. and Shil'shtein, S. Sh. (1980), *Sov. Phys. Solid State*, 22 45.

Jericha, E., Carlile, C. J., Rauch, H. (1996), *Nucl. Instr. & Meth. in Phys. Res. A*, 379 N°. 2, 330-334.

Johnson, J. R. (1980), *J. Less-Common Metals*, 73 345.

Johnson, M. W. (1980), *Rutherford Appleton Laboratory Report*, RL-80-065.

Kawabata, Y., Suzuki, M., Tsuruno, A. and Onishi, N. (1992), *Physica B*, 180&181, 987-990.

Kearley, G. J. and Trouw, F. (1993), *J. of Neutron Res.*, Vol. 1, N°. 3, 45-51.

Kemali, M., Havill, R. L., Titman, J. M., Ross, D. K. (1995a), *J. Alloys and Compounds*, 231 255-258.

Kemali, M., Stonadge, P. R., Ross, D. K., Bennington, S. M. (1995b), *J. Alloys and Compounds*, 231 259-261.

Kemali, M., Havill, R. L., Titman, J. M. (1995c), *Phil. Mag. B*, 72 (2) 275-284.

Kemali, M., Buckley, C. E., Havill, R. L., Ross, D. K., Titman, J. M., Mercer, M. (1995d), *J. Alloys and Compounds*, 231 434-435.

Kemali, M., Buckley, C. E., Ross, D. K., Bennington, S. M., Parker, S. F. (1997), *Physica B*, 234-236, 906-909.

Krishna, P. S. R. (1992), *Private Communication*.

Kubo, R. and Toyabe, T. (1967), *in R.Blinc (EDITOR), Magnetic Resonance and Relaxation*, North-Holland, Amsterdam, p. 810.

Kulda, J., Wildes, A., Martin-Martin, A., Mller, W., Heil, W., Humblot, H., Tasset, F. (1998), *Physica B,* 241-243 136-138.

Lide, D. R. EDITOR (1990-91), *Handbook of Chemistry and Physics*, CRC Press, 71st Edition.

Lovesey, S. W. (1984), *Theory of Neutron Scattering from Condensed Matter*, Clarendon Press, Oxford.

Lynch, J. F., Johnson, J. R., Reilly, J. J. (1979), *Z. Phys. Chem. N.F.*, 117, 229-243.

Maier-Leibnitz, H. and Springer, T. (1963), *Reactor Sci. and Technol.*, 17 217.

Magee, C. B., Lu, J., Lundin, C. E. (1981), *J. Less-Common Metals*, 78 119-138.

Magerl, A., Frick, B. and Liss, K. D. (1992), *SPIE*, 1738 360-367

Martín, D., Campbell, S. and Carlile, C. J. (1996), *J. Phys. Soc. Jpn* 65A 245.

Martín, D. (1996), *Private Communication.*

Martín, D. (1997), *Private Communication.*

Mezei, F. (1972), *Z. Phys.*, 255 146.

Mezei, F. (1976), Commun. Phys., 1 81.

Mezei, F. and Dagleish, P. A. (1977), Commun. Phys., 2 41.

Mildner, D. F. R. (1990a), *Nucl. Instr. & Meth. in Phys. Res. A*, 290 189-196.

Mildner, D. F. R. (1990b), *Nucl. Instr. & Meth. in Phys. Res. A*, 297 38-46.

Miron, N. F., Shcherbak, V. I., Bykov, V. N. and Levdik, V. A. (1971), *Sov. Phys. - Crystallography.*, 16 (2) 266-269.

Penfold, J. and Tomkinson, J. (1986), Rutherford Appleton Laboratory Report, RAL-86-019.

Press, W. H., Teukolsky, S. A., Vetterling, W. T. and Flannery, B. P. (1994), *Numerical Recipes in Fortran*, Cambridge University Press.

Randl, O. G. (1996), *ILL Report*, 96RA07T.

Renz, W., Majer, G. and Skripov, A. V. (1995), *J. Alloys and Compounds*, 224 127-129.

Ross, D. K. and Hall, P. L. (1979), *Advanced Chemical Methods for Soil and Clay Minerals Research*, D. Reidel Publishing Company, London.

Ross, D. K. (1992), *Physica B*, 182 318.

Ross, D. K. (1997a), *Topics in Applied Physics*, 73, Springer-Verlag, Berlin.

Ross, D. K. (1997b), *Osiris-The Next Steps*, EPSRC Proposal.

Rossbach, M., Schärpf, O., Kaiser, W., Graf, W., Schirmer, A., Faber, W., Duppich, J. and Zeisler, R. (1988), *Nucl. Instr. & Meth. in Phys. Res. B*, 35 181-190.

Rowe, J. M., Sköld, K, Flowtow, H. E. and Rush, J. J. (1971*), J. Phys. Chem. Solids*, 32 41.

Schärpf, O. (1989a), *Physica B*, 156&157 631-638.

Schärpf, O. (1989b), *Physica B*, 156&157 639-646.

Schärpf, O. and Capellmann, H. (1993), *Phys. Stat. Sol.* (a) 135 359.

Schärpf, O. and Anderson, I. S. (1994), *Physica B*, 198 203-212.

Schirmer, A., Heitjans, P., Faber, W. and Samuel F. J. (1990), *Meas. Sci. Technol.*, 1 654-656.

Schirmer, A. and Mildner, D. F. R. (1991), *Meas. Sci. Technol.*, 2 1059-1063.

Sears, V. F. (1989), *Neutron Optics*, Oxford University Press, Oxford.

Sivia, D. S., Carlile, C. J. (1992a), *J. Chem. Phys.*, 96 (1) 170.

Sivia, D. S., Carlile, C. J., Howells, W. S., Konig, S. (1992b), *Physica B*, 182 348.

Sivia, D. S., David, W. I. F., Knight, K. S., Gull, S. F. (1993), *Physica D*, 66 234.

Sivia, D. S. (1996), *Data Analysis: A Bayesian Tutorial*, Clarendon Press, Oxford.

Sköld, K. and Nelin, G. (1967), *J. Phys. Chem. Solids*, 28 2369.

Skripov, A. V., Rychkova, S. V., Belyaev, M. Yu., Stepanov, A. P. (1989), *Solid State Commun.*, 71 (12) 1119-1122.

Skripov, A. V., Belyaev, M. Yu., Stepanov, A. P., Dobrokhotova, Z. V., Padurets, L. N., Sokolova, E. I. and Shilov, A. L. (1993), *J. Alloys and Compounds*, 201 145-149.

Skripov, A. V., Cook, J. C., Karmonik, C. and Hempelmann, R. (1996), *J. Phys.: Condens. Matter*, 8 319-324.

Skripov, A. V., Cook, J. C., Karmonik, C. and Hempelmann, R. (1997), *J. Alloys*

and Compounds, 253-254, 432-434.

Skripov, A. V. and Hempelmann, R. (1997), *ILL Experimental Report* 7-02-33.

Skripov, A. V., Cook, J. C., Sibirtsev, D. S., Karmonik, C. and Hempelmann, R. (1998), *J. Phys.: Condens. Matter*, 10 1787-1801.

Soetratmo, M., Hempelmann, R., Hartmann, O., Wäppling, R. and Ekström, M. (1997), *J. Phys.: Condens. Matter*, 9 1671-1677.

Soyama, K., Suzuki, M., Kodaira, T., Ebisawa, T., Kawabata, Y. and Tasaki, S. (1995), *Physica B*, 213&214, 951-953.

Springer, T. (1972), *Quasielastic Neutron Scattering for the Investigation of Diffusive Motions in Solids and Liquids*, Springer-Verlag.

Squires, G. L. (1978), *Intro. to the theory of thermal neutron scattering*, Cambridge University Press, Cambridge.

Stonadge, P. R. (1992), *Ph.D. Thesis, University of Birmingham.*

Sutherland, J. C., Steichele, E., David, W. I. F., Johnson, M. W., Altrip, J. L., Ward, R. C. and Carlile, C. J. (1985), ICANS-VIII, *Rutherford Appleton Laboratory*, RAL-85-110, 771.

Taylor, A. D. (1984), *Rutherford Appleton Laboratory Report*, RAL-84-120.

Turchin, V. F. (1965), *Slow Neutrons*, Israel Program for Scientific Translations.

Turchin, V. F. (1967), Deposited Paper, At. Energy 22.

Van Hove, L. (1954), *Phys. Rev.*, 95 (1) 249.

Ward, R. C., Carlile, C. J., Goyal P. S. and Altrip J. L. (1985), ICANS-VIII, *Rutherford Appleton Laboratory*, RAL-85-110, 526.

Westlake, D. G. (1983), *J. of Less-Common Metals*, 90 251-273.

Williams, W. G. (1988), *Polarized Neutrons*, Clarendon Press, Oxford.

Willis, B. T. M. (1973), *Chemical Applications of Thermal Neutron Scattering*, Oxford University Press.

Willis, B. T. M., Carlile, C. J., Ward, R. C., David W. I. F. and Johnson, M. W. (1986), *Europhys. Lett.* 2 767.

Windsor, C. G. (1981), *Pulsed Neutron Scattering*, Taylor & Francis Ltd, London.

Zsigmond, G., (1997), *Private Communication*.